

**Recording, Processing and Use of Material-Specific Data  
in Pulse Electrochemical Machining**

**Dissertation**

zur Erlangung des Grades  
des Doktors der Ingenieurwissenschaften  
der Naturwissenschaftlich-Technischen Fakultät II  
- Physik und Mechatronik -  
der Universität des Saarlandes

von

Andreas Rebschläger

Saarbrücken

2015

Tag des Kolloquiums: 28.06.2016

Dekan: Prof. Dr.-Ing. Georg Frey

Berichterstatter: Prof. Dr.-Ing. Dirk Bähre  
Prof. Dr.-Ing. Stefan Seelecke

Vorsitz: Prof. Dr. Andreas Schütze

Akad. Mitarbeiter: Dr.-Ing. Frank Krämer



## **Abstract**

The present work focuses on the manufacturing process based on pulsed electrochemical dissolution. The quality of the Electrochemical Machining is dependent on the properties and composition of the processed material, the process parameters and the machine capability. Both, the reproduction accuracy and the possible feed rates, resulting from the dissolution rates of the materials and consequently also processing times differ, depending on the material and alloy components. The basic machine-dependent, yet material-independent processes are explained and presented in this work. Based on an experimental and simulation-based evaluation, a method for the acquisition of machine-independent material data under a number of influencing parameters is investigated. The focus of the investigation lies on a widely used stainless steel and a powder metallurgically produced high speed steel in different hardness conditions. The gathering of material-specific data will be presented for the use in a process simulation and will be validated against an in-process geometry measurement. For this purpose, an experimental set-up was designed, built and tested, which allows the observation of the dissolution process over a longer period of time under industrial process conditions. A theoretical approach focusing on the inverse tool simulation based on material data concludes the work.

## Kurzzusammenfassung

Die vorliegende Arbeit beschäftigt sich mit dem gepulsten, elektrochemisch abtragenden Fertigungsverfahren. Die Qualität der elektrochemischen Bearbeitung ist abhängig von den Eigenschaften und der Zusammensetzung des zu bearbeiteten Materials, den Prozessparametern und der Maschinenfähigkeit. Sowohl Abbildgenauigkeit als auch mögliche Vorschübe, welche aus den Auflöseraten der Materialien resultieren, und somit folglich auch Bearbeitungszeiten, unterscheiden sich je nach Material und Legierungsbestandteilen. Die grundlegenden, maschinenabhängigen jedoch materialunabhängigen Prozesse werden in dieser Arbeit erläutert und vorgestellt. Darauf aufbauend werden experimentelle und simulationsgestützte Auswerteverfahren zur Erfassung von maschinenunabhängigen Materialdaten unter einer Vielzahl von Einflussparametern untersucht. Der Fokus dieser Untersuchungen liegt hierbei auf einem weitverbreitet eingesetzten Edelstahl und einem pulvermetallurgisch hergestellten Schnellarbeitsstahl in unterschiedlichen Härtezuständen. Abschließend wird die Nutzung der erfassten werkstoffspezifischen Daten zur Prozesssimulation vorgestellt und anhand einer in-Prozess Geometrieerfassung validiert. Hierzu wurde eine Versuchsanordnung konzipiert, gebaut und getestet, welche die Beobachtung des Formgebungsprozesses über einen längeren Zeitraum unter industriellen Prozessbedingungen ermöglicht. Ein theoretischer Ansatz zur inversen Werkzeugsimulation auf Basis von Materialdaten bildet den Abschluss der Arbeit.

## Vorwort

Im Laufe der Entstehung der vorliegenden Arbeit stand ich in Kontakt mit einer Vielzahl von Personen, welche mich teils richtungsweisend beeinflusst und unterstützt haben. Diesen Personen möchte ich an dieser Stelle persönlich danken.

Meinem Doktorvater Prof. Dr.-Ing. Dirk Bähre danke ich für die besondere Betreuung und kritischen Fragen, sowie den stets offenen, sachlichen als auch sehr persönlich geprägten Austausch an Informationen und Meinungen im Rahmen vieler Diskussionen und Treffen.

Prof. Dr.-Ing. Stefan Seelecke danke ich für Übernahme des Korreferates und die vielen interessanten Diskussionen und Fragen zur interdisziplinären Anwendung der jeweils gegenseitigen Technologien.

Meinen langjährigen Kollegen Olivier Weber und Philipp Steuer, die mich während der Ausarbeitung ertragen mussten Danke ich besonders! Neben der gegenseitigen Unterstützung in der Etablierung des Themengebietes, waren es vor allem die unzähligen und meist spätabendlichen, fachlichen Diskussionen, welche viele wertvolle Inhalte im Rahmen der Ausgestaltung der Arbeit lieferten.

Bernd Heitkamp für die vielen Diskussionen und Denkanstöße.

Ein Dank an meine wissenschaftlichen Hilfskräfte, Bachelor- sowie Masterarbeiter, welche durch die Anfertigung von Abschlussarbeiten und Unterstützung zu dieser Arbeit beigetragen haben.

Herrn Privatdozent Dr. Lohrengel, Herrn Dr. Hoogsteen und Frau Dr. Baumgärtner für die fachlichen Diskussionen und Hinweise im Rahmen der INSECT Konferenzen.

Den Mitarbeitern der Firma PEMTec: Herrn Brussee, Herrn Grützmacher, Herrn Otto, Herrn Vollmer und Herrn Kuhn für die langjährige Unterstützung in den Bereichen der Maschinentechnik, Konstruktion, Analyse elektrischer Daten und diversen Eingriffen in die Maschinensteuerung sowie Anpassungen der Software.

Den wissenschaftlichen und technischen Mitarbeitern am Lehrstuhl für Fertigungstechnik danke ich für die vielen fachlichen und persönlichen Unterredungen.

Herrn Simon Staudacher für die Unterstützung im Bereich der Metallographie, Herrn Moritz Stolpe für die Unterstützung bei der Härtemessung, Frau Anne Bauer für die Anfertigung von Vorrichtungen.

Ein großer Dank an alle Mitarbeiter der ZeMA gGmbH und den Mitarbeitern der im ZeMA ansässigen Lehrstühle für deren Kooperation, zudem dem Land Saarland und dem Europäischen Fonds für regionale Entwicklung (EFRE) für die Förderung der Forschungsaktivitäten im Projekt INTEGRATIF - ProQ<sup>Quadrat</sup>.

Ganz speziell und von ganzem Herzen danke ich meiner Freundin für Ihre Geduld und allen voran **meinen Eltern**, welche mir den akademischen Weg überhaupt erst ermöglicht haben – DANKE!

# CURRICULUM VITAE

## Personal Information

Name Andreas Rebschläger  
Date of birth and place: May 10th, 1984 in St. Ingbert, Germany

## Professional Background

since 02/2015 Robert Bosch GmbH, Homburg/Saar, Germany  
01/2013 – 12/2014 Group leader manufacturing processes and automation at the ZeMA - Zentrum für Mechatronik und Automatisierungstechnik gemeinnützige GmbH, Saarbrücken, Germany  
04/2010 – 12/2012 Scientific employee at the ZeMA - Zentrum für Mechatronik und Automatisierungstechnik gemeinnützige GmbH, Saarbrücken, Germany

## Studies and Education

10/2004 – 03/2010 Dipl.-Ing. Mechatronik, Universität des Saarlandes, Germany  
2001 – 2003 Abitur, Leibniz-Gymnasium, St. Ingbert, Germany  
2000 – 2001 US High School Diploma, Minneapolis High School (USD 239), Minneapolis, Kansas, USA  
1994 – 2000 Leibniz-Gymnasium, St. Ingbert, Germany  
1990 – 1994 Grundschule Oberwürzbach, St. Ingbert, Germany

## Community Service

2003 – 2004 Community service (German: Zivildienst) German Red Cross, including the training as paramedic (German: Rettungssanitäter)

Parts of this work have been published as follows:

## **Publications**

O. Weber, H. Natter, A. Rebschläger, D. Bähre: Surface quality and process behaviour during Precise Electrochemical Machining of cast iron. International Symposium on Electrochemical Machining INSECT2011, Editors: B. Mollay, M.M. Lohrengel, pp.41-46, Vienna, 2011.

A. Rebschläger, O. Weber, D. Bähre: In-situ process measurements for industrial size Pulse Electrochemical Machining. International Symposium on Electrochemical Machining Technology INSECT2012, Editor: Maria Zybura-Skrabalak, pp.133-148, Krakow, 2012.

O. Weber, H. Natter, A. Rebschläger, D. Bähre: Analytical characterization of the dissolution behavior of cast iron by electrochemical methods. International Symposium on Electrochemical Machining Technology INSECT2012, Editor: Maria Zybura-Skrabalak, pp.41-55, Krakow, 2012.

D. Bähre, A. Rebschläger, O. Weber, P. Steuer: Reproducible, fast and adjustable surface roughening of stainless steel using Pulse Electrochemical Machining. Procedia CIRP 6, pp.385-390, 2013.

A. Rebschläger, O. Weber, B. Heitkamp: Benefits and Drawbacks Using Plastic Materials Produced by Additive Manufacturing Technologies in the Electrochemical Environment. International Symposium on Electrochemical Machining Technology INSECT2013, Editors: A. Schubert, M. Hackert-Oschätzchen, pp.45-51, Chemnitz, 2013.

A. Rebschläger, R. Kollmannsperger, D. Bähre: Video based process observations of the pulse electrochemical machining process at high current densities and small gaps. Procedia CIRP 13 (2013), pp. 418-423, 2013.

M. Swat, A. Rebschläger, D. Bähre: Investigation of the energy consumption for the pulse electrochemical machining (PECM) process. International Symposium on Electrochemical Machining Technology INSECT2013, Editors: A. Schubert, M. Hackert-Oschätzchen, pp.65-71, Chemnitz, 2013.

P. Steuer, A. Rebschläger, O. Weber, D. Bähre: The heat-affected zone in EDM and its influence on a following PECM process. Procedia CIRP 13, pp.276-281, 2013.

O. Weber, D. Bähre, A. Rebschläger: Study of Pulse Electrochemical Machining characteristics of spheroidal cast iron using sodium nitrate electrolyte. International Conference on Competitive Manufacturing, COMA 13, pp.125-130, South Africa, 2013.



O. Weber, A. Rebschläger, P. Steuer, D. Bähre: Modeling of the Material/Electrolyte Interface and the Electrical Current Generated during the Pulse Electrochemical Machining of Grey Cast Iron. Proceedings of the 2013 European COMSOL Conference in Rotterdam, Rotterdam, 2013.

D. Bähre, O. Weber, A. Rebschläger: Study of Pulse Electrochemical Machining of nickel-cobalt ferrous alloy. International Conference on Competitive Manufacturing, COMA 13, pp.119-124 , South Africa, 2013.

D. Bähre, O. Weber, A. Rebschläger: Investigation on Pulse Electrochemical Machining Characteristics of Lamellar Cast Iron using a Response Surface Methodology-based Approach. Procedia CIRP 6, pp.363-368, 2013.

D. Bähre and A. Rebschläger (Editors): Proceedings International Symposium on Electrochemical Machining Technology INSECT2014. ISBN 978-3-95735-010-7, 2014.

A. Rebschläger, K. U. Fink, T. Heib, D. Bähre: Geometric shaping analysis based on PECM video process observations. International Symposium on Electrochemical Machining Technology INSECT2014, Editors: D. Bähre, A. Rebschläger, pp.37-44, Saarbrücken, 2014.

P. Steuer, A. Rebschläger, A. Ernst, D. Bähre: Process Design in Pulse Electrochemical Machining Based on Material Specific Data – 1.4301 and Electrolytic Copper as an Example. Key Engineering Materials Vols 651-653, pp. 732-737, 2015.

M. Swat, A. Rebschläger, K. Trapp, T. Stock, G. Seliger, D. Bähre: Investigating the energy consumption of the PECM process for consideration in the selection of manufacturing process chains. Procedia CIRP. 22nd CIRP conference on Life Cycle Engineering (LCE), 2015.



**TABLE OF CONTENTS**

<b>ABBREVIATIONS &amp; SYMBOLS.....</b>	<b>II</b>
<b>LIST OF FIGURES.....</b>	<b>V</b>
<b>LIST OF TABLES .....</b>	<b>IX</b>
<b>1 INTRODUCTION.....</b>	<b>1</b>
<b>2 THE ELECTROCHEMICAL MACHINING PROCESS .....</b>	<b>3</b>
2.1 ELECTROCHEMICAL DISSOLUTION .....	3
2.2 ELECTROCHEMICAL MACHINING – ECM .....	6
2.3 ELECTROLYTE .....	14
2.4 PULSE ELECTROCHEMICAL MACHINING – PECM .....	18
<b>3 SCIENTIFIC CONCEPT AND APPROACH.....</b>	<b>23</b>
<b>4 INVESTIGATED MATERIALS .....</b>	<b>25</b>
4.1 STAINLESS STEEL 1.4301 .....	25
4.2 POWDER METALLURGICAL STEEL S390 .....	27
4.3 BASIC ELECTROCHEMICAL ANALYSIS .....	29
<b>5 INVESTIGATION METHODS.....</b>	<b>33</b>
5.1 FRONTAL GAP EXPERIMENTS .....	34
5.2 SIDE GAP EXPERIMENTS .....	48
5.3 CONTINUOUS OBSERVATIONS .....	49
5.4 ELECTRICAL AND SURFACE MEASUREMENTS.....	56
<b>6 SIMULATION CONCEPT.....</b>	<b>59</b>
6.1 STATIC SIMULATION .....	59
6.2 SIMULATION BASED ON MATERIAL-SPECIFIC DATA.....	62
6.3 TOOL SIMULATION BASED ON MATERIAL-SPECIFIC SIMULATION .....	67
<b>7 EXPERIMENTAL RESULTS, SIMULATION AND DISCUSSION.....</b>	<b>69</b>
7.1 MATERIAL-SPECIFIC DATA.....	69
7.1.1 Stainless steel 1.4301 .....	69
7.1.2 Powder metallurgical steel S390 .....	77
7.2 EFFECTS FROM CONTINUOUS OBSERVATIONS .....	86
7.3 SIMULATION BASED ON MATERIAL-SPECIFIC DATA.....	91
<b>8 SUMMARY AND CONCLUSION .....</b>	<b>97</b>
<b>REFERENCES.....</b>	<b>99</b>
<b>APPENDIX A OLYPMUS ISPEED-TR .....</b>	<b>114</b>
<b>APPENDIX B MICROSCOPE CALIBRATION SLIDE.....</b>	<b>115</b>

## ABBREVIATIONS & SYMBOLS

Abbreviation or symbol	Unit	Meaning
A	cm <sup>2</sup>	surface area
a	$\frac{mg \cdot cm^2}{C \cdot A}$	constant
a <sub>i</sub>		reference point on anode
AFM		Abrasive Flow Machining
AISI		American Iron and Steel Institute
b	$\frac{1}{s}$	constant
C		constant
C	$\frac{g}{l}$	electrolyte concentration
c		constant
c <sub>i</sub>		reference point in cathode
CAD		computer-aided design
CV		Cyclic Voltammetry
d	$\frac{1}{s}$	constant
DIN		Deutsches Institut für Normung
e		constant
e <sup>-</sup>		electron (negative charge)
ECM		Electrochemical Machining
EDM		Electrical Discharge Machining
EN		European Committee for Standardization
F	$\frac{C}{mol}$	Faraday constant (96,485.33289 C/mol)
f	$\frac{mg}{C}$	constant
f	Hz	frequency
f <sub>electric</sub>	Hz	electrical frequency
FEM		Finite element method
f <sub>mechanic</sub>	Hz	mechanical frequency
h	mm	removal height
HB		hardness scale Brinell
HRC		hardness scale Rockwell (C=150kgf, 120°diamond cone)
HV30		hardness scale Vickers (30 = load of 30kgf)
I	A	electrical current
ICP-OES		Inductive Coupled Plasma - Optical Emission Spectrometry
I <sub>exp</sub>	A	experimental amperage
I <sub>FEM</sub>	A	FEM simulated process current
I <sub>frontal</sub>	A	current through frontal gap
I <sub>local,i</sub>	A	local current between reference points a <sub>i</sub> and c <sub>i</sub>
I <sub>max</sub>	A	maximum amperage
I <sub>real</sub>	A	real measured process current

$I_{\text{side}}$	A	current through side gap
ISO		International Organization for Standardization
$I_{\text{total}}$	A	total current
J	$\frac{A}{\text{cm}^2}$	current density
LED		Light-Emitting Diode
LFT		Lehrstuhl für Fertigungstechnik (Institute of Production Engineering at Saarland University)
lhs		Left-hand side
m	g	mass
M	$\frac{g}{\text{mol}}$	molar mass
MRR	$\frac{\text{cm}^3}{\text{C}}$	mass removal rate
$m_{\text{pract}}$	G	practical mass removal
$m_{\text{theor}}$	g	theoretical mass removal
NaCl		sodium chloride
NaNO <sub>3</sub>		sodium nitrate
p	kPa	pressure
P	μm	position
PA		Polyamide
PECM		Pulse Electrochemical Machining
pH		pH value
PMMA		Polymethylmethacrylat
$P_{\text{shift}}$	%	phase shift (in percent) in relation to a reference
Q	C	electrical charge
R	Ω	ohmic resistance
R <sup>2</sup>		coefficient of determination of a linear regression
$R_a$	μm	Arithmetischer Mittenrauwert
$R_{\text{exp}}$	A	experimental ohmic resistance
rhs		Right-hand side
$R_{\text{max}}$	μm	Maximale Rautiefe
$R_z$	μm	Gemittelte Rautiefe
s	μm	(frontal) gap distance
s	mm	removal height
SEM		Scanning Electron Microscope
SMR	$\frac{mg}{\text{C}}$	Specific Mass Removal
t	s	time
T	°C	temperature
T	s	oscillation period
$t_{\text{on}}$	ms	pulse on time
$t_{\text{shift}}$	ms	phase shift in seconds
$t_{\text{shutter}}$	μs	shutter time (digital camera)
U	V	voltage
$U_{\text{exp}}$	V	experimental voltage
$U_{\text{pol}}$	V	polarization voltage
$U_{\text{polA}}$	V	anodic polarization voltage
$U_{\text{polC}}$	V	cathodic polarization voltage
$U_{\text{prod}}$	V	productive voltage

US		United States
$U_{\text{sim}}$	V	simulated voltage
USSR		Union of Soviet Socialist Republics
V	$\text{cm}^3$	Volume
v	$\frac{\text{mm}}{\text{min}}$	velocity
v	$\frac{\text{mm}}{\text{min}}$	feed rate
VDE		Verband der Elektrotechnik und Elektronik
VDI		Verein Deutscher Ingenieure
$y_0$	$\mu\text{m}$	initial gap
z		valence
ZeMA		Zentrum für Mechatronik und Automatisierungstechnik gemeinnützige GmbH
$\eta$	%	current efficiency
$\kappa$	$\Omega\text{cm}$	specific resistance
$\rho$	$\frac{\text{g}}{\text{cm}^3}$	density
$\sigma$	$\frac{\text{mS}}{\text{cm}}$	conductivity

## LIST OF FIGURES

Figure 2-1 Ion migration schematic in cathode anode setup according to [1].....	3
Figure 2-2 Schematic of electrochemical dissolution processes in ECM, similar [3] .....	9
Figure 2-3 Schematic of ECM shaping.....	9
Figure 2-4 Designation of process specific terms .....	10
Figure 2-5 Polarization voltages at anode and cathode .....	13
Figure 2-6 Example of a calculation with and without considering the polarization voltage .....	14
Figure 2-7 Schematic of the current efficiency using different electrolytes .....	15
Figure 2-8 Effects on the current efficiency under the assumption of different valences .....	16
Figure 2-9 Difference in side gap evolution using a NaCl or NaNO <sub>3</sub> based electrolyte (Assumption: equal conductivity) .....	17
Figure 2-10 Schematic of the PECM process .....	19
Figure 2-11 Time-dependent variables .....	20
Figure 2-12 Technical constraints of the equipment used in the experiments .....	21
Figure 2-13 Shift in Phase of the current pulse in relation to the mechanical oscillations bottom dead center.....	22
Figure 3-1 Information flow chart.....	23
Figure 4-1 Optical micrograph images 1.4301 using a lhs: confocal laser scanning microscope rhs: digital microscope.....	26
Figure 4-2 S390 in the soft-annealed state – average: 296.1 HV30 / 29.2 HRC .....	28
Figure 4-3 S390 in the hardened state – average: 786.9 HV30 / 63.1 HRC.....	28
Figure 4-4 Cyclic voltammetry at a scanning rate of 20 mV/s.....	30
Figure 4-5 Chronoamperometrie at 3 V vs. Hg/Hg <sub>2</sub> SO <sub>4</sub> for 3 min.....	31
Figure 5-1 Schematic of a conventional frontal and side gap experiment .....	34
Figure 5-2 Experimental setup schematic.....	35
Figure 5-3 Experimental setup .....	35
Figure 5-4 Machining 5.65 mm <sup>3</sup> (43.92 mg) of material for three consecutive times.....	37
Figure 5-5 Effect of different starting gaps at three different pulse on times (a) $t_{on} = 1$ ms, b) $t_{on} = 2.5$ ms, c) $t_{on} = 4$ ms) and equal current density at $U=10V$ <i>Exp. 1: first PECM after sample preparation Exp. 2: Starting gap = equilibrium gap Exp. 3: Starting gap &lt; equilibrium gap Exp. 4: Starting gap &gt; equilibrium gap</i> .....	39

Figure 5-6 Development of equilibrium conditions at different starting gaps and two different voltages U = 12.5V (lhs) and U = 15V (rhs).....	40
Figure 5-7 Stability of the current density (top) at repeated experiments under different experimental conditions (bottom) .....	41
Figure 5-8 Influence of the shift of phase on the frontal gap at equal current density and U=10V (lhs) and U=15V (rhs) .....	42
Figure 5-9 Percentage deviation of the frontal gap distance at different shifts of phase and equilibrium gap of 20 $\mu\text{m}$ .....	43
Figure 5-10 Deviations due to different feed rates or a shift in phase assuming a 10 $\mu\text{m}$ gap at the oscillations bottom dead center at 10 Hz (lhs) and 50 Hz (rhs) .....	44
Figure 5-11 Deviations due to different feed rates or a shift in phase assuming a 290 $\mu\text{m}$ gap at the oscillations bottom dead center at 10 Hz (lhs) and 50 Hz (rhs) .....	44
Figure 5-12 Influence of the frequency change on the frontal gap and current density at U=10V (lhs) and 15V (rhs).....	45
Figure 5-13 Effect on the frontal gap at different pressure and phase = 50 % and equal current density at U = 10V (lhs) and U = 15V (rhs).....	46
Figure 5-14 Calculation of the SMR value at different parameter settings .....	47
Figure 5-15 Course of processing in side gap experiments.....	48
Figure 5-16 Theoretical and practical side gap evolution.....	49
Figure 5-17 Experimental setup for continuous observations .....	50
Figure 5-18 Setup flushing chamber .....	51
Figure 5-19 Voltage (U), Pressure (P), Resistance (R) and Position (P) relationship in PECM over time, similar [58, 71] .....	52
Figure 5-20 Setup integrated in PEMCenter8000 (Setup: Inlet 1 - Outlet 3) .....	52
Figure 5-21 Reference structure on each cathode.....	53
Figure 5-22 Schematic of the minimum and maximum image blur resulting from the mechanical oscillation at f=50Hz and a shutter time of 150 $\mu\text{s}$ .....	54
Figure 5-23 Results of a nonstop 120 min PECM experiment divided into 900 s intervals .....	55
Figure 5-24 Data correction based on external measurement.....	57
Figure 5-25 Rise and fall times at different pulse on times .....	57
Figure 6-1 Schematic result of a FEM simulation picturing the electric potential (colors) and the lines indicating the homogeneity of the current density in the experimental setup .....	59
Figure 6-2 Diameter correction 1.4301 setup (Diameter: Anode 6 mm vs. Cathode 8 mm).....	61
Figure 6-3 Diameter correction S390 setup (Diameter: Anode 6.3 mm vs. Cathode 6.3 mm) .....	61
Figure 6-4 Simulation of a process snapshot [87].....	62



---

Figure 6-5 Classification of materials, similar [41].....	63
Figure 6-6 Current efficiency in ECM and PECM, schematic similar [112].....	65
Figure 6-7 Scheme of the calculation steps implemented in Matlab.....	66
Figure 6-8 Sequence of a simulation with examples Inside loop: Simulation of the anode geometry using a given cathode Outside loop: Iterative inverse simulation of the anode and cathode geometry using a targeted anode geometry.....	68
Figure 7-1 Current density [ $A/cm^2$ ] vs. feed rate [mm/min] .....	69
Figure 7-2 Current density [ $A/cm^2$ ] vs. SMR [mg/C].....	70
Figure 7-3 Current density [ $A/cm^2$ ] vs. frontal gap [ $\mu m$ ] for all pulse times [ms] and voltages [V] .....	70
Figure 7-4 Current density [ $A/cm^2$ ] vs. polarization voltage [V] .....	71
Figure 7-5 lhs: Current density [ $A/cm^2$ ] vs. feed rate [mm/min] rhs: Current density [ $A/cm^2$ ] vs. SMR [mg/C] .....	72
Figure 7-6 Time [min] vs. side gap [ $\mu m$ ] development at an initial gap of 20 $\mu m$ .....	73
Figure 7-7 Gap widening: Experiment, Theory and Simulation.....	74
Figure 7-8 Optical images of the machined surface.....	74
Figure 7-9 Surface roughness of 1.4301 at different current densities [ $A/cm^2$ ].....	75
Figure 7-10 SEM surface images of 1.4301 at different current densities .....	76
Figure 7-11 Current density [ $A/cm^2$ ] vs. feed rate [mm/min] lhs: S390 soft-annealed / rhs: S390 hardened.....	77
Figure 7-12 Current density [ $A/cm^2$ ] vs. polarization voltage [V] lhs: S390 soft-annealed / rhs: S390 hardened.....	78
Figure 7-13 Current density [ $A/cm^2$ ] vs. frontal gap [ $\mu m$ ] - including theoretical calculation following Ohm's law - lhs: S390 soft-annealed / rhs: S390 hardened.....	78
Figure 7-14 Current density [ $A/cm^2$ ] vs. SMR [mg/C] lhs: S390 soft-annealed / rhs: S390 hardened ..	79
Figure 7-15 Time [min] vs. side gap [ $\mu m$ ] development at an initial gap of 20 $\mu m$ lhs: S390 soft-annealed / rhs: S390 hardened .....	80
Figure 7-16 Optical image of a S390 surface ( $\phi 6.3$ mm) after machining at a current density below 20 $A/cm^2$ .....	80
Figure 7-17 Optical micrograph images S390 in soft-annealed and hardened state.....	81
Figure 7-18 S390 SEM surface images at different current densities.....	82
Figure 7-19 Current density [ $A/cm^2$ ] vs. surface roughness S390 soft-annealed .....	84
Figure 7-20 Current density [ $A/cm^2$ ] vs. surface roughness S390 hardened .....	85
Figure 7-21 Electrode geometries for continuous dissolution and shaping observation.....	86
Figure 7-22 Verification of the feed rate used in the experiment and illustration of the oscillation and equilibrium frontal gap based on the acquired data .....	87

---

Figure 7-23 Direct extraction of material data from video data [88] .....	88
Figure 7-24 Side gap detection using software analysis .....	89
Figure 7-25 Side gap evolution 0.4 mm below the initial anodic surface as function over time based on video observation [88] .....	90
Figure 7-26 Experimental data for the validation of the introduced simulation .....	91
Figure 7-27 Material data for 1.4301 ( $U=10V$ and $t_{on}=2.5ms$ ).....	92
Figure 7-28 Calculated shape compared to the experimental contour .....	93
Figure 7-29 Inverse calculation of the cathode geometry .....	94

---

## LIST OF TABLES

Table 2.1 List of known properties and electrochemical valence values [3, 4] .....	4
Table 2.2 Theoretical mass removal per Coulomb of iron .....	5
Table 2.3 Short history of ECM [12, 13, 14, 15] .....	7
Table 4.1 Chemical composition of the austenitic steel 1.4301 .....	25
Table 4.2 Chemical composition of the powder metallurgical steel S390 [78].....	27
Table 5.1 Anode and cathode combinations in the experiments .....	35
Table 5.2 Optical resolution based on image acquisition using a microscope calibration slide.....	53
Table 5.3 External, electric measuring equipment .....	56
Table 6.1 Electrical data on the materials taken from their individual data sheets .....	60
Table 6.2 Classification of materials, similar [41] .....	64
Table 7.1 S390 S - optical images of the machined surfaces and experimental data .....	83
Table 7.2 S390 S - experimental data .....	83
Table 7.3 S390 H - experimental data.....	84
Table 7.4 tanh-fit data under defined boundary conditions .....	92
Table 7.5 Calculation data.....	94



# 1 Introduction

Electrochemical Machining as an unconventional production process, though already commercially available around 1959 for the use in production, nowadays experiences advanced applications through the modification of the mechanical as well as the electrical components. While the principle of material dissolution based on electrochemical processes remains unaltered, cost-driven mass production in combination with high precision and reproducibility as well as micro-structuring are pushing the development of the technology towards modified processing and machine technologies.

One of these developments in processing and machine technology in recent years is Pulse Electrochemical Machining. Electrical pulses in the millisecond range and pulse overlaid mechanical tool vibration are the key deviations from the basic Electrochemical Machining.

Based on personal experiences gathered from 2010 to 2015, mostly in discussions and personal talks during the yearly International Symposium on ElectroChemical Machining Technology (INSECT) and other topic specific conferences, the application and decision for the invest into this process stands and falls with the understanding of the basic principles thus the understanding of the possible use cases the technology provides. Entrusted with the task to establish and supervise the introduction of the then new technology at the Zentrum für Mechatronik und Automatisierungstechnik gemeinnützige GmbH (ZeMA) and to transfer the results towards application in cooperation with the Lehrstuhl für Fertigungstechnik (LFT) at the Saarland University, this work is also meant to provide a cornerstone for future generations at both institutes.

The aim of this work is therefore to present the basics and principles of electrochemical dissolution, which enable their use in production, and from thereon to investigate in depth the possibility to describe the information for the process and the information in the process, based on these principles.

Instead of devoting a single chapter to the state of the art and available knowledge from scientific literature, the topic specific information are incorporated into the individual chapters.

By using and creating a standardized and mutually comparable representation of the main process parameters and influences, the transferability towards use cases will be enabled. Furthermore, the use and application of this material and machine-specific knowledge will be transferred towards and validated against the application using industrial equipment. With the concept of using the gathered information and to simulate the process using software and thereby visualizing effects and relationships, a method to improve the understanding and knowledge about this unconventional process will be provided.



## 2 The electrochemical machining process

### 2.1 Electrochemical dissolution

The electrochemical (EC) process is the basic underlying process for the use of electrochemical technology in production. The electrochemical dissolution describes the dissolution process based on an electrical current over time taking place at the interface between two connecting surfaces of different media. In this work, this interface is between an electrolyte and a metal.

While the electrochemical reaction and its effects as well as consequences are well known as corrosion, the electrochemical dissolution can be intentionally induced by external influence. Figure 2-1 provides a schematic view of the ion migration taking place between two electrodes. The term electrode is used independent of the polarity, the term anode is synonymous for an electrode with positive polarity and the term cathode for an electrode with negative polarity. When exposed to an electric field and the resulting current caused by applying a voltage, the ions migrate in an electrolyte solution according to their charge towards the mutual electrode. The electrolyte, an electrically conductive fluid, is hereby mostly composed of demineralized water and the addition of a salt causing the conductive properties of the composition.

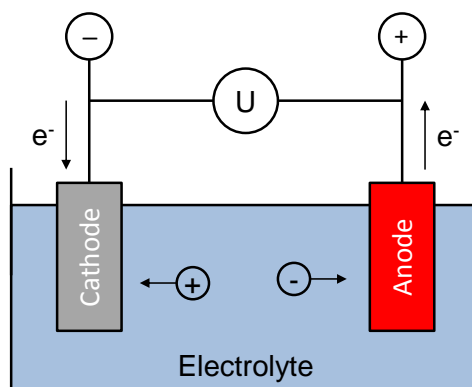


Figure 2-1 Ion migration schematic in cathode anode setup according to [1]

The effects taking place when inducing a current into an electrochemical system is better known and described as Faraday's laws of electrolysis published in 1834 [2]:

- Faraday's first Law of Electrolysis  
*The mass of a substance altered at an electrode during electrolysis is directly proportional to the quantity of electricity transferred at that electrode. Quantity of electricity hereby refers to the quantity of electrical charge measured in coulomb.*
- Faraday's second Law of Electrolysis  
*For a given quantity of D.C electricity (electric charge), the mass of an elemental material altered at an electrode is directly proportional to the element's equivalent weight.*

Equation 2-1 describes Faraday's law in terms of the electrical charge needed to remove a certain mass of material characterized by its molar mass and oxidation state (valence) [1].

$$Q = I \cdot t = \frac{m \cdot F \cdot z}{M} \quad \text{Equation 2-1}$$

With Q electrical charge in Coulomb [C], I electrical current (direct current DC) in Ampere [A], t is the uninterrupted time the electrical current flows through the material in seconds [s], m mass of material dissolved at the anode in [g], F Faraday constant [F = 96,485.33289 C/mol], M Molar mass of the substance in [g/mol] and z as the valence, which corresponds with the number of electrons transferred during the oxidation. While the overall valence of a material is based on the individual composition and electrochemical constraints of its dissolution, the valences of elements is available in literature. Table 2.1 shows a listing of elements and their main valences, as well as other properties, relevant in this work.

Table 2.1 List of known properties and electrochemical valence values [3, 4]

Element		Molar mass [g/mol]	Electrochemical valence z [ ]	Density [g/cm <sup>3</sup> ]
Aluminum	Al	26.98	3	2.7
Chromium	Cr	52.00	2, 3, 6	7.19
Iron	Fe	55.85	2, 3	7.86
Cobalt	Co	58.93	2, 3	8.83
Copper	Cu	63.55	1, 2	8.93
Manganese	Mn	54.92	2, 4, 6, 7	7.21
Molybdenum	Mo	95.94	3, 4, 6	10.2
Nickel	Ni	58.70	2, 3	8.90
Titanium	Ti	47.90	3, 4	4.5
Vanadium	V	50.94	3, 5	5.8
Tungsten	W	182.85	4, 5, 6	19.3

Looking towards the technological approach of deliberate and targeted processing of material, the meaningfulness of Faraday's law lies in the electrochemical removal of a material described through either mass or volume. Transformed to the mass or volume of a single element material removed by the transferred charge, Equation 2-1 can be rewritten as:



$$m = \frac{M}{z \cdot F} \cdot I \cdot t \quad \text{Equation 2-2}$$

$$m = V \cdot \rho = \frac{M}{z \cdot F} \cdot I \cdot t \quad \text{Equation 2-3}$$

$$V = \frac{M}{z \cdot F} \cdot \frac{1}{\rho} \cdot I \cdot t \quad \text{Equation 2-4}$$

V equals the volume of the material dissolved at the anode in [cm<sup>3</sup>] and ρ the density of the material in [g/cm<sup>3</sup>].

The following example based on Faraday's law shows the drastic difference in the case of 100 % theoretical mass removal per Coulomb of pure iron assuming different valence using an equivalent of Equation 2-2 and the valences of iron described in Table 2.1.

Table 2.2 Theoretical mass removal per Coulomb of iron

$Fe \rightarrow Fe^{3+} + 3e^{-}$	$\frac{m}{Q} = \frac{M}{F \cdot z} = \frac{55.85 \frac{\text{g}}{\text{mol}}}{96,485.33289 \frac{\text{C}}{\text{mol}} \cdot 3} = 0.193 \frac{\text{mg}}{\text{C}}$
$Fe \rightarrow Fe^{2+} + 2e^{-}$	$\frac{m}{Q} = \frac{M}{F \cdot z} = \frac{55.85 \frac{\text{g}}{\text{mol}}}{96,485.33289 \frac{\text{C}}{\text{mol}} \cdot 2} = 0.289 \frac{\text{mg}}{\text{C}}$

This rather simple contemplation in Table 2.2 shows how strongly the valence influences the material removal per Coulomb in the theoretical approach. In practice the valence depends on the current per area, the so-called current density, and usually occurs as a composition of different valence states. The experimental validation of the actual valence and its percentage distribution with regard to the current density for different elements can be found in e.g. [5] or [6]. The significance and effects resulting from the valence in an electrochemical system towards the aim of this work will be considered again in a following paragraph.

For an alloy composed of several elements the mass dissolved can be calculated as the superposition of the individual elements [7] indicated by index i and the number of electrochemically dissolvable elements n

$$m = \sum_i^n \frac{M}{z_i \cdot F} \cdot I \cdot t \quad \text{Equation 2-5}$$

$$V = \frac{1}{\rho_{alloy}} \cdot \sum_i^n \frac{\rho_i}{100} \cdot \frac{M}{z_i \cdot F} \cdot I \cdot t \quad \text{Equation 2-6}$$

As already presented in the rather simple example calculation, in the case of iron assuming only two different valence values, this approach gets many times more complex looking at an alloy. Yet, using Equation 2-6 the theoretical material removal can be calculated for alloys with diverse and complex composition.

## 2.2 Electrochemical Machining – ECM

The technical use in production based on Faraday's law is the Electrochemical Machining, short ECM. These days ECM is mainly used in mass production e.g. by companies like Philips [8] for the production of shaver caps, companies manufacturing turbomachinery components [9], like LEISTRITZ TURBINENTECHNIK GmbH or MTU Aero Engines AG, or in general the deburring of components. While the underlying basics of the EC processes and mechanisms are the focus of research in the field of physical chemistry, this broad knowledge is eventually finding the way into the production, since many overlapping and interfering effects occur during the practical use in production engineering.

Since its first practical application in 1928, see Table 2.3, Electrochemical Machining became more and more interesting in industry. Arguments for the use of ECM are stress free machining [3], the capability to process independent of the hardness state of a metal, the theoretically infinite endurance of tools and the possibility of high parallelization. To enable a user of this technology, high standards and requirements have to be met concerning the power sources, machine robustness against the corrosive environment, automation and coatings. These enablers are also main obstacles to the technology. The process differs considerably from conventional machining technologies like milling, turning and grinding, which makes it complicated to become familiar with the theory quickly. Also monitoring and interpreting the process during machining is complicated, since hardly any in-process investigations or measurements at the electrode interfaces under process conditions are possible due to high current densities. Furthermore, compared to other technologies the initial acquisition costs are high. In this context Corbin [10] states:

*"[...] Electrochemical machining is a last resort, not a step up. It is used when there is no other practical way to machine a part, because it is very costly, slow and difficult to make the hole precisely the right diameter and shape without going to much higher expense than with traditional machining techniques. ECM has its uses, one of which is to machine carbide materials that simply cannot be cut any other way. There is nothing inherently more accurate about ECM. It costs fortunes in equipment just to make it the same accuracy as lathe boring, reaming, and diamond lapping. Using ECM makes sense when you can't cut the material in a more traditional way. People who sell ECM machines are the first to tell you this. [...]"*

Despite the costs and complexity, ECM still is an important machining technology in mass production and is gradually finding its way into smaller series. Selection criteria indicating the use of ECM were already discussed in 1972 [11]. Due to advances in power sources and processing, the focus in current research - personally judging from the publications in recent years - has shifted towards the processes taking place during material dissolution and more precise material models in general. This knowledge then enables the reduction of iterations needed in tool-shaping, thus making the process more competitive and cost efficient.

Table 2.3 Short history of ECM [12, 13, 14, 15]

around 1834	Michael Faraday (1791-1867) discovered the relationship between electric charge and material conversion during electrolysis.
1928	V.N. Gusev and L. Rozkov [13] (in Western literature often found as W. Gussef) used the anodic dissolution with the aim to properly dissolve metal - Electrochemical Machining (ECM).
1959	First commercial machine available in the US - Anocut Engineering Company.
1960-1970s	Serial use of ECM in the aerospace branch (industry) and in tool manufacturing (forging dies) began in the USSR and in Western Europe. Electrochemical technologies developed during this period and companies like Philips, Hitachi, Mitsubishi, AEG Elotherm, Amchem provided the equipment.
around 2000	Expansion of ECM technology with electrical and mechanical pulses.
1998 - 2011	The complex of new bipolar microsecond ECM by vibrating tool-electrode was introduced to market - Pulse Electrochemical Machining (PECM).
starting 2000	Possibility to use the technology in the field of micro-structuring, including the use of pulse length in the sub microsecond range.

In DIN8580 [16] ECM is defined in the main group focusing on separating processes. As part of the subgroup 3.4, ECM is further defined in DIN8590 [17] as imaging electrochemical removal using an external power source at high current density, caused by small distance between the tool electrode and the work piece at high flow velocities of the electrolyte solution. Furthermore VDI3400 [18] and subsequent the draft of VDI3401-Blatt 1 [19], based on VDI3401-Blatt 1 [20] and VDI3401-Blatt 3 [21], include definitions, a glossary and pictured use cases based on the

electrochemical dissolution. Most of these use cases can already be found in one of the earliest books about ECM, the book of De Barr and Oliver [22] dating from 1968. Here processes like electrolytic honing, electrochemical turning and milling as well as electrochemical shaping, among others, are presented. In fact, the book ends with chapter 13 "*The future of electrochemical machining*", stating disadvantages of the technology, which are partially still present today: Unfamiliarity with the techniques involved, high capital costs, controlling the process and tool design for ECM.

In the following roughly fifteen years a lot of renowned, scientific literature appeared:

- 1969 the PhD thesis of Pahl [23] focused on the imaging accuracy,
- 1971 Wilson [24] published his exceptional book "*Practice and Theory of Electrochemical Machining*"
- 1972 the PhD thesis of Degenhardt [11] with focus on the machinability of metallic materials
- 1973 an article about ECM by Maus (company Bosch GmbH) [25]
- 1973 a theoretical model for high rate ECM was published citing current densities up to 5,800 A/cm<sup>2</sup> [26]
- 1973 an article about reproduction accuracy with ECM: Determination of the side gap in Deitz et al. [27]
- 1974 McGeough [28] publishes the book "*Principles of Electrochemical Machining*"
- 1977 Bannard [29] published a review of literature regarding kinetics of the dissolution process, metallographic effects and optimization
- 1980 the Machining Data Handbook [3] lists a wide range of available machining data on the process, materials and covering use cases, schematics, valences and much more
- 1979 and 1984 Degner publishes books about finishing technologies [30] and ECM [31]

Later works of e.g. Weller [32] in 1984 starts focusing on a wider range of nontraditional machining processes like AFM, EDM and ECM. Also following publications focus on specific topics and problems in the field of ECM rather than talking about the wide range of applications and the basic theory – the works get more focused on specifics. Designated works describe the mathematics of anodic smoothing [33], anodic shaping [34] as well as deburring and cavity-forming [35]. Special topics in the manufacturing applications and productivity limitations of ECM [36] are discussed and works of Rajurkar et al. [37], Klocke and König [7] as well as Spur [38] reiterate the knowledge in today's standard literature used for teaching purposes. The strong electrochemical evolution as well as trends in ECM, Pulse ECM and  $\mu$ ECM is presented in [39] and [40].

A schematic of the electrochemical dissolution is presented in Figure 2-2. When applying an electric voltage the current through the system represented by cathode, electrolyte and anode causes basic reactions. The key process is the dissolution of metal at the anode. This anodic dissolution of - in this case - iron into bivalent iron

( $\text{Fe}^{2+}$ ; valence  $z = 2$ ) and the further reaction towards iron hydroxide ( $\text{Fe}(\text{OH})_2$ ), which then gets flushed out of the interelectrode gap by a constantly applied stream of electrolyte.

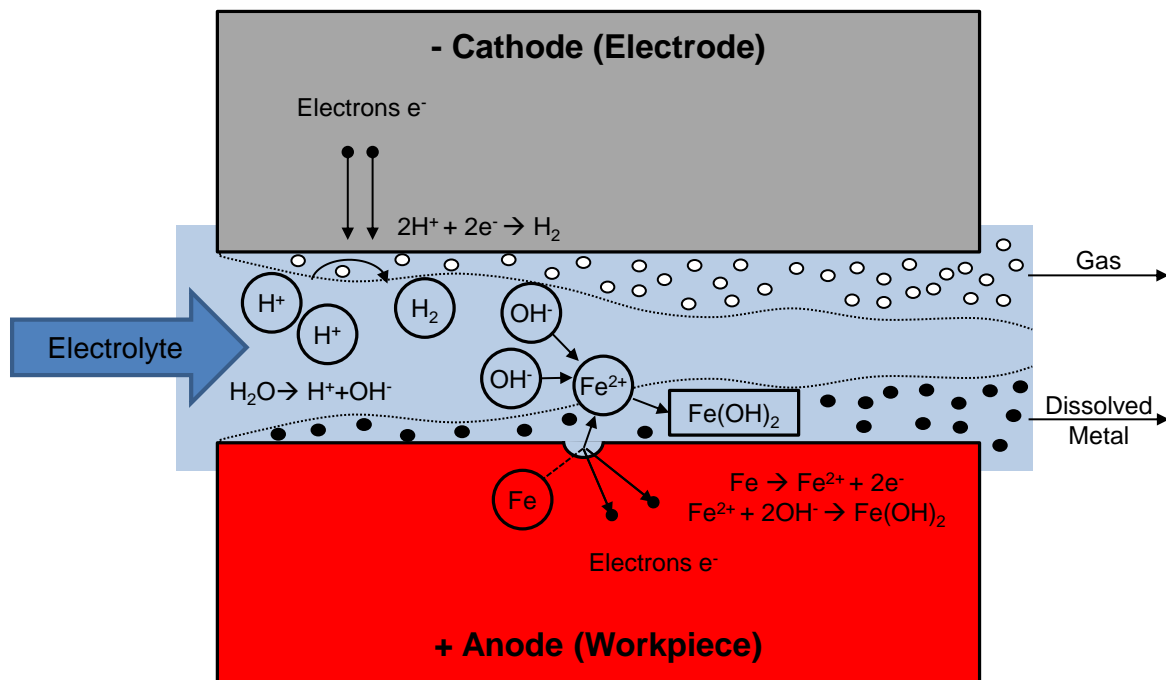


Figure 2-2 Schematic of electrochemical dissolution processes in ECM, similar [3]

While this schematic only shows the outermost basics of anodic dissolution, it is sufficient to understand the working principle in production. The shaping process is presented in Figure 2-3. Since the removal of metal only takes place on the anode interface, a feed of a tool towards this electrode allows an almost imaging processing. However, a one-to-one imaging machining of the tool electrode (cathode) into the work piece (anode) can never happen since a gap of electrolyte needs to be present to enable the electrochemical dissolution process. Many factors influence the work result [41] the following paragraph will focus on the most basic relationships in ECM.

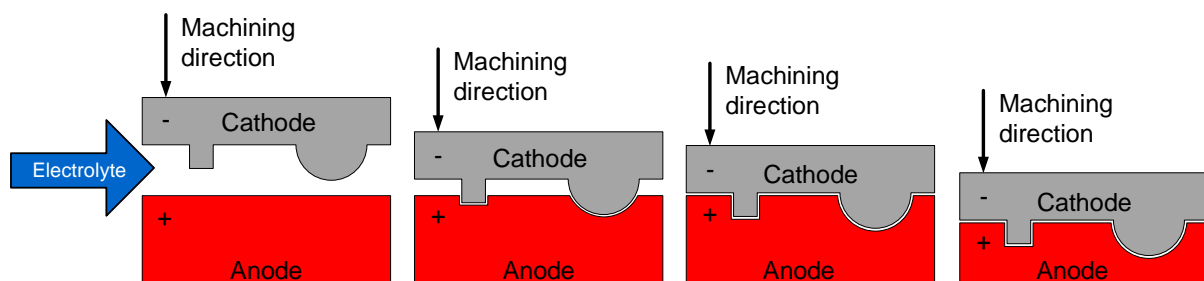


Figure 2-3 Schematic of ECM shaping

For further understanding, a few terms specific to ECM have to be introduced. While most of today's sinking ECM machines only allow a tool movement in one direction, a frontal gap and a side gap have to be distinguished. Figure 2-4 displays the frontal

gap, which describes the area in the projection direction of the movement of the cathode and the side gap. The phenomena of a widening side gap, which is untypical to most known conventional technologies, when the tool is not fed into the corresponding direction, will be discussed in detail in chapter 2.3.

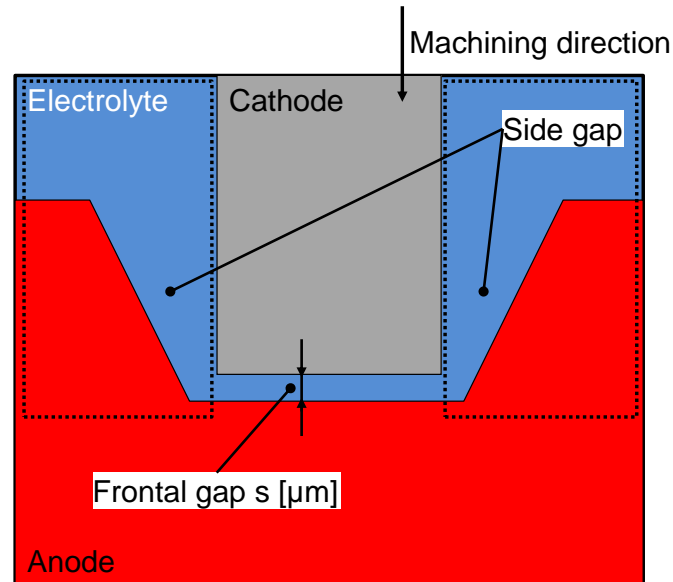


Figure 2-4 Designation of process specific terms

Based on Faraday's law, Equation 2-7 describes the resulting removal rate or velocity of the electrochemical dissolution based on the materials molar mass, valence and density in normal direction of the machining feed rate and an applied constant current density (in normal direction to the anodic surface) [42, 43].

$$v = \frac{M}{z \cdot F \cdot \rho} \cdot J \quad \text{Equation 2-7}$$

This relationship can be derived from Faraday's law as follows:

$$m = V \cdot \rho = \frac{M}{z \cdot F} \cdot I \cdot t \quad \text{Equation 2-8}$$

$$V = \frac{M}{z \cdot F} \cdot \frac{1}{\rho} \cdot I \cdot t \quad \text{Equation 2-9}$$

$$V = A \cdot h = \frac{M}{z \cdot F} \cdot \frac{1}{\rho} \cdot I \cdot t \quad \text{Equation 2-10}$$

With A describing the surface area and h the removal height in case of an ideal cylindrical anode, further considerations can be done:

$$\frac{h}{t} = \frac{M}{z \cdot F} \cdot \frac{1}{\rho} \cdot \frac{I}{A} \quad \text{Equation 2-11}$$

with  $v = \frac{h}{t}$  (assuming  $t = \text{const.}$ ) and  $J = \frac{I}{A}$

$$v = \frac{M}{z \cdot F} \cdot \frac{1}{\rho} \cdot J \quad \text{Equation 2-7}$$

The current density  $J$  is usually used, either in  $A/cm^2$  or in  $A/mm^2$ , since normalizing to an area allows a comparison between experiments using different surface sizes, and the current itself is one of the most important and modifiable parameters in Faraday's law when carrying out an experiment.

Also starting with Faraday's law, the material-specific components, sometimes also referred to as the electrochemical equivalent for a material, can be derived from Equation 2-7.

$$SMR = \frac{M}{z \cdot F} \quad \text{Equation 2-12}$$

$$MRR = \frac{M}{z \cdot F} \cdot \frac{1}{\rho} \quad \text{Equation 2-13}$$

The specific mass removal (SMR) in  $[mg/C]$  as well as the mass removal rate (MRR) in  $[cm^3/C]$  hereby represent material-specific coefficients. The relationship between the two introduced removal rates can be written as:

$$MRR = SMR \cdot \frac{1}{\rho} \quad \text{Equation 2-14}$$

Therefore Equation 2-7 becomes:

$$v = MRR \cdot J = SMR \cdot \frac{1}{\rho} \cdot J \quad \text{Equation 2-15}$$

It is obvious, that an essential factor for the use in production is still missing. While the velocity or removal rate is often synonymous with the feed rate applied in ECM, the factor allowing contemplations towards shaping accuracy comes from Ohm's law (Equation 2-16).

$$U = R \cdot I \quad \text{Equation 2-16}$$

U potential in  $[V]$ , R ohmic resistance in  $[\Omega]$

Ohm's law provides the information about the relation between the current and applied voltage in an electrically conductive medium. Since this conductive medium is represented by an electrolyte, a liquid solution, Ohm's law has to be adapted towards the present geometric properties in accordance to the setup. Assuming two parallel and equally sized opposing electrode surfaces at a distance  $s$  and a specific resistance of the electrolyte  $\kappa$  the resistance in the enclosed volume can be written as

$$R = \kappa \cdot \frac{s}{A} \quad \text{Equation 2-17}$$

$s$  distance between electrodes of a homogeneous conductor in [ $\mu\text{m}$ ],  $A$  cross sectional area in [ $\text{cm}^2$ ],  $\kappa$  specific resistance in [ $\Omega\text{cm}$ ]

By using the inverse relationship between resistance and conductivity

$$\kappa = \frac{1}{\sigma} \quad \text{Equation 2-18}$$

the overall resistance can be written as

$$R = \frac{s}{\sigma \cdot A} \quad \text{Equation 2-19}$$

$\sigma$  conductivity [ $\text{mS/cm}$ ]

With the combination of the relationships stated above, Ohm's law can be rewritten.

$$U = R \cdot I = \frac{s}{\sigma \cdot A} \cdot I = \frac{s}{\sigma} \cdot \frac{I}{A} \quad \text{Equation 2-20}$$

With  $J$  as the current density or current per surface area in [ $\text{A/cm}^2$ ]:

$$U = \frac{s}{\sigma} \cdot J \leftrightarrow s = \frac{U \cdot \sigma}{J} \leftrightarrow J = \frac{U \cdot \sigma}{s} \quad \text{Equation 2-21}$$

While the correlation is valid for ideal conditions, data reveal processes taking place between each interface of the electrodes and the electrolyte. Already mentioned in 1969 [23], the deviation in voltage between voltage applied and current measured at known electrolyte conductivity, is known as polarization voltage  $U_{\text{pol}}$ . It can be subdivided into a polarization voltage at the anode and at the cathode respectively, see Figure 2-5.

As experimentally determined, the polarization voltage shows a linear relationship with the current density  $J$  in  $\text{NaNO}_3$  [44, 45]. The cause for the polarization voltage can be seen in the reactions taking place at the electrode-electrolyte interface, which



lead to oxide formations or layers and hence additional resistances. The stability, reactivity and breakdown of such passive films [46], as well as the surface structure [47] and mechanisms of the anodic dissolution [6] are still in the focus of research [5, 48]. Models were developed describing layers on an iron surface in  $\text{NaNO}_3$  [48], with each of them showing different properties and resistances. Equally the same investigations revealed differences in valence of  $\text{Fe}^{3+}$  und  $\text{Fe}^{2+}$  under different electrical conditions [48, 49].

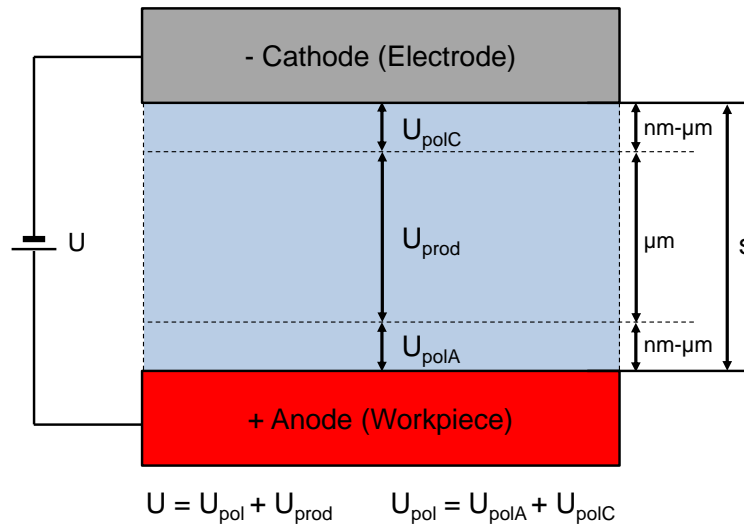


Figure 2-5 Polarization voltages at anode and cathode

Since the variable  $U$  is used for the voltage applied to the system overall, the variable  $U_{\text{prod}}$  is introduced in Figure 2-5 to represent the productive voltage describing the voltage in the ideal electrolyte system ( $U_{\text{prod}} = U$  in Equation 2-21 and previous equations) which directly correlates with the current and conductivity.

$$s = \frac{(U - U_{\text{pol}}) \cdot \sigma}{J} \quad \text{Equation 2-22}$$

Equation 2-22 shows the adapted form of Ohm's law taking  $U_{\text{pol}}$  into account. Since the layer thicknesses, leading to  $U_{\text{pol}}$ , are reported in the range of  $\text{nm}$  to some  $\mu\text{m}$  [48], the gap distance is not reduced by these layer thicknesses. Similar to [44], the polarization voltages, resulting from the cathode and anode material reactions will not be further investigated, since the machine used in later experiments resembles a two-electrode setup. Other than a three-electrode setup, used in [48] and developed in [50], this two-electrode setup does not allow a reference measurement towards a known potential. Therefore resulting effects from the electrode material ( $1.4301$  conductivity  $1.39 \times 10^7 \text{ mS/cm} \gg$  conductivity electrolyte  $\sim 70 \text{ mS/cm}$ ) cannot be measured and the polarization voltage has to be evaluated experimentally.

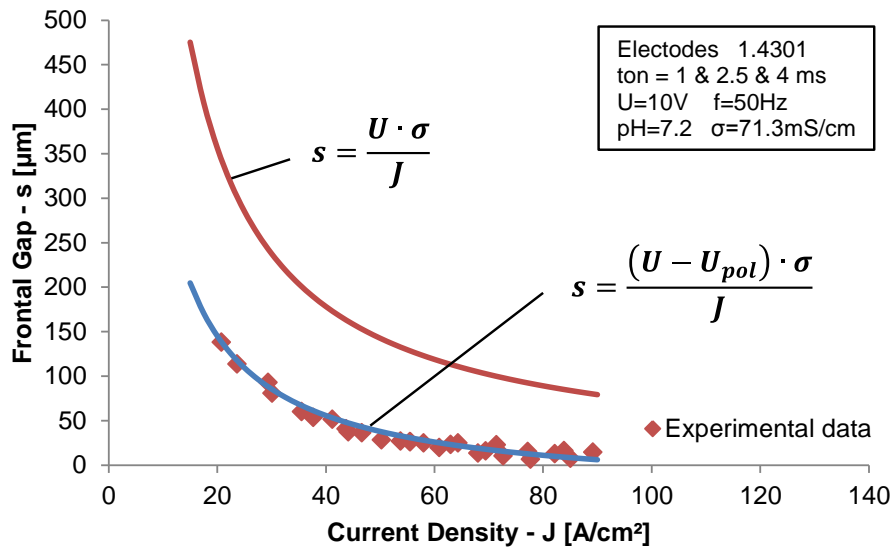


Figure 2-6 Example of a calculation with and without considering the polarization voltage

Figure 2-6 shows the application of Ohm's law with and without considering the polarization voltage at the example of experimental data. Only when considering  $U_{pol}$ , the experimentally determined relationship between current density and frontal gap relationship can be described correctly.

### 2.3 Electrolyte

The two main electrolytes used in ECM are sodium chloride NaCl [51] and sodium nitrate NaNO<sub>3</sub> [52]. Both have their unique characteristics. As schematically shown in Figure 2-7, NaCl has a consistent linear behavior over the complete range of current densities, while NaNO<sub>3</sub> does not. To understand the difference pictured, a current efficiency  $\eta$  in [%] has to be introduced. It describes the relationship between practical experiments and the dissolution expected, using the theoretical calculations based on Faraday's law.

$$\eta = \frac{m_{pract}}{m_{theor}} \cdot 100\% = \frac{SMR_{pract}}{SMR_{theor}} \cdot 100\% = \frac{MRR_{pract}}{MRR_{theor}} \cdot 100\% \quad \text{Equation 2-23}$$

$m_{pract}$  mass removed in practical experiments

$m_{theor}$  theoretical mass removed, calculated using Faraday's law

Using a NaCl-based electrolyte, the electrochemical reactions taking place in the interelectrode gap do not form stable oxides. Therefore the current efficiency follows a steady course, since the current in the process is used in the anodic dissolution following Faraday's law. In contrast to this simple reaction mechanism with no valence change, NaNO<sub>3</sub> based electrolytes can form stable oxides on the anode surface, which act as a passivation layer towards further dissolution [31, 48]. By applying high current densities, this layer or the underlying material can be dissolved

and the dissolution process intensifies with increasing current density. The basics on mass transport in high rate dissolution of iron in ECM electrolytes can be found for chloride solutions in [53] and for nitrate solutions respectively in [54].

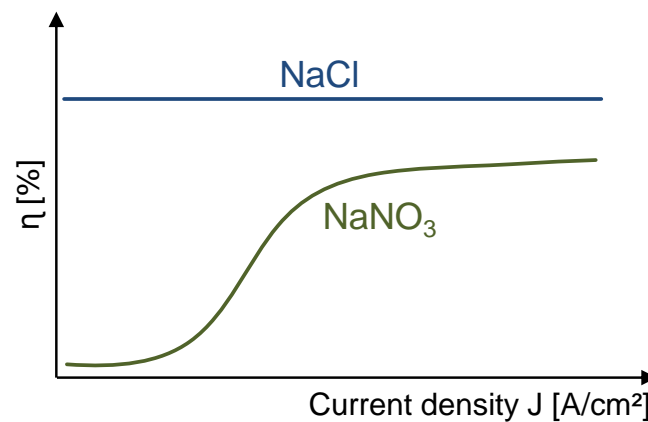


Figure 2-7 Schematic of the current efficiency using different electrolytes

In order to explain why this commonly used method to describe a material by its current efficiency, is neither useful nor suitable for the aim of this work, a closer look towards the valence in the theoretical part of Equation 2-23 is necessary.

At the example of the material 1.4301, composed of roughly 69 % iron (Fe), 18 % chromium (Cr) and 10 % nickel (Ni), the lack of quality in regard to the current efficiency, without a clear understanding or sources in literature listing the valences, is explained. The valence of chromium as machined in the underlying experiments is 6 (CrVI). Therefore the theoretical current efficiency will mainly be influenced by the valence of Fe as 2 or 3 and the valence of Nickel as 2 or 3 (see Table 2.1). The four combinations possible are pictured in Figure 2-8 and a value referred to as 'Mean' is defined as the average towards the valence values of iron and nickel. The individual values (red dots) indicate experimental results and the lines depict the theoretically calculated SMR values based on the combinations as highlighted in the legend. Looking at the calculated current efficiency values in the figure, the deviations are in a range of up to 30% from the lowest to the highest values assuming variations of valences. The method used cannot explain dissolution ineffective reactions, which just result from a loss of mass of nonconductive material. However, the current efficiency provides a quantitative assessment under known constraints. The theoretical considerations can provide evidence when values of 100% and above are calculated using faulty assumptions. Since the values can only be put in context, when knowing the correct valences for each current density value, all material dissolution results in this work will be based on measurable and comparable values as SMR in [mg/C].

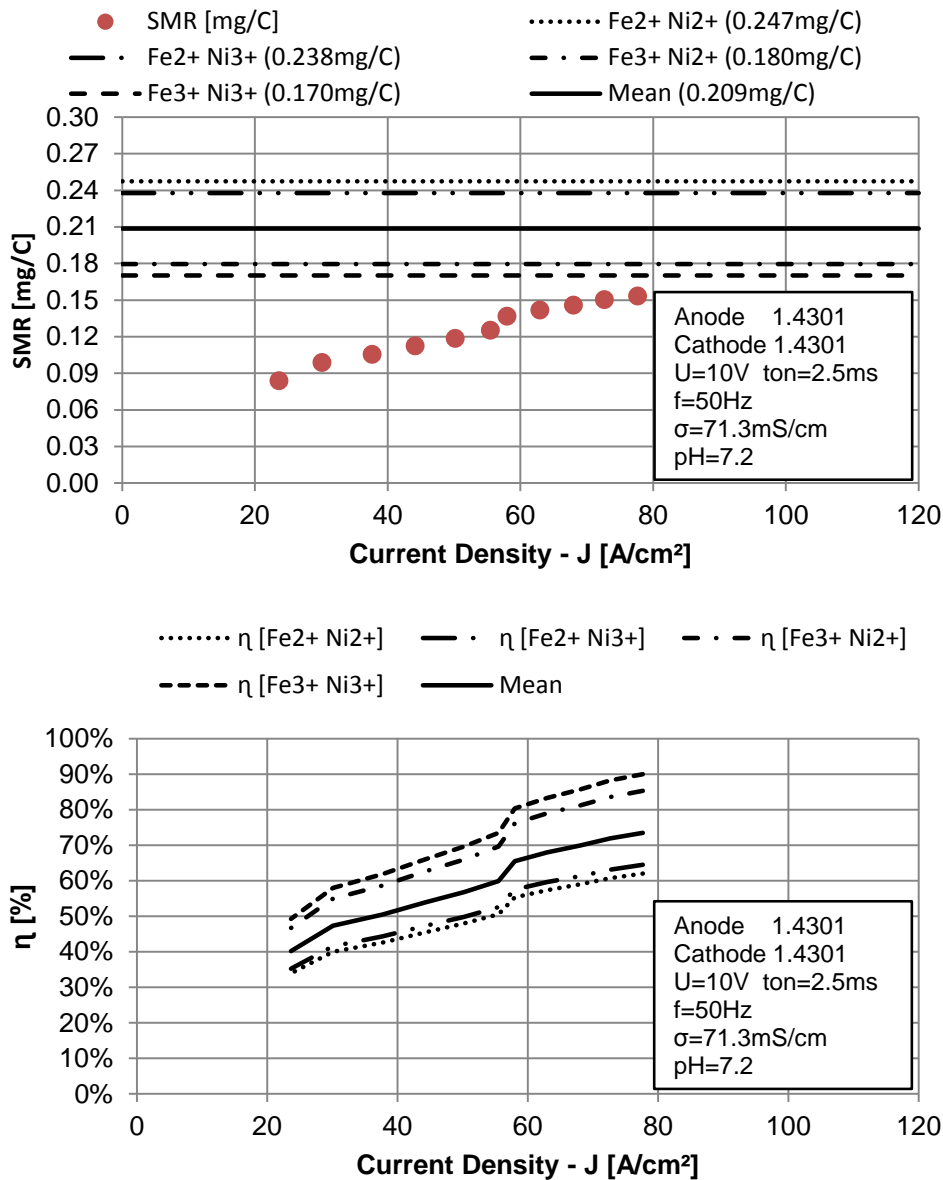


Figure 2-8 Effects on the current efficiency under the assumption of different valences

To explain the geometric shaping in ECM using either NaCl or NaNO<sub>3</sub> as electrolyte, the following section will focus on a theoretical model, which is figuratively supported using Figure 2-9. Neglecting the polarization for purposes of explanation, the relationship describing the gap size using no feed of the tool can be found in Equation 2-21.

As initial condition a small gap is assumed and the voltage and conductivity are assumed to remain constant. Hence, the gap and current density are inversely proportional  $s \sim 1/J$ .

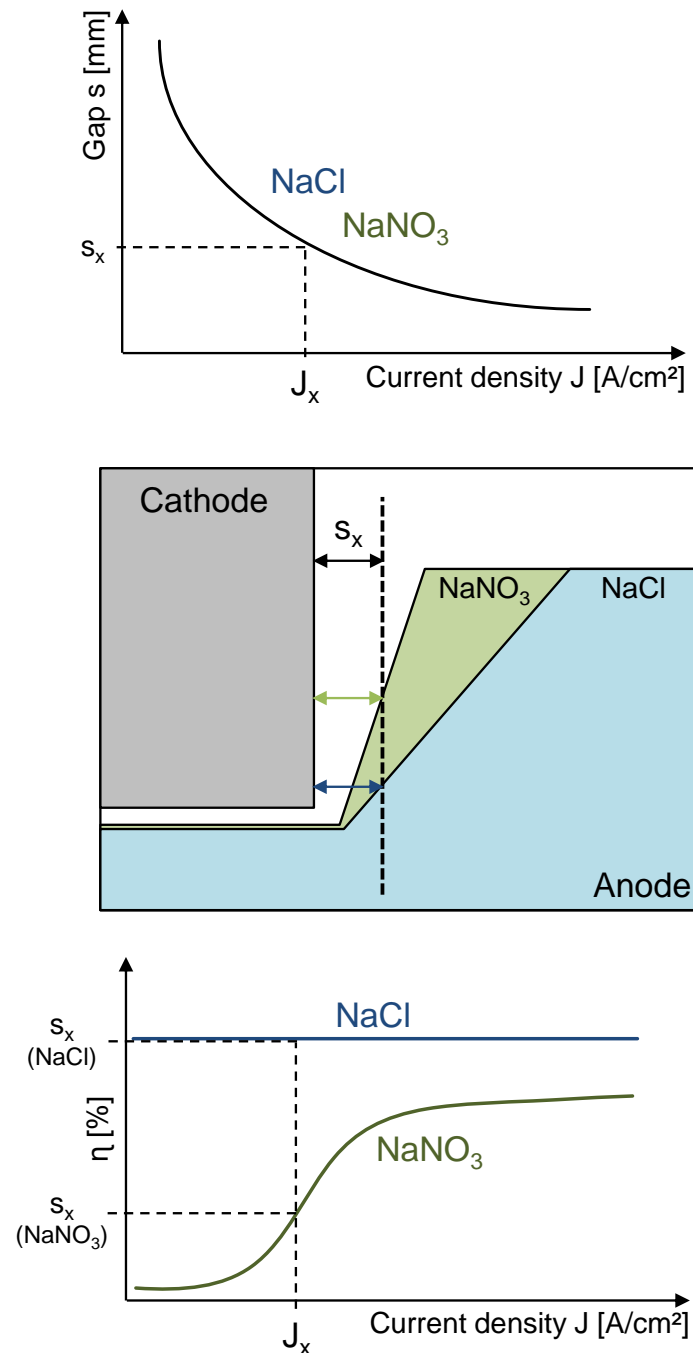


Figure 2-9 Difference in side gap evolution using a NaCl or NaNO<sub>3</sub> based electrolyte (Assumption: equal conductivity)

The correlation, which is based on Ohm's law, is displayed in the upper illustration. Indicated with  $s_x$  the distance displayed in the middle is also equal, yet through the differences in current efficiency, the amount of material dissolved with proceeding time is different. At an imaginary time step later, the gap in both cases will be bigger than displayed, yet when only using NaCl the dissolution rate will remain constant, even when the current density drops, due to the  $s \sim 1/J$  relationship. Regarding NaNO<sub>3</sub>, the current efficiency and hence also the material removal rate will further decrease as time proceeds.

In this work, only water-based technically pure  $\text{NaNO}_3$  by manufacturer Kirsch Pharma GmbH [55] is used. The water is taken from a reverse osmosis process, using an Aqua Medic Merlin II by company Aqua Medic. The measured conductivity of the water going into the machine used in the experiments before adding the  $\text{NaNO}_3$  was on an average measured at  $\sigma = 58 \mu\text{S}/\text{cm}$ . It is known, that the pH-value and concentration of the electrolyte have an effect on the reaction products, mechanisms and copying accuracy [56], yet considering the objective of this work only experiments with a constant pH value and constant concentration in the inflow of the process chamber are conducted.

The conductivity considerations in this work are carried out using published empirical data [44]. Herein, the relation between conductivity, temperature and concentration of  $\text{NaNO}_3$  dissolved in demineralized water was concluded as follows:

$$\sigma = a \cdot C^2 + b \cdot C + (c \cdot C^2 + d \cdot C) \cdot T \quad \text{Equation 2-24}$$

with

$\sigma$  = conductivity [mS/cm]  
 $C$  = electrolyte concentration [g ( $\text{NaNO}_3$ )/l]  
 $T$  = electrolyte temperature [ $^{\circ}\text{C}$ ]

and the constants derived as the following values:

$a = -0.0000755$   
 $b = 0.0523$   
 $c = -0.00000338$   
 $d = 0.00200$

## 2.4 Pulse Electrochemical Machining – PECM

The Pulse Electrochemical Machining (PECM), schematically shown in Figure 2-10, is a variation of the ECM process. During this process, the feed towards the work piece is overlaid with a mechanical oscillation of the tool [57]. The oscillation amplitude of the machine used is  $200 \mu\text{m}$ , which results in two different process phases. During the minimum gap size, a pulsed current with a pulse duration ranging from 0.1-5 ms can be applied. The small gap size, achievable through the oscillation of the cathode and short current pulses of up to 8,000 A, lead to an effective material removal process resulting in good surface quality and precise copying accuracy [37]. The upward movement during the oscillation results in the phase of maximum gap size, which enables enhanced flushing possibilities and consequently a better removal of the processed material as compared to the conditions at minimum gap size. While this process using just electrical pulses was already described by Degenhardt in 1972 [11], a patent in 1979 [58] described the method and system using a mechanical vibration overlaid with the electrical pulsation. It was not many years later, that first results of experiments under pulsed current conditions were published [59] and variations and use cases were reported [31, 60, 61]. Especially the focus on new developments in ECM [37] and studies of ECM utilizing a vibrating tool electrode [62, 63] gave an insight to the new possibilities this process opened. In 2009 the PECM application area was described with the potential of processing in an

interelectrode gap ranging from below 1 mm to over 1  $\mu\text{m}$  [64]. With the possibility of continuous machining at such small gaps the replication accuracy has been increased tremendously. Furthermore the use case for micro-structuring was examined [65] and a better fatigue life than Electrical Discharge Machining (EDM) has been reported [66].

In these days suppliers and users of PECM, amongst others, companies like PEMTec SNC, Kennametal Extrude Hone, EMAG ECM GmbH, Imato Industrial Solutions and Philips Consumer Lifestyle.

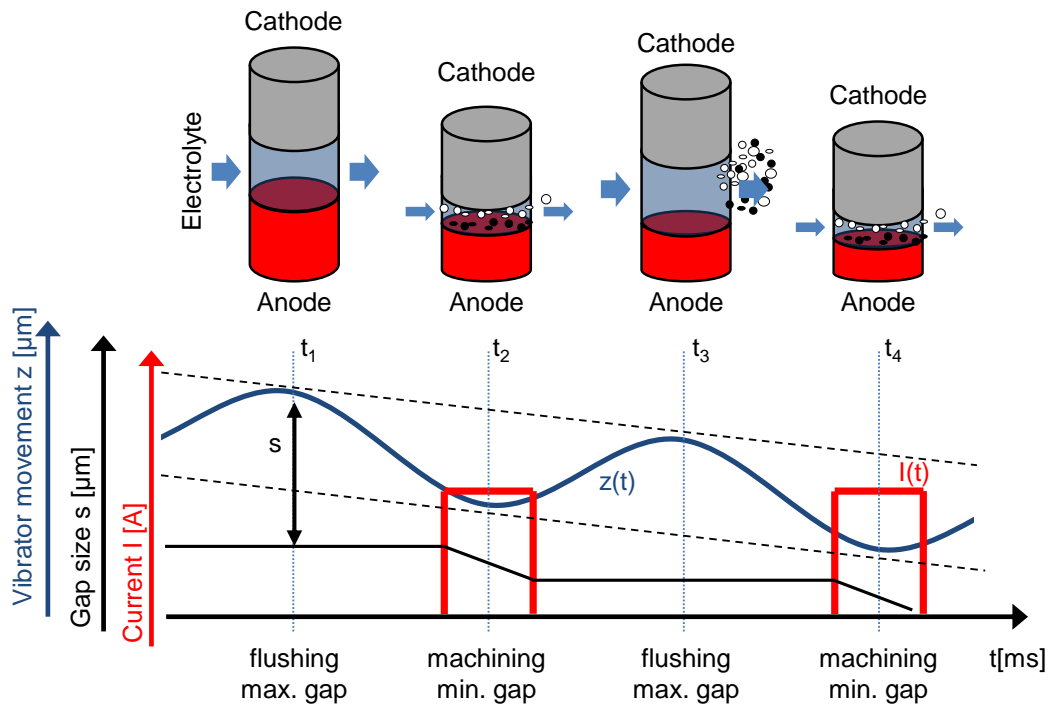


Figure 2-10 Schematic of the PECM process

In the underlying technology one oscillation period  $T$  is divided into a pulse on time  $t_{\text{on}}$  [ms] and a pulse off time  $t_{\text{off}}$  [ms], compare Figure 2-11. A duty cycle can be defined as the coefficient of  $t_{\text{on}}$  divided by  $T$ . Using a 50 Hz oscillation frequency,  $T$  equals 20 ms and assuming a pulse on time between 1 ms and 4 ms, the duty cycle calculates to only 4-20 %.

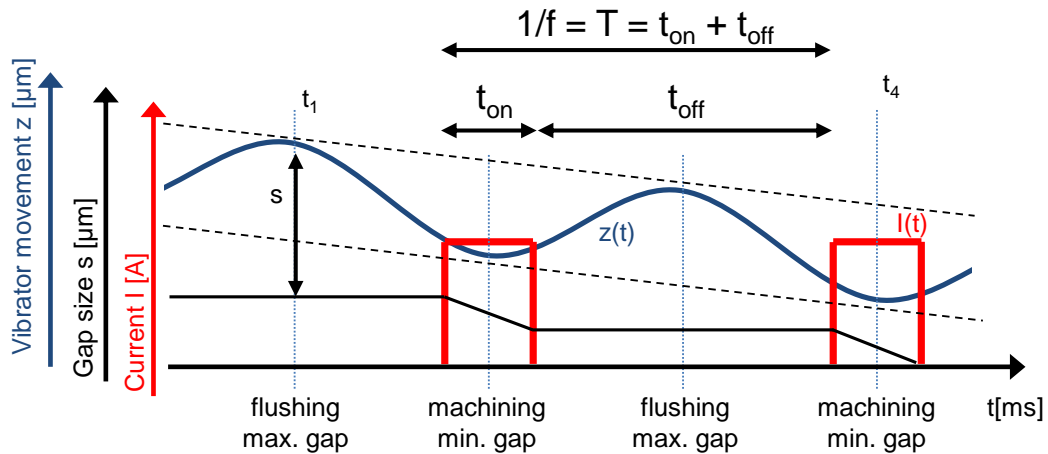


Figure 2-11 Time-dependent variables

To increase or change the machining rate and duty cycle other pulse-pause cycles are possible by using

- longer pulses or multiple pulses during one oscillation [37, 67, 68]
- rectangular, exponential, saw or triangle pulses [69]
- a programmable movement of the cathode with a higher down time and localization of the anode surface through touching of anode and cathode before applying multiple pulses. When a change in the parameters is detectable and the gap is filled with hydroxides, then parameter specific lifting of the cathode and flushing of the gap or adjusting to a certain surface condition [70] can be performed

Since PECM can be regarded as a discontinuous ECM process, when using rectangular pulses, all formulas introduced can be adapted by considering a constant factor composed of the pulse on time and the pulses per time unit, which is in this case defined by the frequency  $f$  of the sinusoidal oscillation. The ideal Faraday's law is therefore adjusted by considering the pulse on and pulse off cycle

$$Q = I \cdot t \cdot t_{on} \cdot f = \frac{m \cdot F \cdot z}{M} \quad \text{Equation 2-25}$$

In contrast to the equations in ECM, here  $t$  corresponds to the uninterrupted machining time and  $t_{on}$  to the length of each current pulse. The connection between feed rate and current density can be written as

$$v = \frac{M}{z \cdot F \cdot \rho} \cdot J \cdot t_{on} \cdot f \quad \text{Equation 2-26}$$

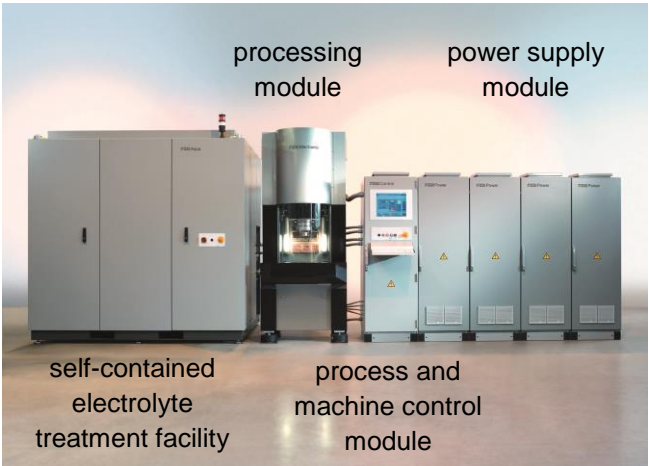
The influence of time during a pulse is not considered. The reason can be seen in the fact that the material height removed during each pulse in feed direction, is again fed in equal amount during the pulse off time, which resembles the equilibrium state of the process in feed direction. In this way, every pulse is each time triggered at an



equal frontal gap after the processing gap has been regenerated with electrolyte after each oscillation.

The PECM machine used in all experiments was a PEMCenter8000 (installed 2011) by company PEMTec SNC, France. The main technical data is listed in Figure 2-12. A similar machine was already used by Förster in 2004 [4], yet many changes in the mechanical and electrical concept do not allow a comparison of data. The preparation of the electrolyte in terms of conductivity, temperature and pH value occurs automatically in the processing unit. These parameters can therefore be regarded as constant input parameters or boundary conditions. The temperature compensated conductivity was measured in the experiments in the range of  $\sigma = 71.5 \pm 1.5$  mS/cm and the pH was kept constant between pH 7.1 and pH 7.3. Furthermore the machine is equipped with a bipolar unit. This unit allows a polarity switch [31, 71], which was patented as a method for on-line removal of cathode depositions during the electrochemical process [72]. This unit was not used, yet during the pulse pauses a voltage of  $U = 2.7$  V at a maximum current of  $I_{\max} = 120$  mA is applied [48].

Technical Data	
Current $I$ [A]	up to 8,000
Voltage $U$ [V]	up to 18.7
Pulse on time $t_{\text{on}}$ [ms]	0.1 - 5
Mechanical Oscillation $f_{\text{mechanic}}$ [Hz]	5 - 60
Electrical pulsation without mechanical oscillation $f_{\text{electric}}$ [Hz]	1 - 200
Feed rate $v_f$ [mm/min]	0 - 2
Electrolyte pressure [kPa]	100 - 1,000
Electrolyte	$\text{NaNO}_3$
(common) pH-value	6-9



PEMCenter8000 by company PEMTec SNC,  
Forbach, France

Figure 2-12 Technical constraints of the equipment used in the experiments

As a special feature of the machine used, a parameter variation has to be mentioned. The shift in Phase  $P_{\text{shift}}$  [%] - as shown in Figure 2-13 - relates to the shift of the pulse on time in relation to the bottom dead center of the mechanical vibrator. The starting time  $t_{\text{shift}}$  [ms] of the rising flank of the pulse on time can be calculated in relation to the point in time when the vibrator reaches the bottom dead center according to Equation 2-27.

$$t_{shift}[ms] = -P_{shift}[\%] \cdot t_{on}[ms] \quad \text{Equation 2-27}$$

The resulting effects on the process and the evaluation of experimental data will be discussed in more detail in chapter 5.1

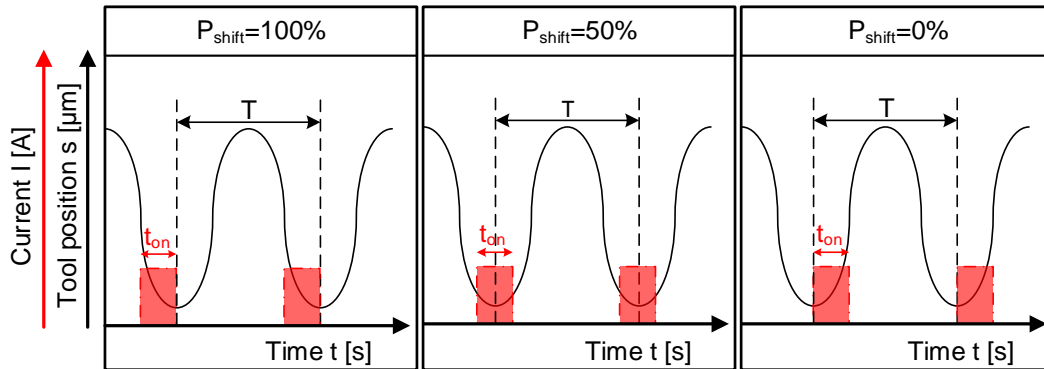


Figure 2-13 Shift in Phase of the current pulse in relation to the mechanical oscillations bottom dead center

### 3 Scientific concept and approach

The aim of this thesis is to present and validate a novel approach towards the specification and the use of material-specific data to improve the PECM process in terms of understanding the material specifics and providing an approach to simplify the iterative tooling process. The procedure used to gather the information up to the point of using it in a PECM simulations is schematically shown in Figure 3-1.

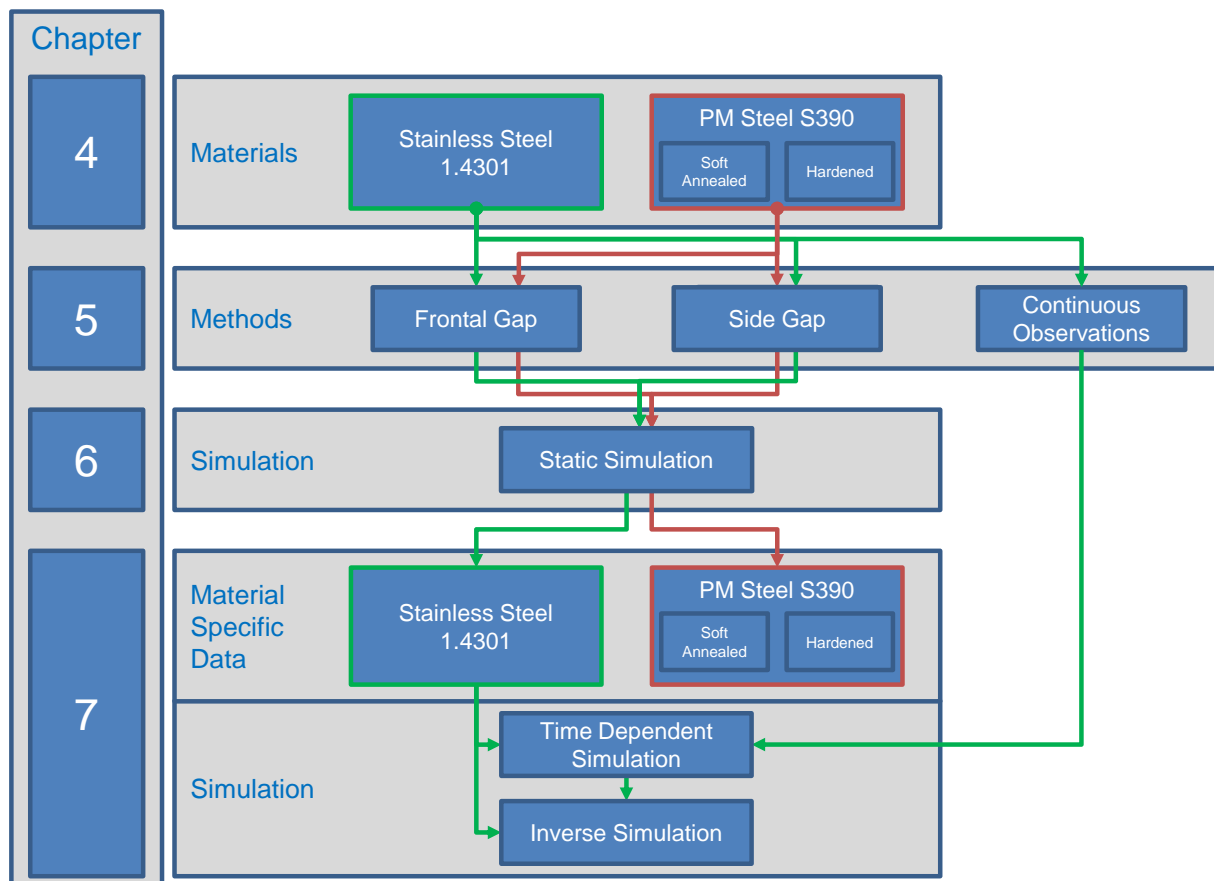


Figure 3-1 Information flow chart

Following the introduction, about the basics of ECM and PECM, two materials are introduced in chapter 4. One of the most widely used stainless steels (V2A) with material number 1.4301 and a powder metallurgical steel (PM Steel S390) in two different hardness states.

In order to investigate these two materials, three methods to gather production relevant material data using industrial-size machinery are presented in chapter 5. The methods used are introduced together with extensive tests focusing on mastering and understanding influencing machine parameters to ensure repeatability and process reliability. Based on the results, the parameter fields useable to ensure machine-independent results are restricted and by varying the main influencing

parameters the materials are characterized individually. The data acquired includes information about the dissolution rates, geometric precision and surface properties achievable.

In chapter 6 simulation concepts are introduced. Aside from the Finite-Element-Method (FEM) using commercially available software to validate and better understand the electrical parameters in a complex three dimensional experiment, a two dimensional simulation based on individual programming is presented.

With the possibility to validate experimental results and measurements using simulation, the material-specific data recorded is evaluated and discussed in chapter 7. Based on the material data for the stainless steel, the simulation concept is tested and validated towards experimental data recorded using the in-process observation setup.

In each chapter, its main content is summarized to highlight the key content. Also the topic specific information covering the state of the art and available knowledge from scientific literature are incorporated and, if possible, additionally supported and discussed using collected data and examples.

## 4 Investigated Materials

The investigated materials were selected according to the following criteria:

1. A stainless steel (1.4301) partially investigated using basic electrochemical methods as described in scientific literature was selected to assure the possibility of cross-referencing results, which are acquired through the novel experimental approach used.
2. A powder metallurgical (PM) steel in soft-annealed and hardened state was chosen to investigate the effects and results of machining in dependence of specific hardness and to investigate the resulting effects on the work piece surface and the geometric constraints in geometric shaping.

### 4.1 Stainless steel 1.4301

The stainless steel investigated was obtained at a conventional industrial metalware dealer, the Alois Schmitt GmbH & Co. KG, Germany. The material was processed and investigated as delivered. No further treatment or conditioning was conducted. The outside diameter was 6 mm with a measured tolerance in diameter of  $\pm 0.05$  mm. All samples were cut to a length of 70 mm and the front surface was turned and sanded to a roughness below  $R_a = 1 \mu\text{m}$  before the investigations.

The austenitic steel with the material number 1.4301 (also known as X5CrNi18-10, AISI 304 or V2A) was chosen, since it is one of the mainly used stainless steels and data is partially available in literature [4, 73, 74]. Yet, this data is mainly focused on the dissolution behavior under small-scale laboratory conditions. In addition, data can be found with regard to other similar stainless steels (e.g. [75]), which is helpful in the interpretation and comparison of the experimental data towards meaningfulness.

Table 4.1 Chemical composition of the austenitic steel 1.4301

Steel Symbol X5CrNi18-10	Element										Density [g/cm <sup>3</sup> ]	Data Sheet Density [g/cm <sup>3</sup> @20°C]
	Fe	C	Si	Mn	P	S	Cr	Cu	Ni	N		
Steel Number 1.4301	7.874	2.260	2.336	7.430	1.830	2.070	7.140	8.920	8.908	0.001		
	Composition [Weight-%]											
min	75.000	0.000	0.000	0.000	0.000	0.000	17.000	0.000	8.000	0.000		
max	65.760	0.070	1.000	2.000	0.045	0.015	19.500	1.000	10.500	0.110		
average	70.380	0.035	0.500	1.000	0.023	0.008	18.250	0.500	9.250	0.055		
Density [g/cm <sup>3</sup> ]	5.542	0.001	0.012	0.074	0.000	0.000	1.303	0.045	0.824	0.000	7.801	7.766
ICP-OES	68.890			1.920			17.720	0.330	10.160			
Density [g/cm <sup>3</sup> ]	5.424	0.000	0.000	0.143	0.000	0.000	1.265	0.029	0.905	0.000	7.767	7.766

Using optical emission spectrometry with induced coupled plasma (ICP-OES) the composition of 1.4301 was determined at the Institute of Physical Chemistry (German: Lehrstuhl für Physikalische Chemie) of the Saarland University. Table 4.1 shows the chemical composition, as published in the Landolt-Börnstein Database [76] and the results derived using ICP-OES. It was found, that the density calculated

based on the ICP-OES measurements and the composition itself is in close relation with the data sheet values.

In Figure 4-1 the results of micrographs are displayed. The images were taken with an Olympus LEXT OLS3100 Confocal Laser Scanning Microscope with integrated optical microscope and a Keyence VHX 500 F digital microscope both located at the Institute of Production Engineering at Saarland University. All metallographic results and sample preparations to verify the austenitic microstructure with carbide precipitates in the grain and at the grain boundaries were carried out with the consultation of the expert staff at the Department of Functional Materials (German: Lehrstuhl für Funktionswerkstoffe) of the Saarland University.

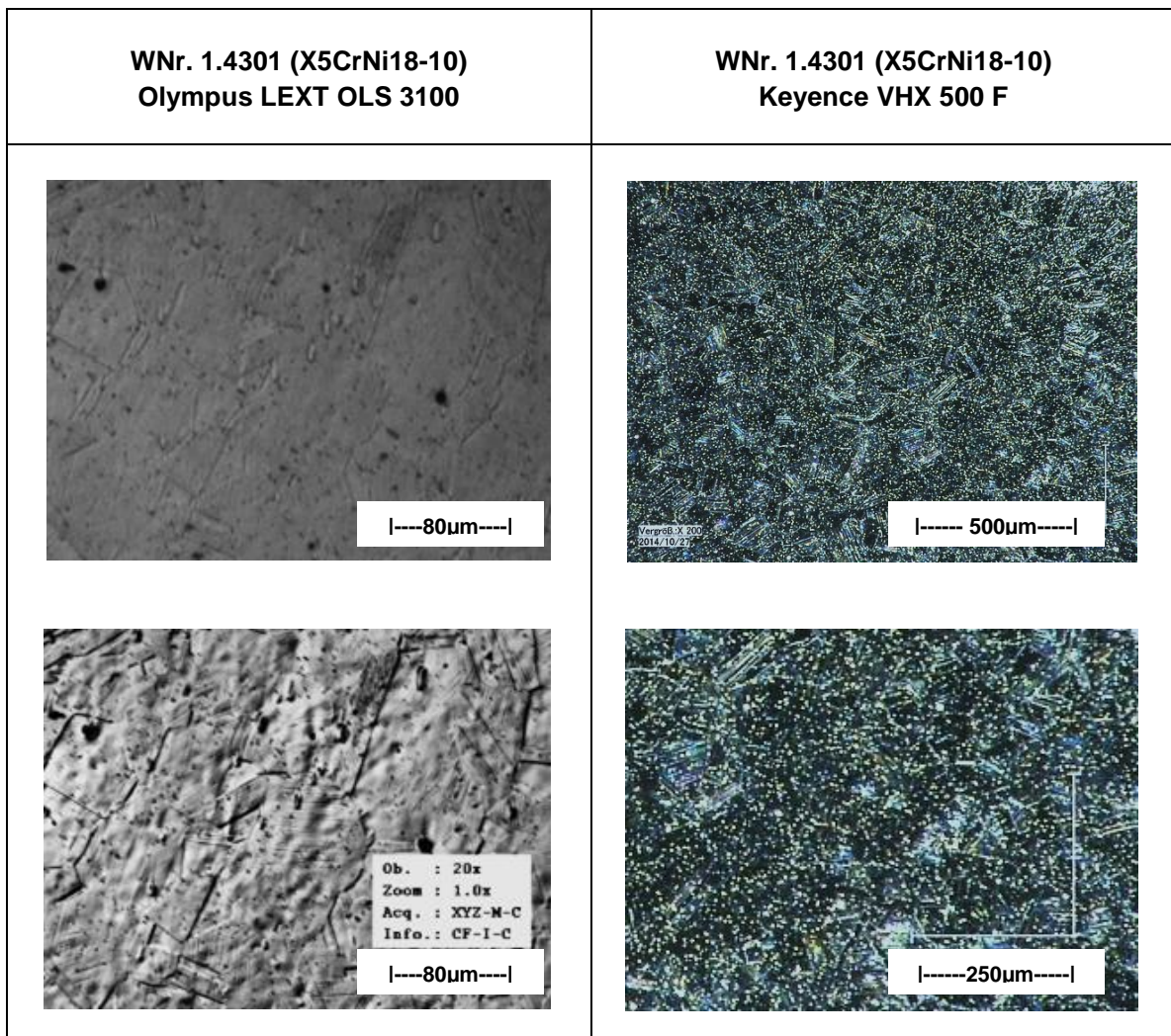


Figure 4-1 Optical micrograph images 1.4301 using a  
 lhs: confocal laser scanning microscope  
 rhs: digital microscope

## 4.2 Powder metallurgical steel S390

A powder metallurgical (PM) steel with the abbreviation S390, from the manufacturer BÖHLER-UDDEHOLM Deutschland GmbH, with a relatively high amount of tungsten, see Table 4.2, was investigated in soft-annealed and hardened state. This material was chosen in order to investigate the effects and results of machining in dependence of its hardness and to investigate the effects on the surface roughness and the geometric constraints in geometric shaping. The applications of this specific material can be seen in the machining of steels, as well as nonferrous metals such as nickel-base and titanium alloys and it can be used under extreme compressive stresses [77, 78].

Table 4.2 Chemical composition of the powder metallurgical steel S390 [78]

S390	Element											
	Fe	C	Si	Mn	P	S	Cr	Mo	V	Ni	W	Co
(Datasheet values)	7.874	2.260	2.336	7.430	1.830	2.070	7.140	10.280	6.110	8.908	19.300	8.900
	Composition [Weight-%]											
average	67.460	1.640	0.600	0.300			4.800	2.000	4.800		10.400	8.000
Density [g/cm <sup>3</sup> ]	5.312	0.037	0.014	0.022			0.343	0.206	0.293		2.007	0.712
measurement	66.854	1.630	0.300	0.260	0.018	0.018	4.910	2.280	5.120	0.200	10.090	8.320
Density [g/cm <sup>3</sup> ]	5.264	0.037	0.007	0.019	0.000	0.000	0.351	0.234	0.313	0.018	1.947	0.740

The material also came into focus, since it is commonly said, that a deviating hardness in the same material, due to its equal chemical composition, has no influence on the machinability using ECM. Yet, the question is often not answered or no sufficient data provided, if the machining parameters also stay equal. Profound investigations on this topic could only be found towards the investigation of stainless steels, which were published and presented by Hoogsteen [75, 79]. It was shown that there is nearly no influence on the electrochemical machining behavior under a variety of changing current densities, when the material was soft-annealed or in a hardened state. Other than the machining of hardened S390 under a narrow set of PECM parameters published in [80] and first basic investigations of PM steels (both company Böhler) of type M340 with a low and M390 with no tungsten content [4], no data is available concerning machining under PECM conditions and the comparison of behavior and parameters in the soft-annealed and hardened state.

In its delivery condition, the soft-annealed state, the company-provided samples are specified with a material hardness below 300 HB (approx. 300 HV30) and are stated with a possible material hardness of around 65-67 HRC (approx. 840-900 HV30). Prior to the experimental investigations, parts of these samples with an outside diameter of 6.3 mm were conventionally machined into cylinders with a length of 70 mm and afterwards externally hardened by the company eifeler Werkzeuge GmbH, Germany. The hardening process itself can be found in the material data sheet [78]. After the hardening, all samples were sanded and prepared for hardness measurements. The hardness tester used was a Wolpert Wilson Instruments Model 930N located at the chair of metallic materials (German: Lehrstuhl für Metallische

Werkstoffe) at Saarland University. For all samples a test force of 394.2 N, a hold time of 10 s and a Vickers indenter was used. The results of the measurements are presented in Figure 4-2 and Figure 4-3. The average hardness of the S390 samples, in the following referred to as S390 S, were measured to be in the range of 296.1 HV / 29.2 HRC.

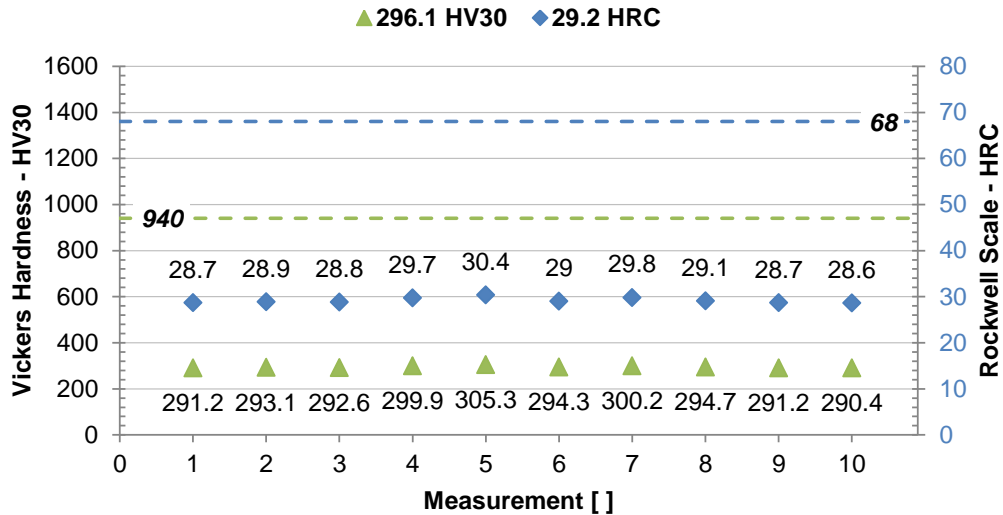


Figure 4-2 S390 in the soft-annealed state – average: 296.1 HV30 / 29.2 HRC

The hardened S390 samples, in the following referred to as S390 H, were measured in the range of 786.9 HV30 / 63.1 HRC. Even though the averaged results in the hardened state are below the values stated in the material data sheet, the difference in hardness between the two considered states is larger than a factor of two.

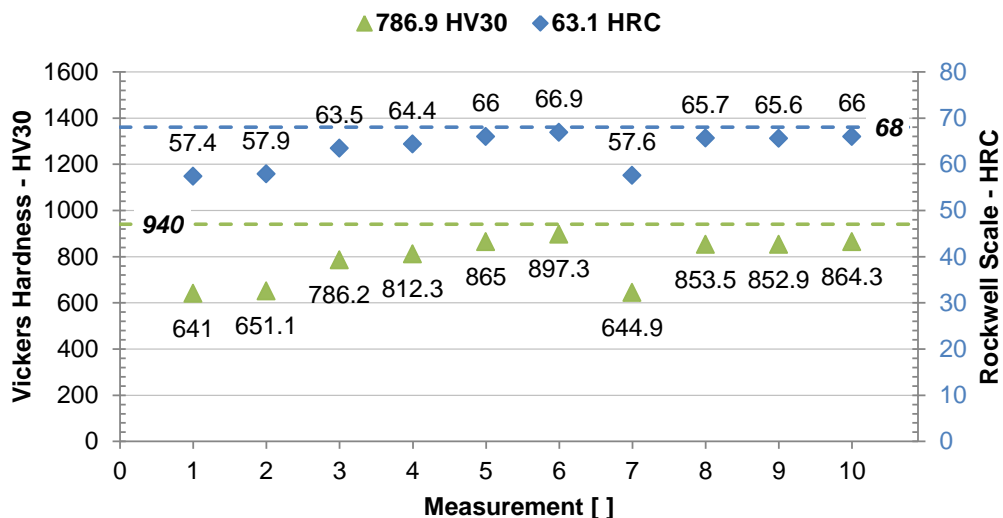


Figure 4-3 S390 in the hardened state – average: 786.9 HV30 / 63.1 HRC



### 4.3 Basic Electrochemical Analysis

Two of the most widely used techniques to acquire quantitative information about electrochemical reactions are the Cyclic Voltammetry and the Chronoamperometry:

- *Cyclic Voltammetry (CV) provides information on redox processes, heterogeneous electron transfer reactions and adsorption processes. It offers a rapid location of redox potentials of the electroactive species. The CV technique consists in scanning the potential of a stationary working electrode using a triangular potential waveform. During the potential sweep, the potentiostat measures the current resulting from electrochemical reactions occurring at the electrode interface and consecutive to the applied potential. The cyclic voltammogram is a current response plotted as a function of the applied potential. [81]*
- *Chronoamperometry, a controlled-potential technique, which measures the current response to an applied potential step. It involves stepping the potential of the working electrode from an initial potential, at which (generally) no faradic reaction occurs, to a potential at which the faradic reaction occurs. The current-time response reflects the change of the concentration gradient in the vicinity of the surface. Chronoamperometry is often used to measure the diffusion coefficient of electroactive species or the surface area of the working electrode. This technique can also be applied to the study of electrode processes mechanisms. [81]*

The Cyclic Voltammetry (Figure 4-4) as well as Chronoamperometry (Figure 4-5) were carried out using a BioLogic SP-150, by company Bio-Logic SAS (France), including a modular VMP3B-10 10A-Buster unit and the EC-Lab (v10.39) software. The results show a transpassive dissolution mechanism with a stable oxide layer on the surface of the materials.

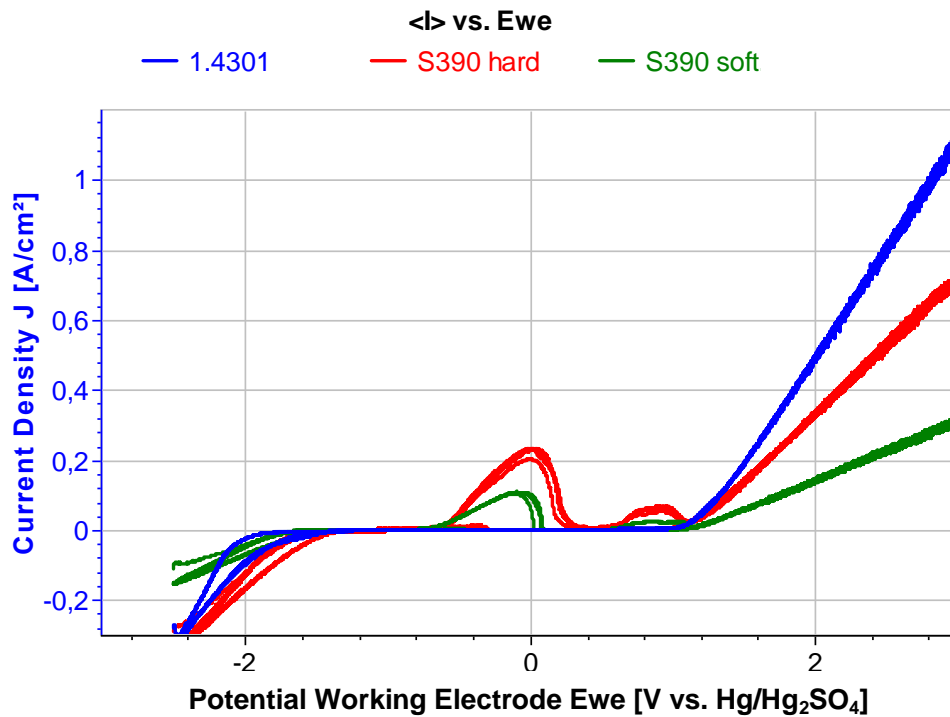


Figure 4-4 Cyclic voltammetry at a scanning rate of 20 mV/s

Conductivity and temperature were controlled before each experiment using a gauge GMH 3430 by Greisinger electronic GmbH. Since the electrolyte was prepared only once, the conductivity was measured at 71.8 mS/cm and the temperature at constant ambient laboratory temperature of 19°C. Using a digital-pH-/mV (Redox)-Meter GPHR 1400 A, also Greisinger electronic GmbH, the pH value was measured in the range of pH 7.3 - 7.4. The chromium VI, since taken from the PEMCenter8000 electrolyte processing tank, was at a content of CrVI = 4.8-5 mg/l. All materials investigated were pre-machined on a lathe and then sanded to achieve a surface roughness of below  $R_a < 1 \mu\text{m}$  at the front surface. After measuring the roughness and the exact diameter of each sample, all were insulated at the lateral surface using *SLOTOWAX Finish Coat* by the company Dr.-Ing. Max Schlötter GmbH & Co. KG, Germany. This coating was internally tested and provides even at a small layer thickness a long-term electrochemical protection in the electrochemical environment.

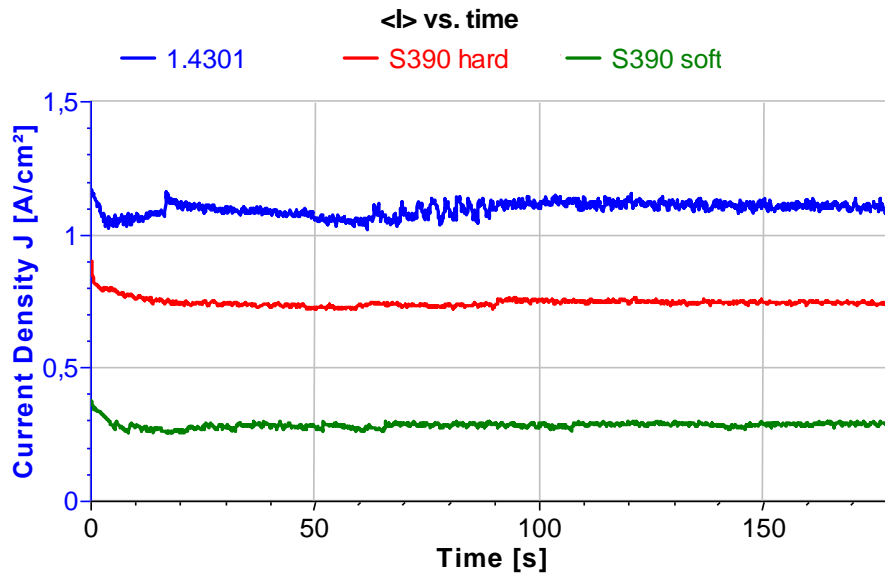


Figure 4-5 Chronoamperometrie at 3 V vs. Hg/Hg<sub>2</sub>SO<sub>4</sub> for 3 min

While no similarities to the quantitative data presented in Förster [4] towards 1.4301 could be found, the progression of the data in the case of the PM steel S390 is similar, yet not the same as the results presented in Degenhardt [11] and Lindenlauf [41], who investigated different PM steels. The question about comparability to PECM was already brought up by Förster [4], who pointed out the differences in processing using mainly DC voltage and ECM-like conditions. Yet at a later date, a micro flow cell was built by Möhring [50] which allows faster electrolyte flow velocities and overall PECM-closer investigation conditions. Since in this work industrial boundary conditions and currents well past the boosters capabilities of 10 A were reached in PECM, no direct conclusions to the experiments performed can be drawn. While Altena [82] discusses the efficiency profile during the pulse, it still seems unclear how the process states change during the pulses, if it follows the same path through the current efficiency curve at each pulse or if it jumps from one state into the other due to the fast current rise times and how the conditions during the pulse off time influence the following dissolution.

The cyclic voltammetry with a maximum voltage increase rate of 20 V/s, using the available BioLogic hardware, is not comparable to PECM with an increase of 17.5 V in a rise time between 200-300  $\mu$ s, which equals an equivalent of about 58.333 - 87.500 V/s. Therefore the basic electrochemical analysis methods are not directly applicable to determine the electrochemical behaviors of the material under PECM conditions especially since the pulse off time is not considered. Only the results from Chronoamperometry (compare Figure 4-5) allow the conclusion, that the materials investigated show no permanent material passivation when applying a DC voltage for a longer time period.



## 5 Investigation Methods

In literature different methods are used to characterize materials using ECM or PECM. To determine and evaluate material-specific parameters, most of the experimental setups are based on laboratory conditions and have limited electric boundary conditions [11, 41, 50, 65, 73, 83]. In most cases the current density is limited well below  $100 \text{ A/cm}^2$  ( $100 \text{ A/cm}^2 = 1 \text{ A/mm}^2$ ). Series production conditions with either a focus on shaping or material behavior can only be found in recent publications [44, 68, 84]. Since none of the laboratory scale setups offer the possibility to upscale the components, a comparatively simple and cost-efficient test setup was conceived to acquire material data. This setup for the collection and comparison of material data is based on the idea to meet the three most important measurable criteria in the PECM process, with the focus set on the field of production engineering:

- Material dissolution following Faraday's law, as qualitative calculation for the theoretical efficiency and the quantitative, practical machinability, using the SMR value as indicator.
- The frontal gap and side gap evolution as indicators for the size (precision) and geometry achievable in PECM.
- The resulting surface of the work piece under different current density conditions.

To meet these three criteria a setup had to be realized, which allows an understandable, reproducible and reliable collection of data under a wide range of parameters. Since frontal gap and side gap evolution are concurrent processes, they have to be investigated individually. For this purpose, two kinds of experimental procedures are used:

- One setup is used to investigate all of the above mentioned criteria with the focus on
  1. Faraday's law
  2. Frontal gap and side gap
  3. Surface topology
- Continuous observations (videos) are used to take into account the factor time, since most of the experimental procedures mentioned above are rather snapshots, or integral considerations of the process, and are rarely able to reproduce interfering or concurrent processes in just one experiment.

These two setups, their calibration and limitations to certain parameter ranges are discussed in this chapter. The evaluation of the work piece surface and topology is primarily a standard follow-up process using metrology well established in production engineering and will be roughly discussed at the end of the chapter.

### 5.1 Frontal gap experiments

An experimental procedure focusing on shaping, presented in Figure 5-1, is inadequate to differentiate between effects resulting from the partitioning of the total current into the current through the frontal gap and the effects caused by the current through the side gap. This is because the side gap increases continuously and therefore also the surface area on the sides of the cathode increases. Hence, the current density is inconsistent over the course of the experiment, since an increase in side gap and surface leads to a further drop in the  $\text{NaNO}_3$  current density versus the current efficiency curve.

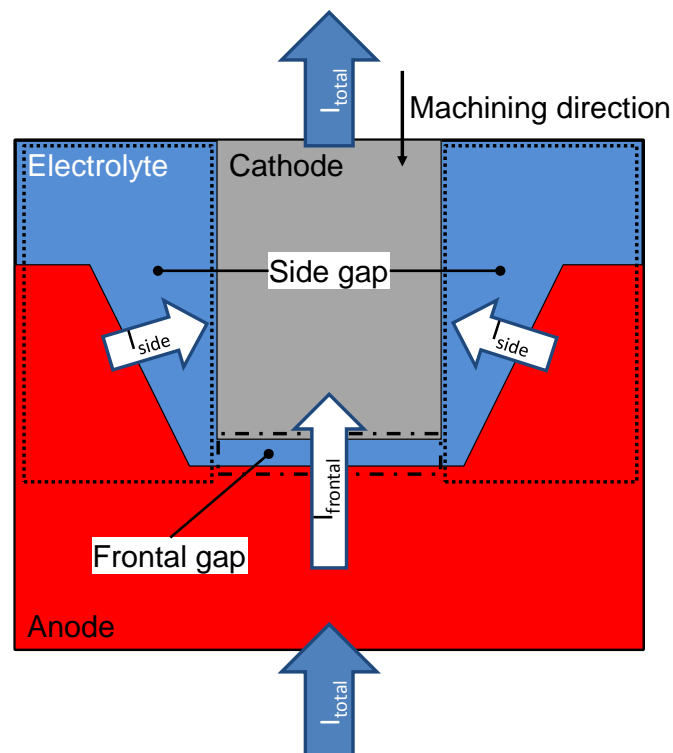


Figure 5-1 Schematic of a conventional frontal and side gap experiment

Due to the stated reason, a novel and simple experimental setup was devised, which does not completely reduce the effects of the side gap, yet results in a constant side gap effect during the course of the experiments. This constant effect can then be taken into account using appropriate measures, in this case FEM simulation. The setup used is presented schematically in Figure 5-2 and Figure 5-3. The flushing chamber pictured in Figure 5-3 is fed with the cathode towards the anode to assure equal flushing conditions at all time. It is made from additive manufacturing and is therefore electrically isolated. Similar to the schematic in Figure 5-2, it is constructed to cover almost the complete lateral cathode and anode surfaces. By retracting the cathode and connected flushing chamber, the cathode surface can be cleaned after each experiment and the anode material can be changed using a quick-change system from company EROWA, Switzerland, with a repeatability of 5 microns.

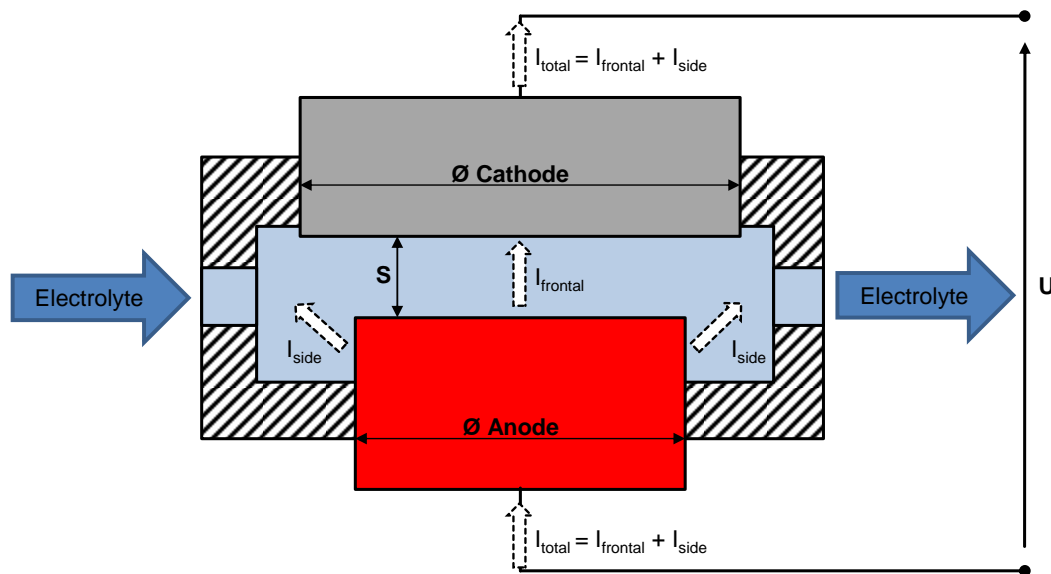


Figure 5-2 Experimental setup schematic

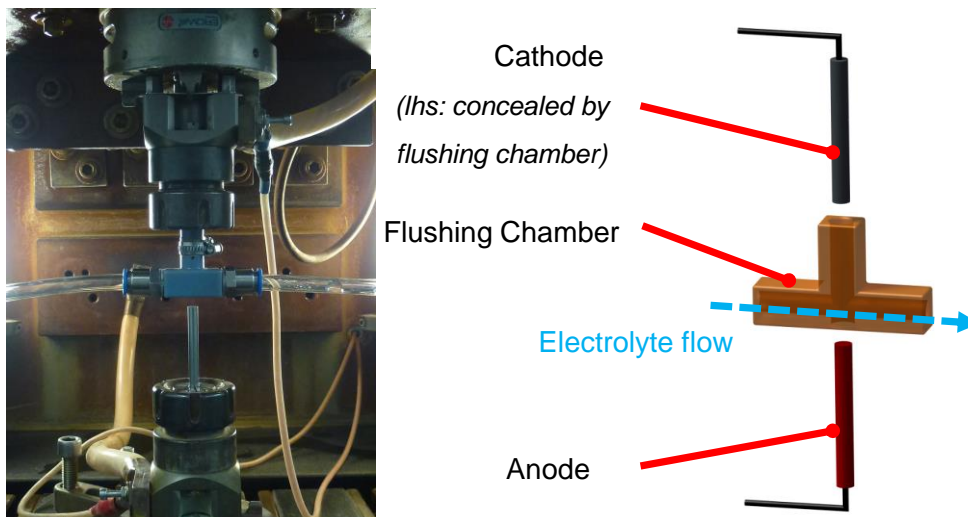


Figure 5-3 Experimental setup

To prevent effects resulting from a bent-up of the machine's C-frame design, a small contraction was used. The material and geometry of the electrodes used in the experiments are listed in Table 5.1. Each anode and cathode was prepared before each experiment towards a surface roughness  $R_a < 1.5 \mu\text{m}$ . The flushing is done from one side to the other using the machine's standard electrolyte supply connections.

Table 5.1 Anode and cathode combinations in the experiments

Anode		Cathode	
Material	Diameter [mm]	Material	Diameter [mm]
1.4301	6	1.4301	8
S390	6.3	1.4301	6.3

The use of a complete self-construction in combination with the machine's integrated technology, a mechanically driven, synodically oscillating vibrator, makes it necessary to test this structure and combination extensively. It must be ensured that the device provides precise and reliable data. For this purpose, known phenomena from literature have been tested regarding the gap behavior over time and parameter variations to uncover potential limiting machine conditions.

For a correct determination of the current density in the frontal gap [85], implied as a rectangular current pulse presented in Figure 2-10, a simulation-based calculation is presented for compensating the current through the lateral surface of the geometry in the following chapter 6. However, the findings and implications for the experimental data contained therein have already been taken into account in the following representations. By using the machine's integrated measurement capabilities for frontal gap distance and process current the following investigations neglecting the effects of pH and temperature [54, 86] are performed.

Looking at Faraday's law towards processing in a single direction, two aspects using PECM have to be pointed out:

1. Equilibrium conditions are reached, when the dissolution rate and the feed rate are equal. In case of the interelectrode gap in feeding direction this means that the gap will remain constant, once the equilibrium is reached. In the case of frontal gap experiments the indication of this process state is a constant current during constant feed. In contrast to the ECM process, in the PECM process the gap will only widen during each current pulse. Yet on a large time scale this resembles a quasi-continuous process, see Figure 2-10.
2. The equilibrium feed rate can be derived by Equation 2-26. Inferentially, the cathode has to be fed at a constant feed rate to match the dissolution rate at constant boundary conditions (e.g. electrolyte pressure and conductivity).

To measure the frontal gap distance, the cathode is fed towards the anode at a feed rate below 0.5 mm/min ( $\sim 8.33 \mu\text{m/s}$ ). By knowing the position of the cathode after the last current pulse, the distance is calculated automatically when cathode and anode touch each other. To prevent damage to cathode and anode, this is done at a low voltage of about  $U = 2.7 \text{ V}$  and at a maximum current of  $I_{\text{max}} = 120 \text{ mA}$ . The course of the current during the experiments is also recorded by the machine. However not each pulse but the current at a time interval of approximately 0.25 s is stored in an experiment-specific file. Thus, neither individual nor time-averaged current data is presented.

In order to investigate the effects of the machine's individual mechanical and electrical technology and the possible parameter variations, the following input variations are discussed using experimental data. Conclusions towards the reproducible recording of material data are made at the end of this chapter. The effects resulting from



- **pre-machining,**
- **choosing a false initial starting gap,**
- **a shift in phase (technology-specific),**
- **the mechanical oscillation frequency,**
- **and a change in input pressure**

will be specifically investigated using 1.4301 as anode and cathode material in the following.

To assure constant and repeatable processing independent of the **pre-machining**, the results of three consecutive experiments are presented in Figure 5-4. For each of the pictured experiments, the boundary conditions remain the same. These boundary conditions resemble the equilibrium conditions, which were obtained in a series of prior iterative experiments. Therefore the first experiment presented in Figure 5-4, indicated with a total charge of 469.5 Coulomb, is the result of the PECM machining using the specified parameters after the pre-machined sample was integrated into the experimental setup. It is obvious that the current rises to a plateau after roughly 250 s, before the expected equilibrium conditions are reached. When repeating the experiment two consecutive times, using the same parameters and without removing this sample, almost the same amount of charge is recorded, yet the current remains more and more constant and almost rectangular during each trial. This is the result of the surface changing towards the topology and surface roughness connected to the used parameter settings. As a conclusion, all samples which were turned and therefore have a different roughness before the first PECM machining passage, have to be machined at least once before conducting the actual experiment. Also, the experiments need to last long enough to achieve equilibrium conditions.

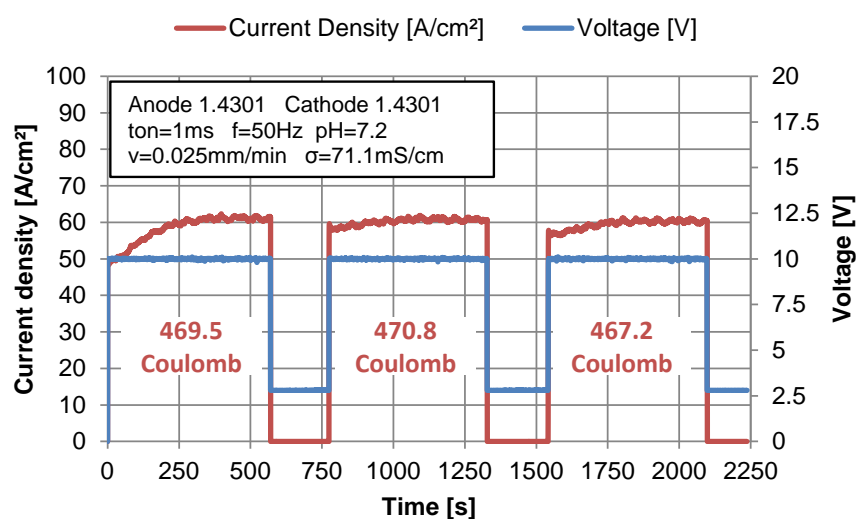


Figure 5-4 Machining 5.65 mm<sup>3</sup> (43.92 mg) of material for three consecutive times

Similar to this necessity of discarding the first machining trial after using a new sample, the initial starting gap is important to achieve comparable and stable results. Each experiment (= one rectangular form) in Figure 5-5 and Figure 5-6 shows how the current signal is influenced, when the sample is machined the first and second time using the equilibrium conditions and afterwards intentionally using **false initial starting gaps** at different pulse on times (Figure 5-5) and voltages (Figure 5-6). Using 1.4301 as material for anode and cathode the presented data shows the level-off effect towards a constant current density. For all experiments the feed rate and pulse on time were adjusted beforehand to achieve a uniform current density, between  $72 \text{ A/cm}^2$  and  $76 \text{ A/cm}^2$  for each process. As pointed out in literature [22], a process starting gap diverging from the equilibrium gap will either result in a widening of the gap and a parallel reduction of current density or a reduction of the gap, while at the same time the current density increases. This is easily explained through Ohm's Law and the correlation between feed rate and material dissolution rate. Since the process is set to a certain voltage and the conductivity remains the same, the current density and gap width are inverse proportional parameters, which will ultimately adjust to the predominant dissolution rate established through the feed of the cathode. The results therefore show how important the knowledge about the correct initial starting gap is, in order to run an experiment long enough to obtain a correct correlation between current density and frontal gap at given boundary conditions.

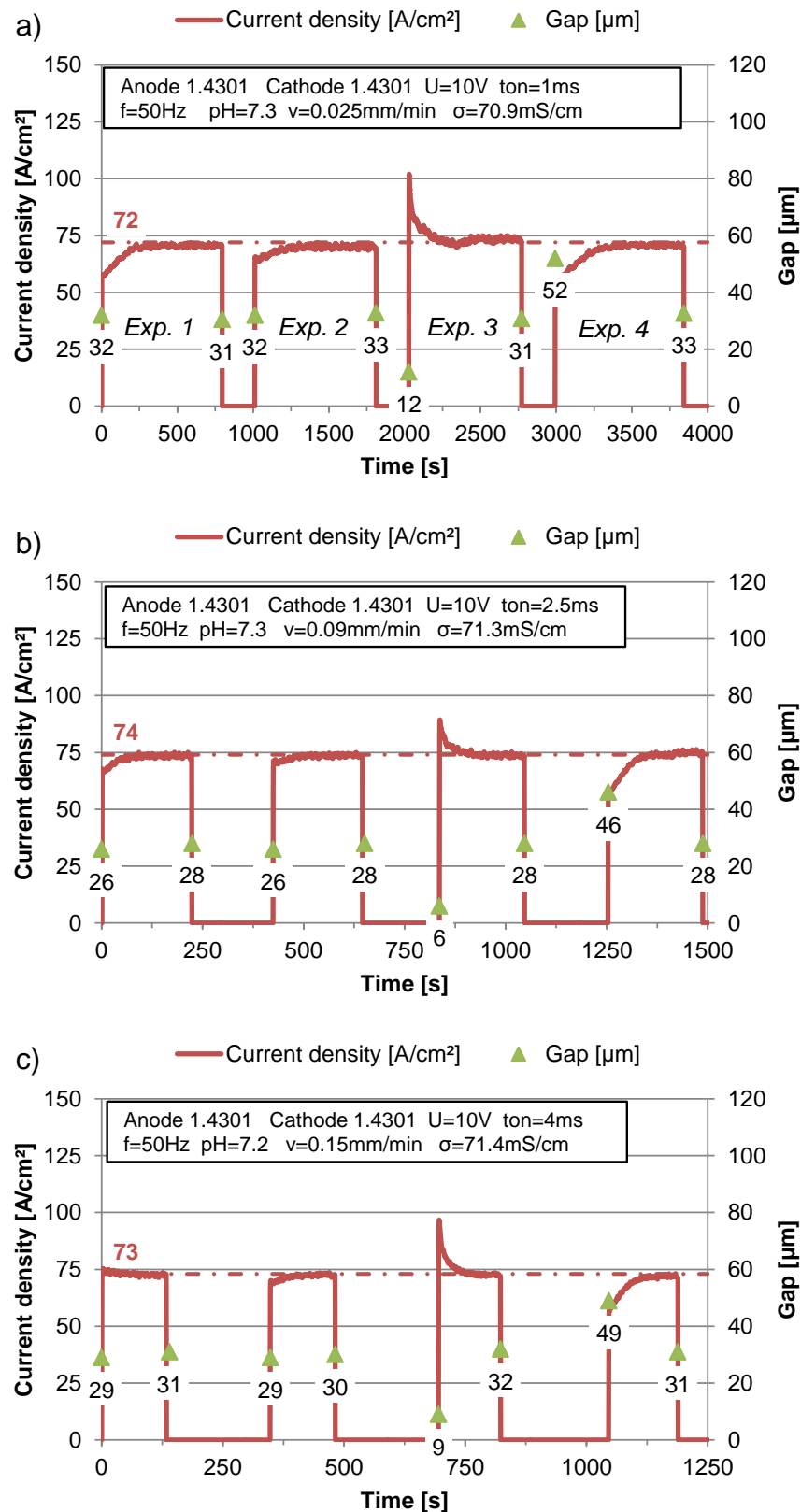


Figure 5-5 Effect of different starting gaps at three different pulse on times (a)  $t_{on} = 1$  ms, b)  $t_{on} = 2.5$  ms, c)  $t_{on} = 4$  ms) and equal current density at  $U=10V$

*Exp. 1: first PECM after sample preparation*

*Exp. 2: Starting gap = equilibrium gap*

*Exp. 3: Starting gap < equilibrium gap*

*Exp. 4: Starting gap > equilibrium gap*

The gap values presented here and throughout the chapters are averaged values taken from three consecutive contact measurements using a machine-implemented software building block. Herein the contact position of cathode and anode before machining is correlated to the position obtained after machining. This is done directly prior to and directly after each experiment.

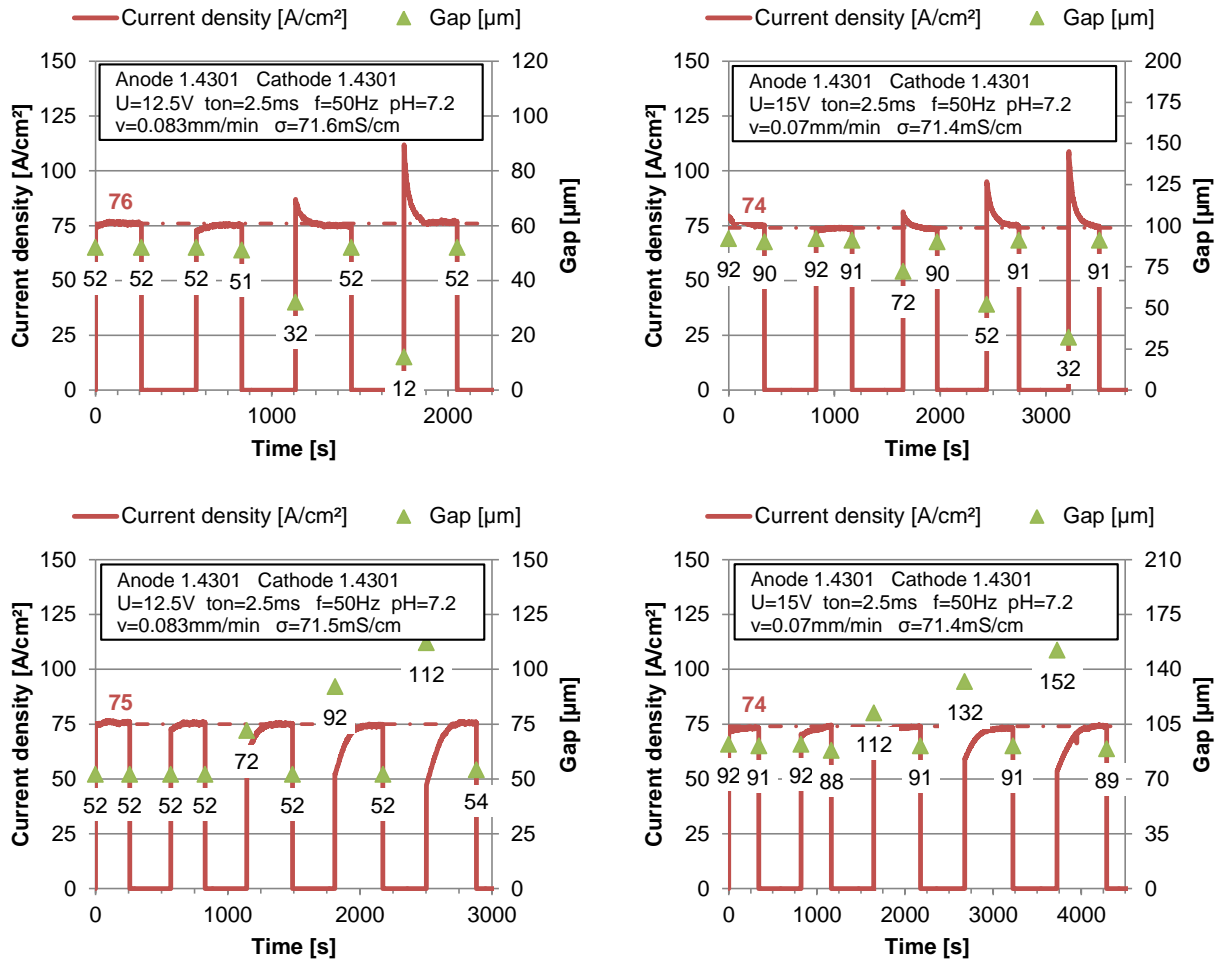


Figure 5-6 Development of equilibrium conditions at different starting gaps and two different voltages  $U = 12.5\text{V}$  (lhs) and  $U = 15\text{V}$  (rhs)

As the current density in the steady state or equilibrium gap condition is always constant when using the presented experimental setup, the current density in the following illustrations always refers to the steady state conditions.

Figure 5-7 represents a confirmation of the assumptions towards a self-adjusting equilibrium regarding current density, gap and feed rate, while proportionally changing the boundary conditions of the experiments. For example a doubling of the feed rate, while at the same time doubling the pulse on time, a similar current density is achieved following the laws of Faraday. The slight deviations in the actual current density can be explained by deviations in rise and fall times caused by the machine hardware and hence a resulting slight variation in the current density at each pulse. However, a closer look at three of the experiments presented in Figure 5-7, which

were already exemplarily pointed out in more detail in Figure 5-4, revealed just slight variations of less than 1 % in the charge transferred during each experimental run. Since the measured variable is the distance to be machined at a certain feed rate and voltage, the self-adjusting process mentioned before ultimately leads to a variation in current density in order to achieve the same result. This can only be achieved when the process is able to reach its equilibrium state during the provided time (here: total feed divided by feed rate). To take account of this statement, the overall feed in all presented experiments was compared to the stabilization of the current density during the process or preprocesses using the setup. Likewise the parameter sets were run to determine adequate boundary conditions in order to achieve reproducible and constant process conditions.

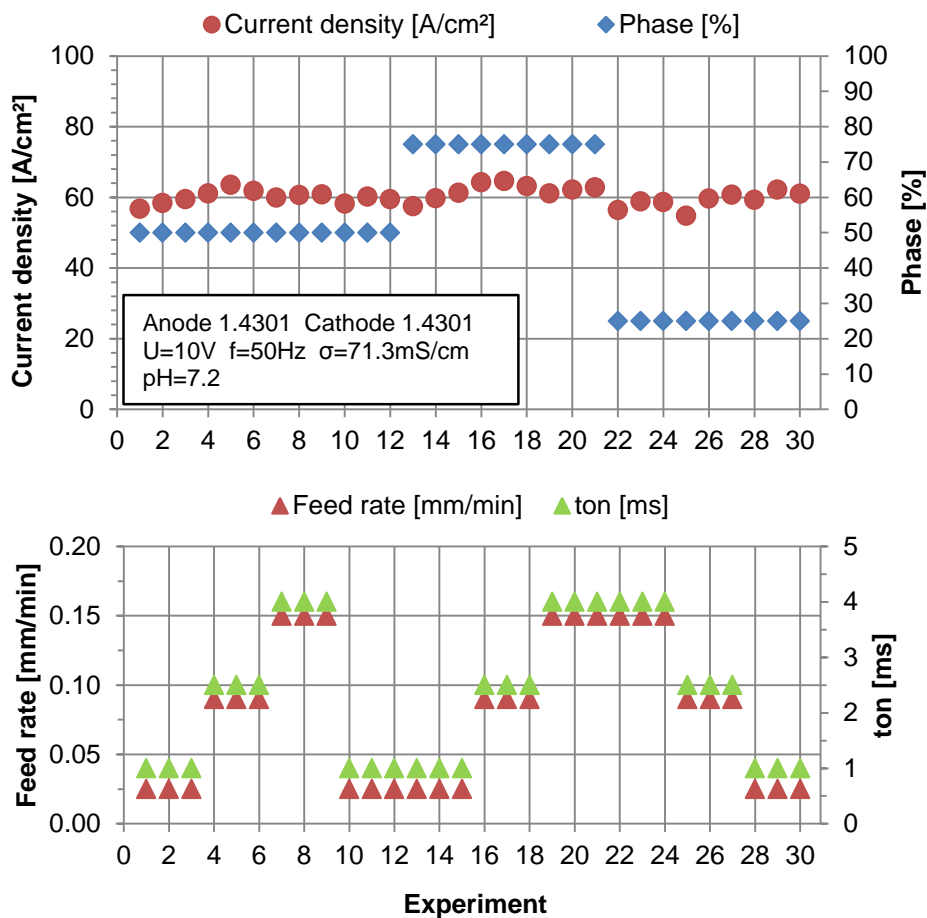


Figure 5-7 Stability of the current density (top) at repeated experiments under different experimental conditions (bottom)

As already indicated in Figure 5-7, the machine offers the possibility to adjust the current pulse in relation to the time the vibrator reaches the bottom dead center of its sinusoidal movement. The following experiments show the influence of this so-called **shift in phase** regarding the change in frontal gap measurement. The total deviation of the current density in the experiments presented in Figure 5-8 is below 1.5 %. Even though the current density was measured similarly in all experiments, there is a strong deviation in the gap measured. Therefore, the experiments are of special

importance towards the measurement and evaluation of the frontal gap during constant current density.

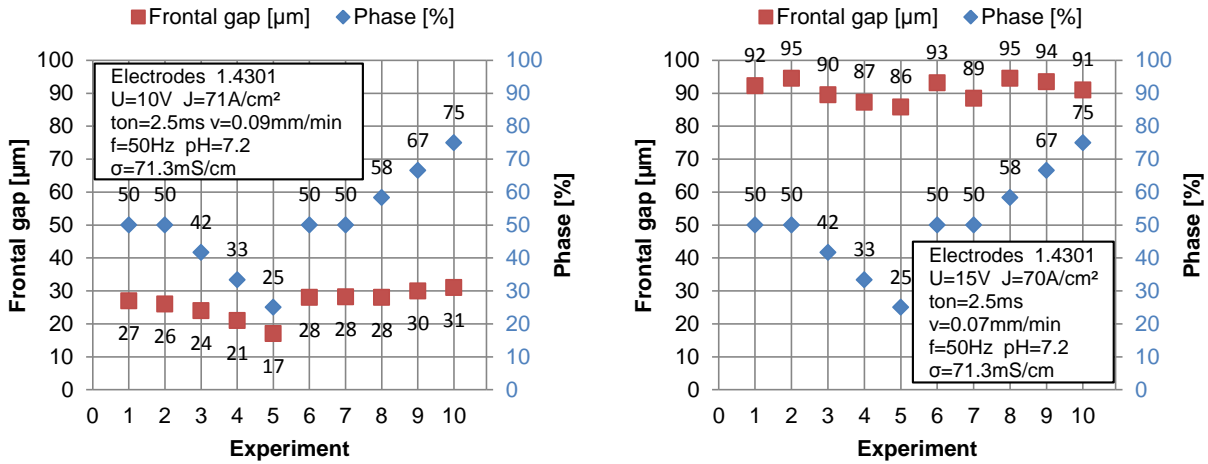


Figure 5-8 Influence of the shift of phase on the frontal gap at equal current density and U=10V (lhs) and U=15V (rhs)

From these first results, it appears that with the possibility to shift the pulse position (compare Equation 2-27) special attention needs to be paid to this setting in order to ensure comparability of the results. To explain this phenomenon a theoretical approach is required, since the gap measurement has a direct influence on the achievable geometric shaping accuracy. While a gap which was falsely measured too small can result in an unexplainable deviation in shaping accuracy, a gap falsely measured too wide when investigating the material behavior, can cause electrical shortcuts in applications, or unnecessary changes or adaptations in machining parameters.

The theoretical approach mentioned is based on Ohm’s law and takes into account the position of the mechanical vibrator over time. As indicated in Figure 5-9, the gap between cathode and anode changes during one oscillation and under a certain set of parameters. The ‘percentage deviation’ used is here defined as

$$\text{Percentage deviation [\%]} = \frac{\text{mean gap during pulse} - \text{equilibrium gap}}{\text{equilibrium gap}} \cdot 100\% \quad \text{Equation 5-1}$$

wherein the ‘mean gap during pulse’ is the averaged distance between anode and cathode during one complete pulse at a specified shift of phase.

The current signal is kept constant during the complete pulse independent of the shift in phase. This is achieved by adjusting the voltage pulse in accordance to the vibrator position over time. Yet, since the gap cannot be measured during each pulse in the available machine generation, the form of the voltage pulse needed is derived from the history of previous pulses and the respective current signal in correlation to the process constraints. The maximum voltage applicable is hereby limited by the electrical equipment. Looking at the results presented it becomes obvious how

important the setting of the shift in phase is in correlation to the frontal gap and ultimately the accuracy achievable in experiments.

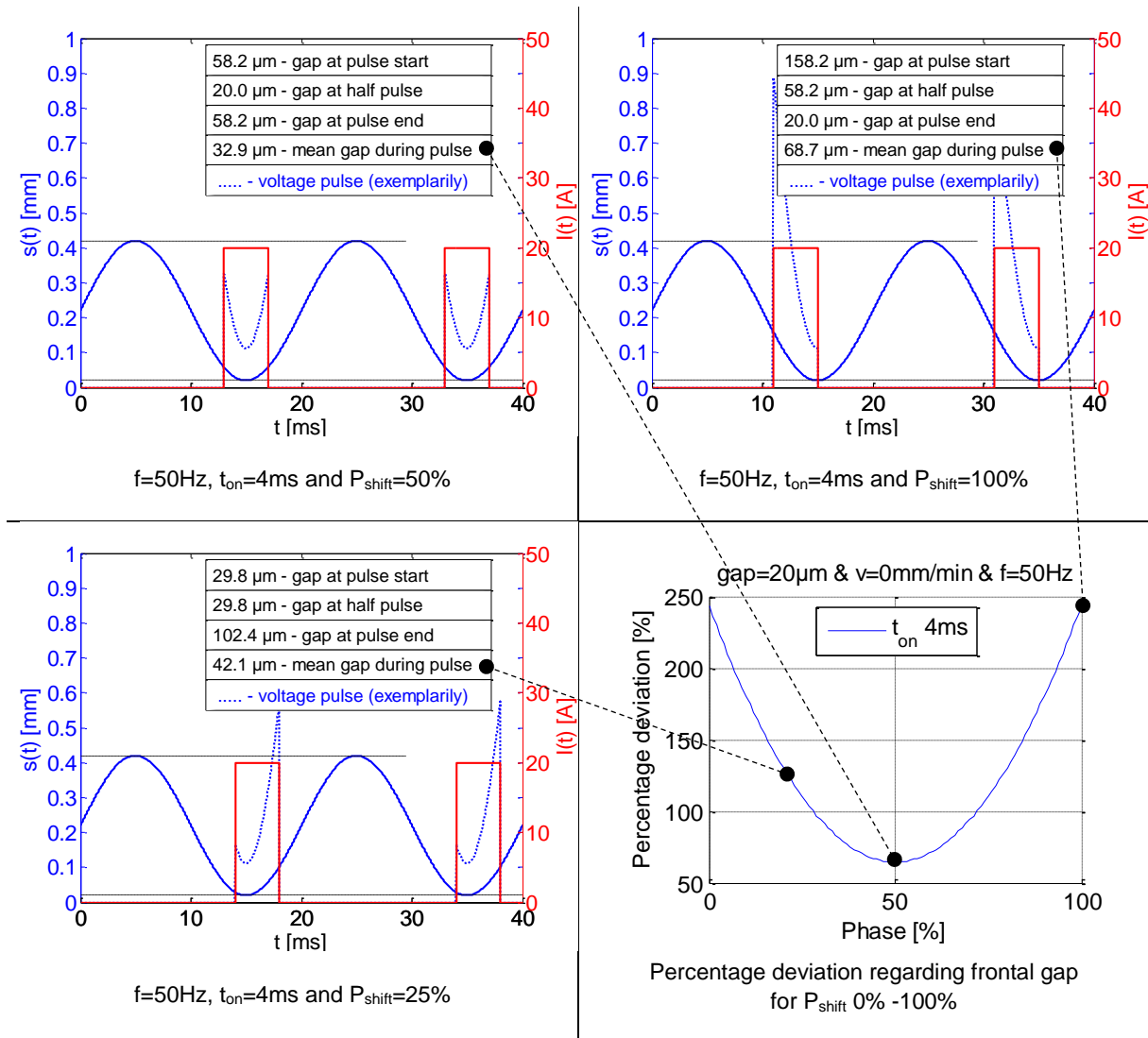


Figure 5-9 Percentage deviation of the frontal gap distance at different shifts of phase and equilibrium gap of 20  $\mu\text{m}$

In order to put the theoretical findings into context with the precision and repeatability of the process to identify material-specific models, Figure 5-10 and Figure 5-11 present the results of a shift in phase assuming the range of used parameters in this work. With a range of gaps measured between 10  $\mu\text{m}$  and 290  $\mu\text{m}$  in frontal gap experiments, the deviations in measurement caused using a shift in phase can range from -12 % to 130 % percent towards the actual process gap.

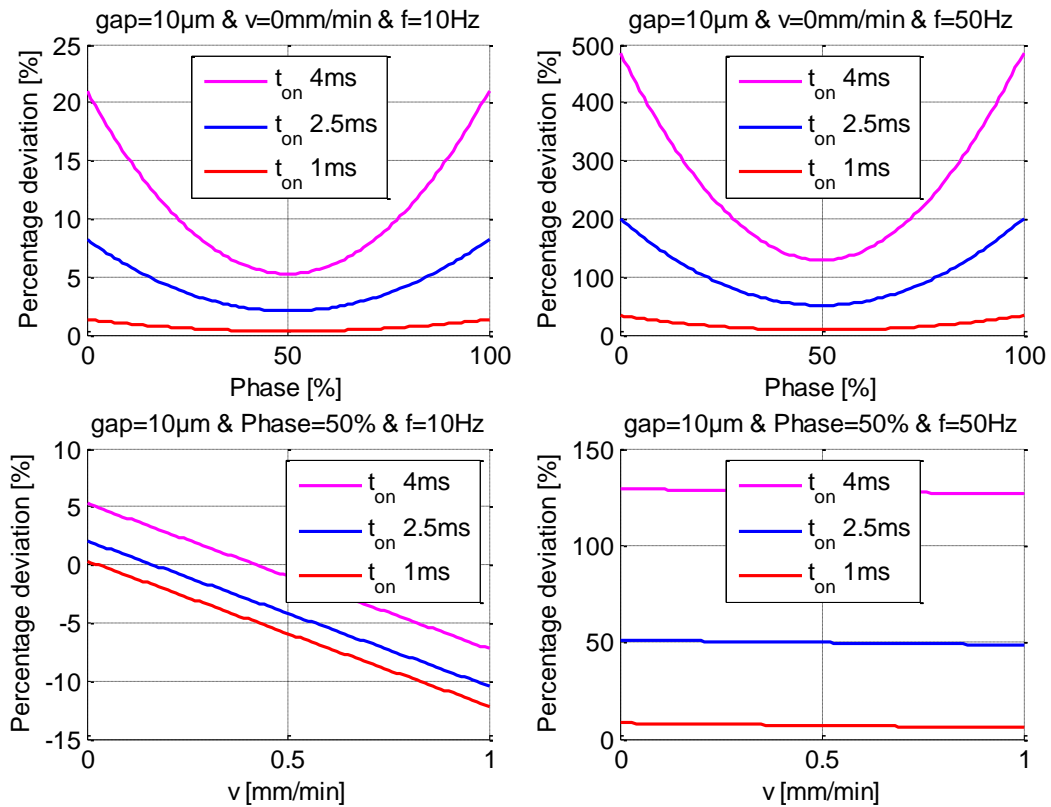


Figure 5-10 Deviations due to different feed rates or a shift in phase assuming a 10  $\mu\text{m}$  gap at the oscillations bottom dead center at 10 Hz (lhs) and 50 Hz (rhs)

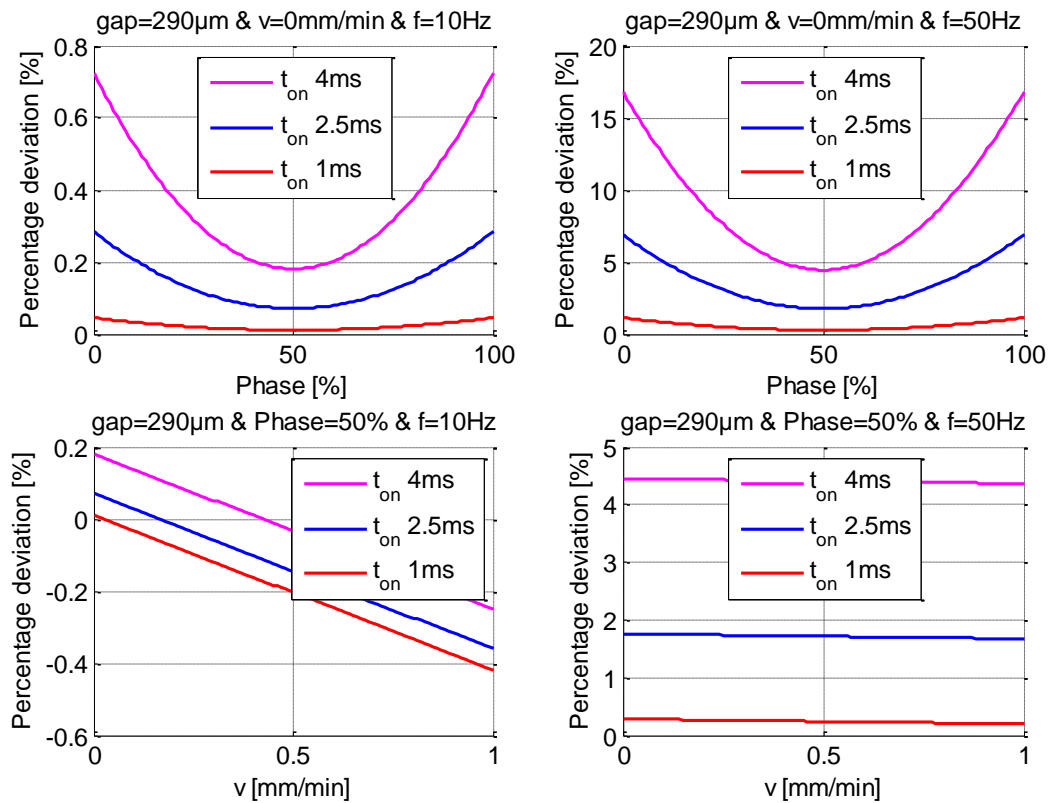


Figure 5-11 Deviations due to different feed rates or a shift in phase assuming a 290  $\mu\text{m}$  gap at the oscillations bottom dead center at 10 Hz (lhs) and 50 Hz (rhs)



Especially the oscillation **frequency** - mechanically and electrically coupled - set in the experiments has an effect on the gap measurement and the distance between anode and cathode during one current pulse. Figure 5-12 points out the effects at a 50% shift of phase and different oscillation frequencies. Smaller frequencies mean longer pulse off times between pulses, and increase the time for a passivation layer building on the anode surface. Once built, this layer has to be removed with a certain charge, which would not be necessary at a higher oscillation frequency and shorter passivation pauses. This effect is especially visible at small frequencies and high voltages (see Figure 5-12 at  $U = 15\text{ V}$  at  $f = 10\text{ Hz}$  and  $f = 20\text{ Hz}$ ). Here the gaps decrease, while the current density increases as a resulting compensation effect to break the passivation at lengthening pause times every time anew.

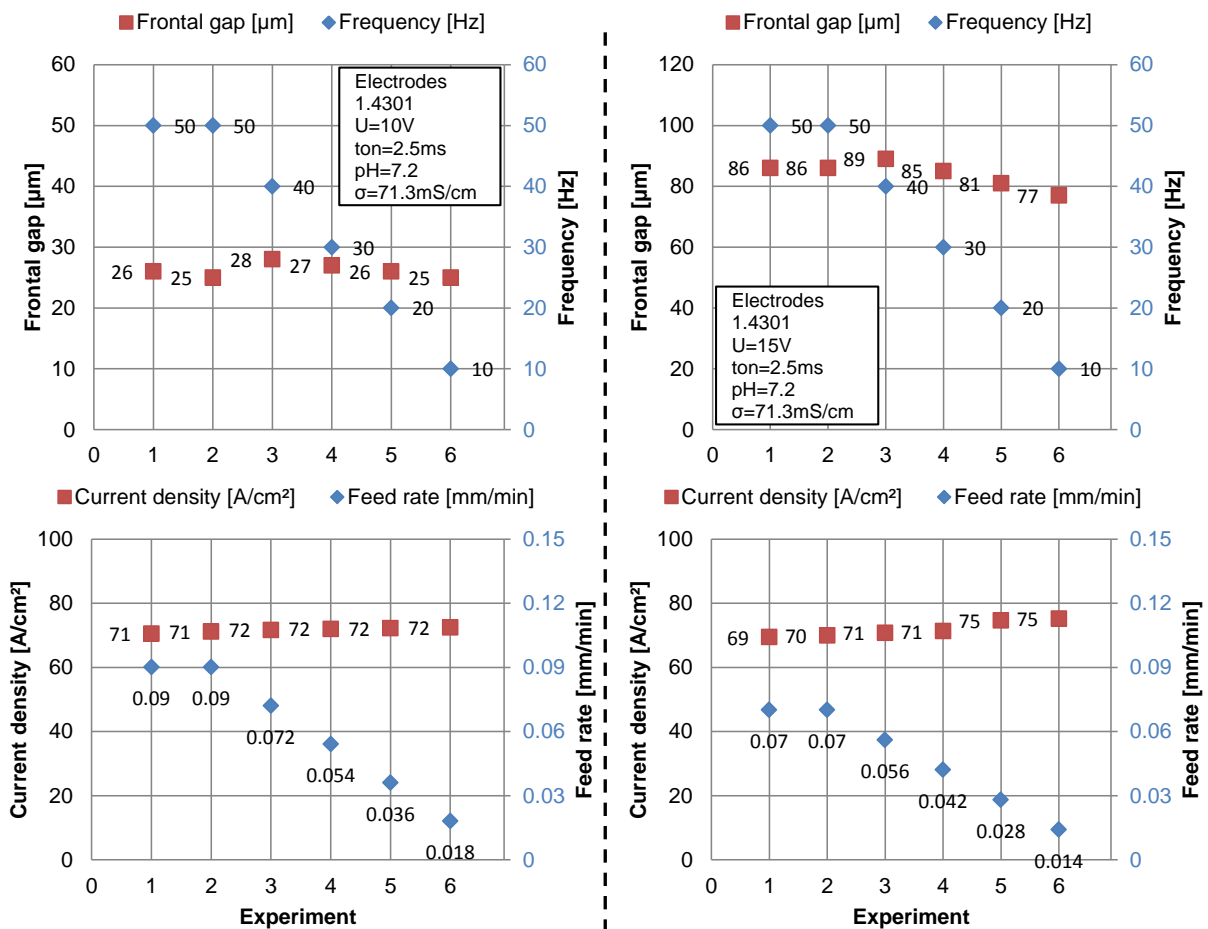


Figure 5-12 Influence of the frequency change on the frontal gap and current density at  $U=10\text{ V}$  (lhs) and  $15\text{ V}$  (rhs)

The effect of the **pressure** entering the constructed experimental setup is also of great interest. As pointed out in Figure 5-13, a change in pressure between  $100\text{ kPa}$  and  $800\text{ kPa}$  has significant effects on the gap and current density measured. Especially at small gaps ranging from  $10\text{ }\mu\text{m}$  to  $40\text{ }\mu\text{m}$ , the pressure leads to wide variations in the machine's integrated gap measurement, even though the experiments are all stable at a comparable current density.

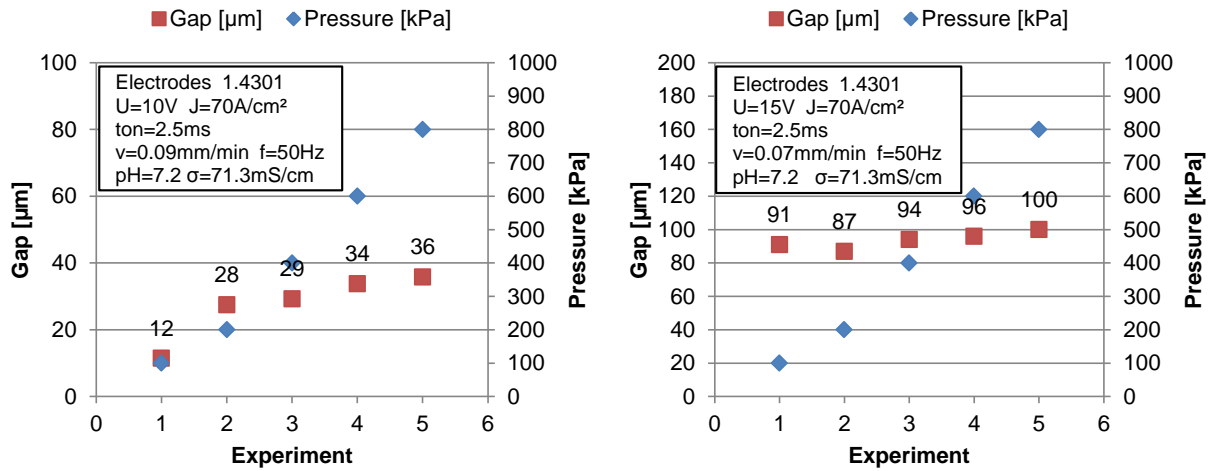


Figure 5-13 Effect on the frontal gap at different pressure and phase = 50 % and equal current density at U = 10V (lhs) and U = 15V (rhs)

In this section, the focus was on the selection of appropriate conditions for the reproducible recording of data relating to pre-processing, shift in phase, frequency and pressure in relation to the used machine technology. With all the considerations made, which prove the repeatability of the process at constant boundary conditions, the following conclusion can be made:

All experiments using this machining technology should be performed at a shift in phase of 50 %, a frequency of 50 Hz and at constant pressure (here  $p = 100$  kPa to assure the lowest possible flow velocity) to ensure comparable and reproducible results.

As explained before, it is hardly possible to specify a material by its current efficiency, since the valence values at different current densities are mostly unknown. Therefore the SMR or MRR value is used. SMR and MRR differ only in the density of their material, therefore SMR is considered as the variable of choice. Since there are at least two ways the SMR value can be experimentally determined, the calculation on the basis of weight and volume are compared and provided in the following.

Repeated measurements were performed and each of the SMR values determined on two different ways:

1. Measuring the difference in weight of the sample before and after machining and setting it in relation to the charge recorded during the experiment.
2. Putting the feed in relation with the dimensions and therefore the volume of the material machined, and the current density at equilibrium conditions.

The experiments presented in Figure 5-14 show the two possible ways to determine the SMR value. In both cases the same experiment is evaluated using Faraday's law in combination with the loss-of-mass measurement. The other SMR result describes the SMR value determined from the cylindrical sample volume machined, using a specific feed rate and the charge recorded. The experiments show that the deviations

between the two approaches is well below 5 % in the stable field of parameters defined before. The way of calculating the SMR using the volume is an advantage, since the sample neither needs to be weighed, nor changed or replaced after each experiment. In this way the time needed for the experiments can be reduced.

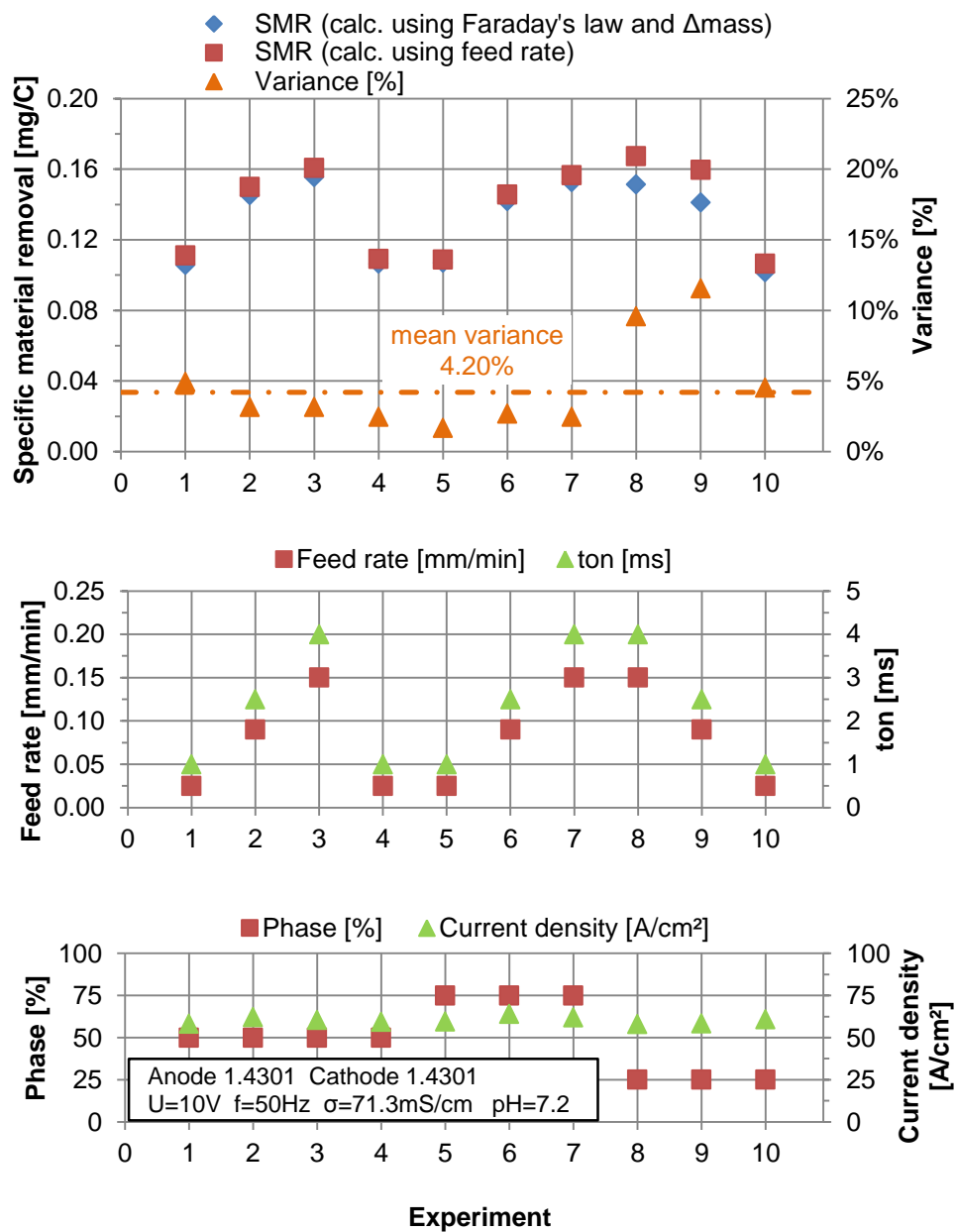


Figure 5-14 Calculation of the SMR value at different parameter settings

## 5.2 Side gap experiments

According to the findings and results from the frontal gap experiments the side gap evolution will be considered in more detail. In contrast to the frontal gap experiments a variation in processing is needed to determine the geometric behavior taking place in the side gap. Since the vibration of the tool electrode is perpendicular to its feed rate, it is simple to reproduce these conditions. By applying the vibration and setting the feed rate to zero, the frontal gap widens at each pulse. Even though it would be possible to just apply electrical pulses and hereby switching off the vibration, the effects resulting from a gap widening in the pulse pause time should not be neglected. The corresponding schematic is presented in Figure 5-15.

An exemplary result of the side gap measurements is presented in Figure 5-16. The supporting points are chosen at fixed times: 0.5 s, 1 s, 2 s, 4 s, 8 s, 16 s, 32 s, 64 s, 128 s, 256 s, 512 s, 1,024 s and 2,048 s. At each point the gap is measured and the value recorded, afterwards the experiment is started once again from the beginning.

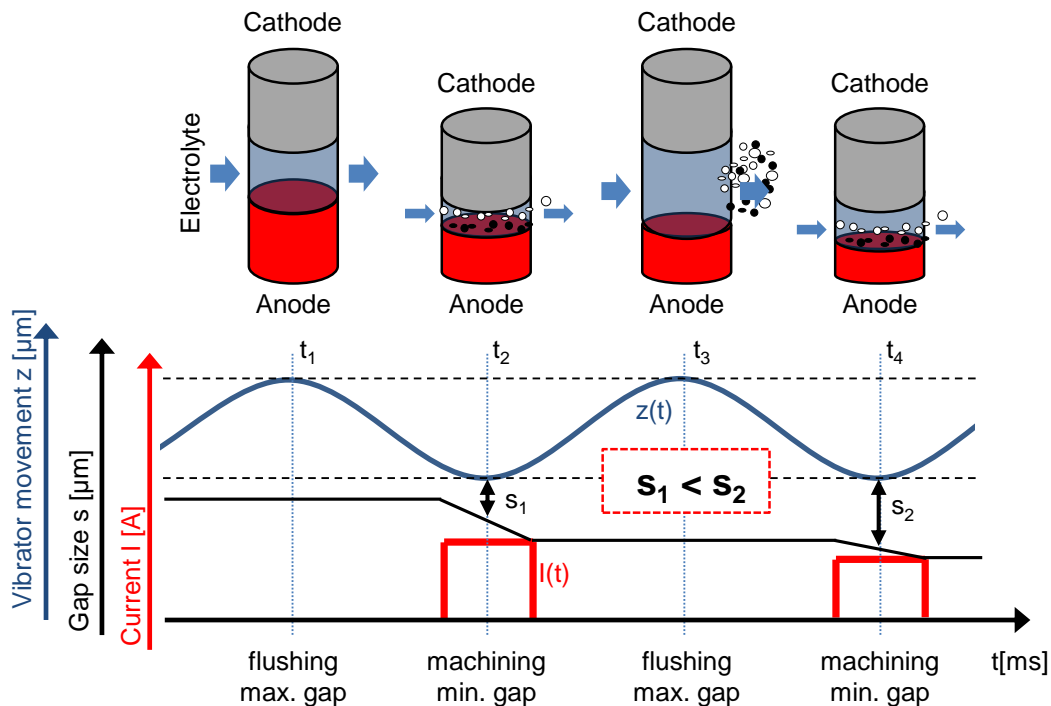


Figure 5-15 Course of processing in side gap experiments

Although there is a slight increase in the rounding of the circumferential edges of the anode in this type of experiment, it was found after removing the samples that the frontal surface remains parallel to the cathode surface. The hereby continued predominant homogeneity of the electrical field in the gap is thus a measurable indicator of the gap widening over time.

$$y = \sqrt{2 \cdot C \cdot t + y_0^2}$$

Equation 5-2

Using the theoretical approach for the gap widening [11, 22, 29] displayed in Equation 5-2, the hereby obtained result is overlaid using the parameters  $C = 10.33$  and  $y_0 = 20 \mu\text{m}$  as initial starting gap used in the experiments in Figure 5-16. The value  $C$  was hereby obtained by fitting the experimental data towards the theoretical solution using the software Matlab.

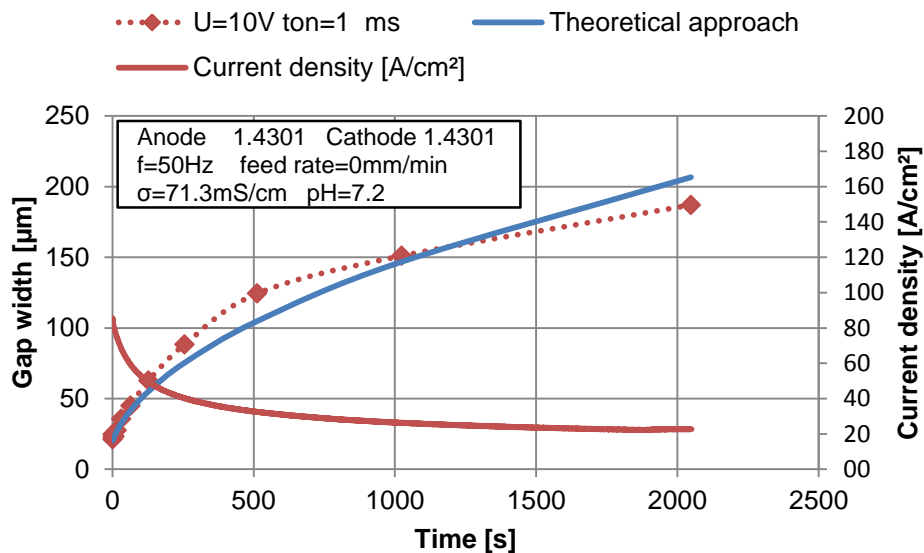


Figure 5-16 Theoretical and practical side gap evolution

### 5.3 Continuous observations

The presented experimental setups to investigate effects and relationships in frontal and side gaps focus on the equilibrium state processes conditions and result in the evaluation of mostly single data points. Yet, none of these experimental setups allow the observation of complex shaping. In order to observe the electrochemical shaping in PECM a device was developed, built and tested which allows a visual observation during the complete process. Results and background information on this setup were presented in [87] and further details in [88].

Already in 1974 the effects of the electrolyte flow velocity and cathode orientation on gas [28] and later in 1982 [89] the flow characteristics in PECM were investigated under the assumption of stationary conditions. Also profound in-situ observations of copper (Cu) were conducted using a custom setup with an integrated microscope [90, 91, 92, 93]. Yet, next to the setup reported herein and the works published later focusing on simulation in ECM [94], no in-process recording could be found in literature. The schematic setup developed is pictured with regard to the main components in Figure 5-17 and the flushing chamber including the connection possibilities in detail in Figure 5-18.

In Figure 5-17 a cathode and anode setup is displayed, which allows different possibilities of flushing. The most common is flushing through the anode (either anode to cathode or the other way around) or flushing from one side to the other, combinations are optional. The high-speed-camera type Olympus i-Speed TR, by company Olympus, and the LED light sources are orientated towards the process window. This process window, in terms of imaging, or process chamber in case of PECM is housed on either side of the electrodes using two PMMA plates. The electrodes themselves are fitted to metal clamping devices, which are connected to the machine's power supply. Figure 5-18 presents a more detailed schematic of the composite setup. The numbers indicate the possibilities for inflow and outflow connections of the electrolyte. Using this setup, multiple flushing conditions are possible in interaction with the use of the appropriate anode and cathode geometries. However, in the course of this thesis only experimental results derived from the example of flushing through the anode towards a cathode surface (combination: 4 → 1 & 3) and flushing from side to side (combination: 1 → 3) are presented.

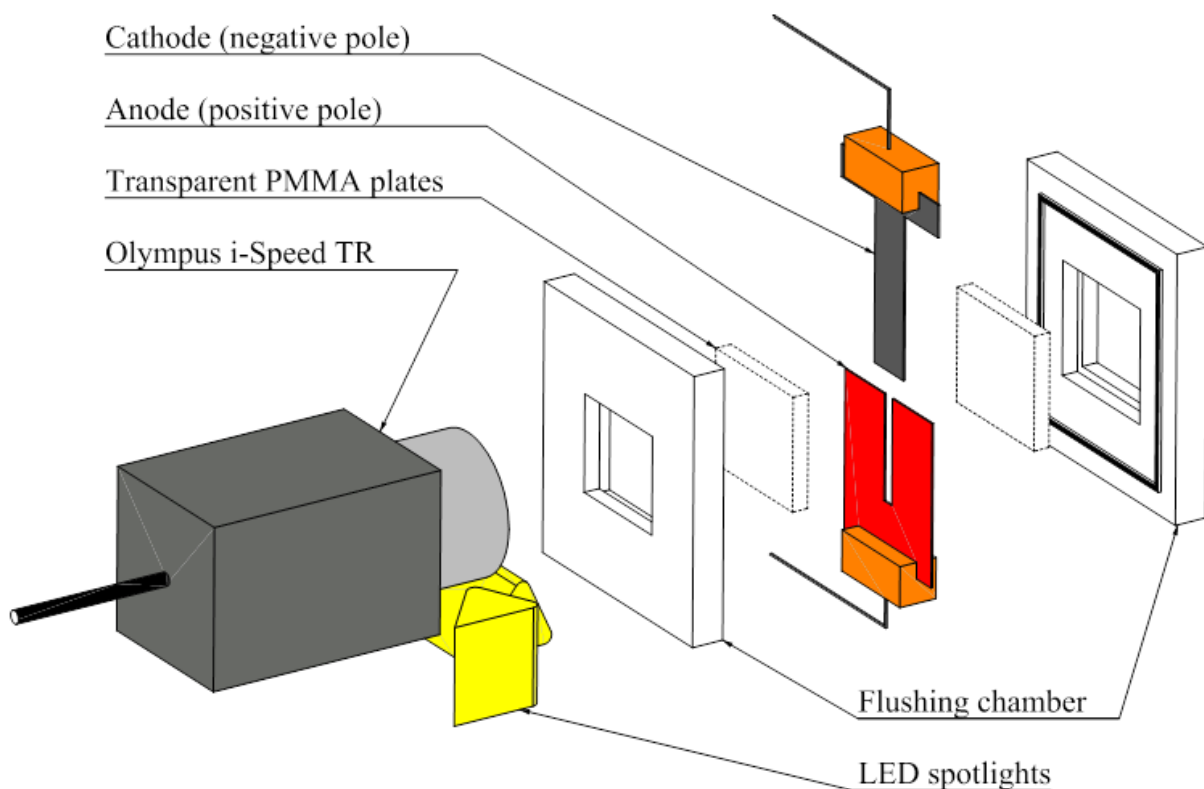


Figure 5-17 Experimental setup for continuous observations

The electrodes used in the experiments consist of precision sheet metal (material 1.4301) with a thickness of 1 mm. The frame rate in all experiments was chosen to 2 fps (at a shutter time of 150  $\mu$ s) to enable a complete recording of the PECM process over a time interval of over 152 min using the best available resolution. The recording can be extended by reducing the resolution or using a lower framerate as specified in the camera data and specifications listed in APPENDIX A.

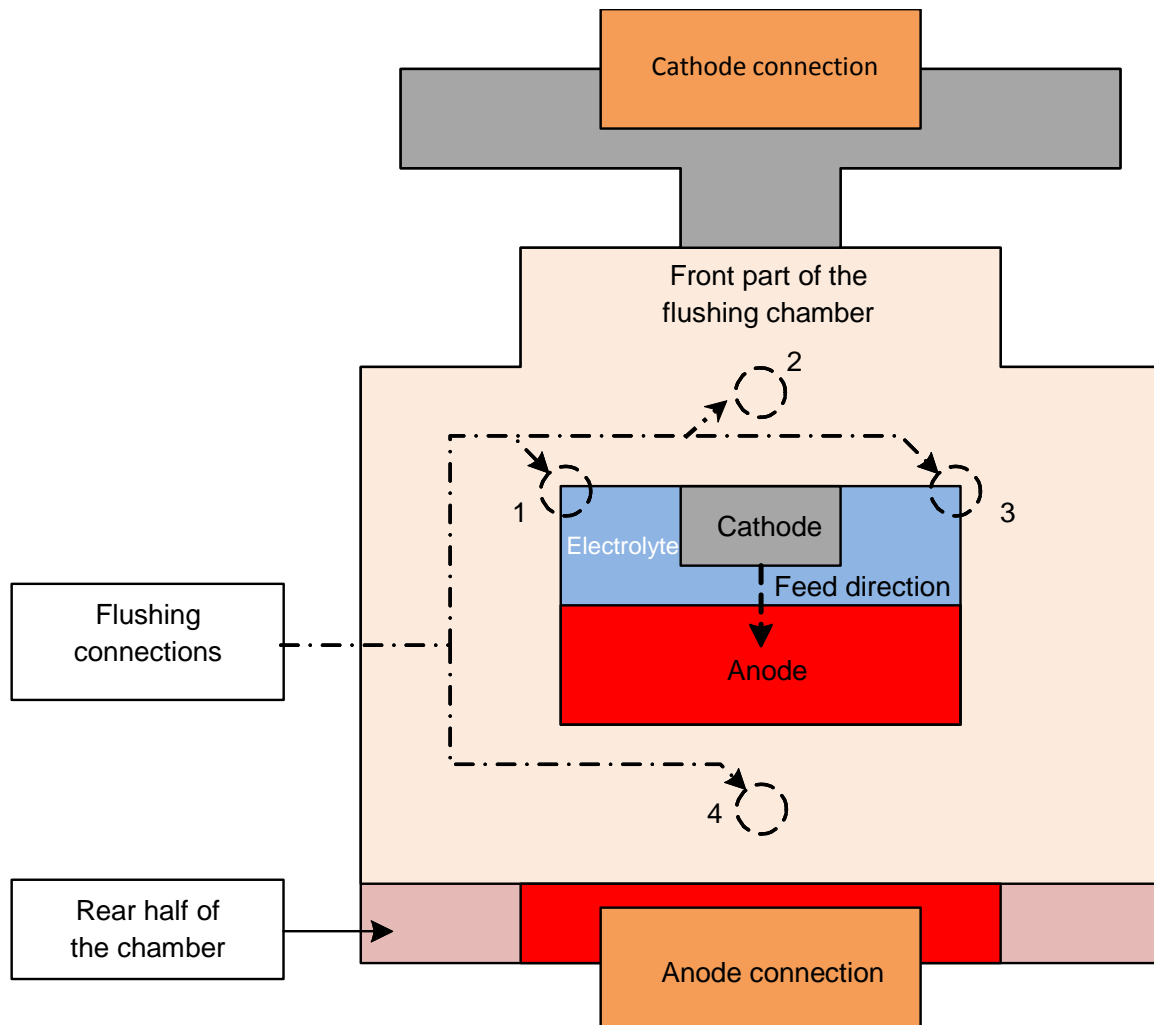


Figure 5-18 Setup flushing chamber

The flushing chamber itself is made of additive manufacturing technology (EOS Formiga P110, Material: PA2200 infiltrated), which was tested for the use under PECM processing conditions [95]. The chamber is mainly used to achieve a pressure difference between the inflow and outflow of the electrolyte [70]. This concept of differential pressure reduces the appearances of flow-induced grooves [96, 97] and allows more constant and reproducible process conditions as well as in some cases higher feed rates [23] since the gas phase during the pulse gets minimized by compressing the gas mechanically [58] – compare schematic in Figure 5-19.

Figure 5-20 pictures the setup when integrated in the PECM machine and the Controller Display Unit (CDU) image shows the actual interelectrode gap before processing.

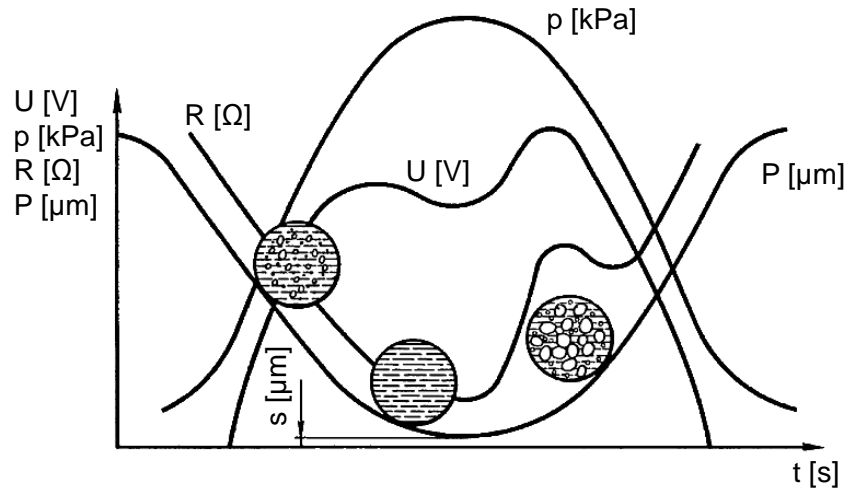


Figure 5-19 Voltage (U), Pressure (P), Resistance (R) and Position (P) relationship in PECM over time, similar [58, 71]

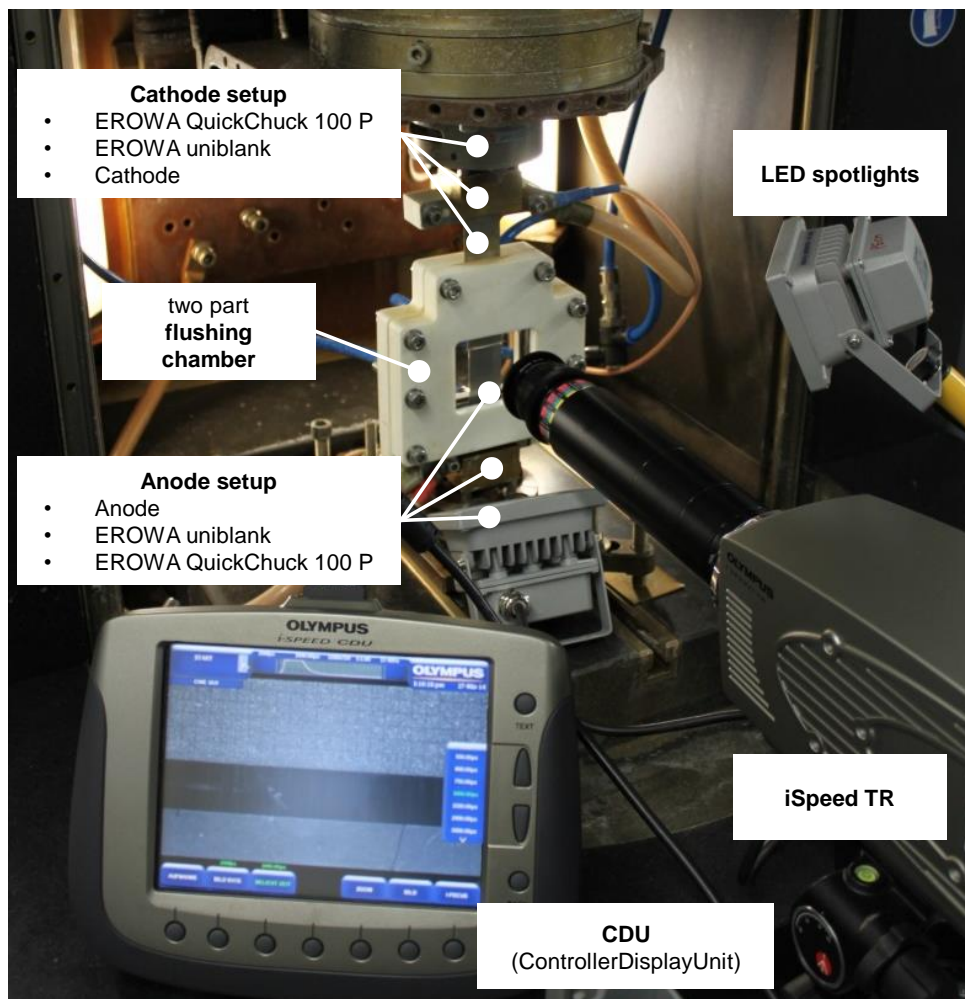


Figure 5-20 Setup integrated in PEMCenter8000 (Setup: Inlet 1 - Outlet 3)

Since the camera position can change during experiments on different days and in order to assure and provide a size reference in all experiments a cross sectional structure of 500  $\mu\text{m}$  times 500  $\mu\text{m}$ , see Figure 5-21, was added on each cathode



using a 3D-Micromac/Lumera 355 nm picosecond laser located at the research group 'Sensorik und Dünnschichttechnik' at the University of Applied Sciences (German: Hochschule für Technik und Wirtschaft des Saarlandes), Germany.

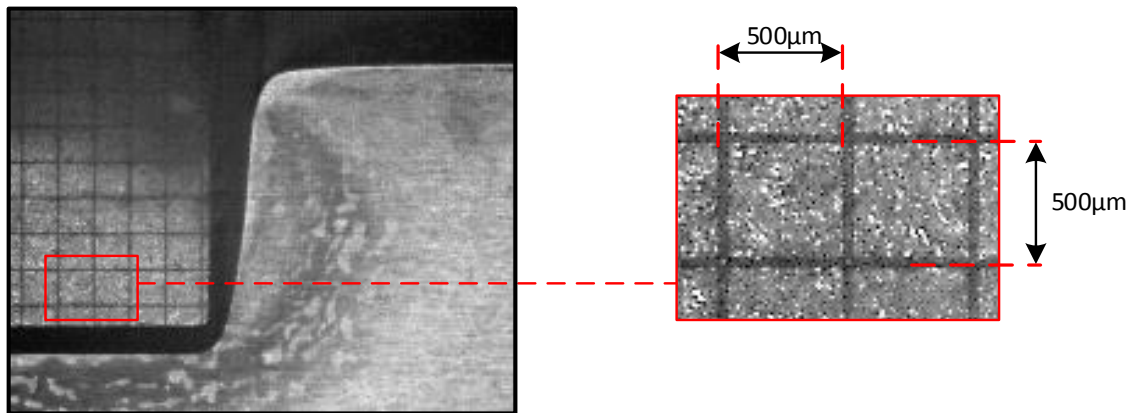


Figure 5-21 Reference structure on each cathode

The results in Table 5.2 are based on measurements using the high-speed camera by recording a microscope calibration slide. The measurement is done using the camera-integrated measuring tool. Details about the used microscope calibration slide and more detailed results from the optical evaluation are attached in APPENDIX B. As Table 5.2 shows, the conversion factor from pixel to distance is on average 8.5 µm per pixel, with a pixel having a rectangular shape.

Table 5.2 Optical resolution based on image acquisition using a microscope calibration slide

Size of the reference structure	Optical evaluation results			
	mm	pixel		µm/pixel
1.5	179	→	0.00838	8.38
0.6	73	→	0.00822	8.22
0.15	17	→	0.00882	8.82
0.07	8	→	0.00875	8.75
0.1	12	→	0.00833	8.33
			<b>Average</b>	<b>8.50</b>

Because the images are taken during the mechanical sinusoidal movement, the anode and cathode surface move while the shutter is active and the image is stored in the camera's memory. Figure 5-22 shows the theoretical minimum and maximum blur occurring during a 50 Hz frequency and a constant shutter time of  $t_{\text{shutter}} = 150 \mu\text{s}$ . Around the top and bottom dead center of the movement, the speed reaches zero (yellow line) and the blur is at its minimum. At the maximum speed indicated (green line), the blur is calculated to 9.4 µm. This of course just applies to the cathode movement. The anode moves only during the pulses at a velocity, which

is slightly higher than the feed rate in the considered time interval. For example, at a constant feed rate of  $v = 0.2 \text{ mm/min}$ , which corresponds to  $3.33 \text{ } \mu\text{m/s}$ , the blur corresponds to  $0.0666 \text{ } \mu\text{m}/t_{\text{on}} * t_{\text{shutter}}$  at  $f = 50\text{Hz}$ , which is more than factor 127 smaller than the average measured optical resolution.

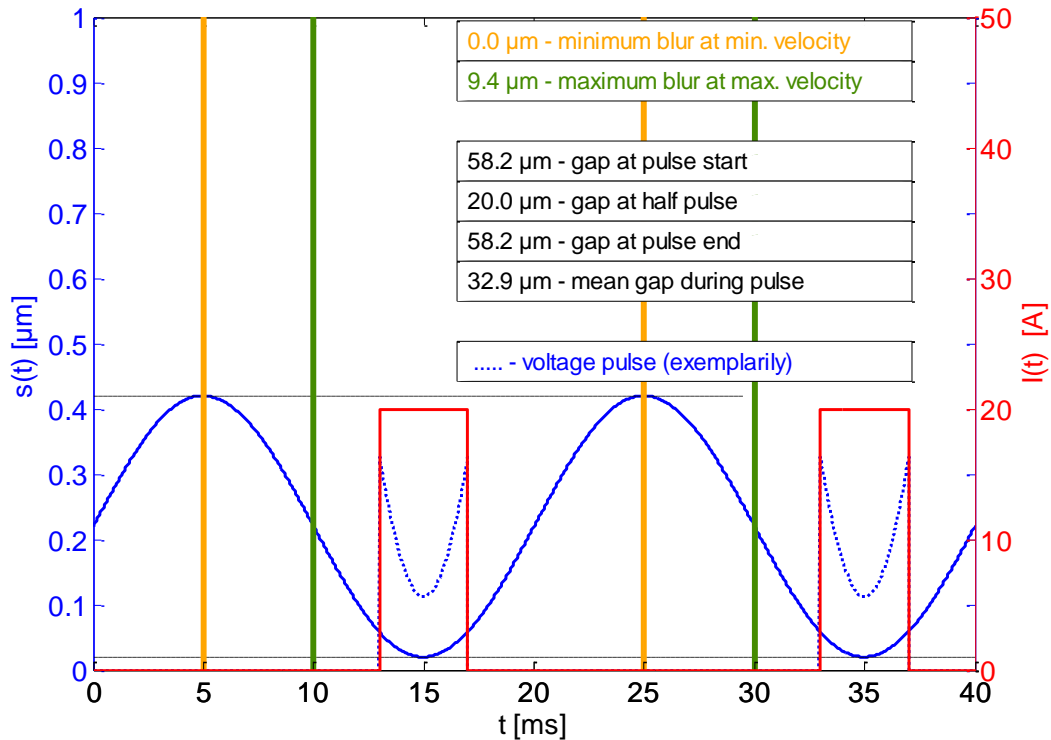


Figure 5-22 Schematic of the minimum and maximum image blur resulting from the mechanical oscillation at  $f=50\text{Hz}$  and a shutter time of  $150\mu\text{s}$

An example of a recording using a specified geometry and a recording of 120 min is presented in Figure 5-23. Here the materials were both precision sheet metal of type 1.4301 with a thickness of 1 mm and the dimensions provided in the schematic. The resulting pictures are displayed at time intervals of 900 s. The machining depth corresponds to 3.2 mm, neglecting the starting gap, using a flushing through the anode towards the cathode. The figure shows the individual pictures and the corresponding results using a programmed edge detection algorithm (software Matlab) to trace the outlines of the anode at each specified time interval. The experiments and parts of the Matlab programming were carried out as part of two master theses supervised by the author at the Institute of Production Engineering at Saarland University [98, 99].

Parameter	Total feed [mm]	Feed rate v [mm/min]	Pressure p [kPa]	Voltage U [V]	$f_{\text{mechanical}}$ [Hz]	$f_{\text{electric}}$ [Hz]	$P_{\text{shift}}$ [%]	$t_{\text{on}}$ [ms]	Initial gap [ $\mu\text{m}$ ]
Moving cathode	3.3	0.027	100	10	50	50	75	2.5	110

Flushing direction from the bottom through the channel in the cathode towards the anode

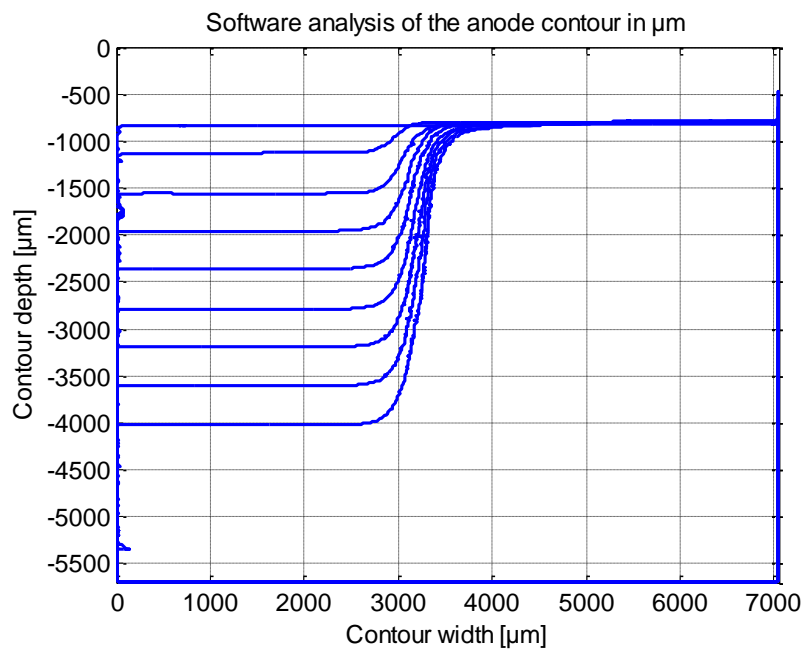
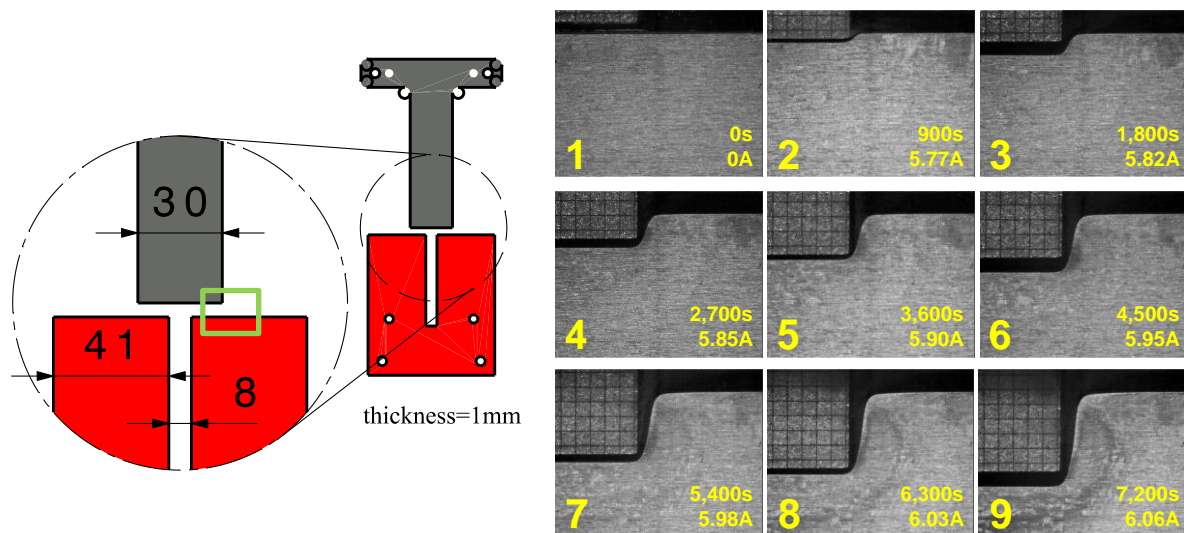


Figure 5-23 Results of a nonstop 120 min PECM experiment divided into 900 s intervals

## 5.4 Electrical and Surface Measurements

Two different approaches for the data acquisition were conducted during the experiments. On the one hand all available data was collected by machine integrated sensors at a sample frequency of about 4 Hz, and on the other hand additional hardware and software were installed. To detect and save data, a data acquisition system was purchased, which allows a sampling frequency of 250 MS/s (MS/s = Mega Samples per second). All additional measurement equipment, on top of the machine-integrated sensors and the specifications are listed in Table 5.3. All sensors used in the experiments were evaluated and chosen on the basis of investigations concerning the use in the PECM environment [100]. Special focus lies on range, accuracy, reaction time and especially the durability during electrolyte contact. Limiting conditions like material in medium contact consisting either of chemical resistant plastic or stainless steel were also taken into account, as well as the ability to withstand mechanical vibrations up to 60 Hz with an amplitude of 200  $\mu\text{m}$  in combination with high currents and therefore possible induction and (sensor) noise. Other values, e.g. osmotic water or compressed air supply as well as NaOH and HNO<sub>3</sub> volumes dosed during experiments to automatically regulate the pH value, were not considered.

Table 5.3 External, electric measuring equipment

Type	Sensor Measurement principle	Range Signal / Unit	Peak di/dt [kA/ $\mu\text{s}$ ]	Accuracy	Rise time	Company
Rogowski current transformer	CWT3LFB/4/1000 Rogowski Current Transformer	0 – 0.6 kA	4.0	$\pm 1 \%$	direct electrical response (<< 1 ms)	PEM - Power Electronic Measurements Ltd., Nottingham, U.K.
Rogowski current transformer	CWT60LFB/4/1000 Rogowski Current Transformer	0 – 12 kA	11.0	$\pm 1 \%$	direct electrical response (<< 1 ms)	
Current transformer	HTA 100-S	$\pm 300 \text{ A}$ (100 A nominal)	> 0.05	$\pm 1 \%$	< 3 $\mu\text{s}$	LEM Holding SA, Fribourg, Switzerland
Current transformer	HTA 300-S	$\pm 900 \text{ A}$ (300 A nominal)	> 0.05	$\pm 1 \%$	< 3 $\mu\text{s}$	LEM Holding SA, Fribourg, Switzerland
Voltmeter	HZ109 Differential Probe	$\pm 35 \text{ V}$	-	$\pm 3 \%$	17 / 12 ns	HAMEG Instruments GmbH, Mainhausen, Germany
Type	Name	Maximum sampling rate	DC accuracy	Interval accuracy (DC ~ 100MHz)	A/D converter	Company
Data Acquisition	Peaktech 1280	250.00 MS/s Dual channel	$\pm 3 \%$	$\pm (1 \text{ interval time} + 100 \text{ ppm} \times \text{reading} + 0.6 \text{ ns})$	8 bits	PeakTech Prüf- und Messtechnik GmbH, Ahrensburg, Germany

In the low current ranges the measurements revealed a strong deviation in the current recorded by the machine itself and the actual current in the process recorded

using the external sensors. Since the deviation was linear in the range between 7 A to 70 A a function could be calculated to adjust the results provided from the machine. Also for the range of 70 A and above a constant deviation in the current recorded for the machine used was determined. Both functions are presented in Figure 5-24.

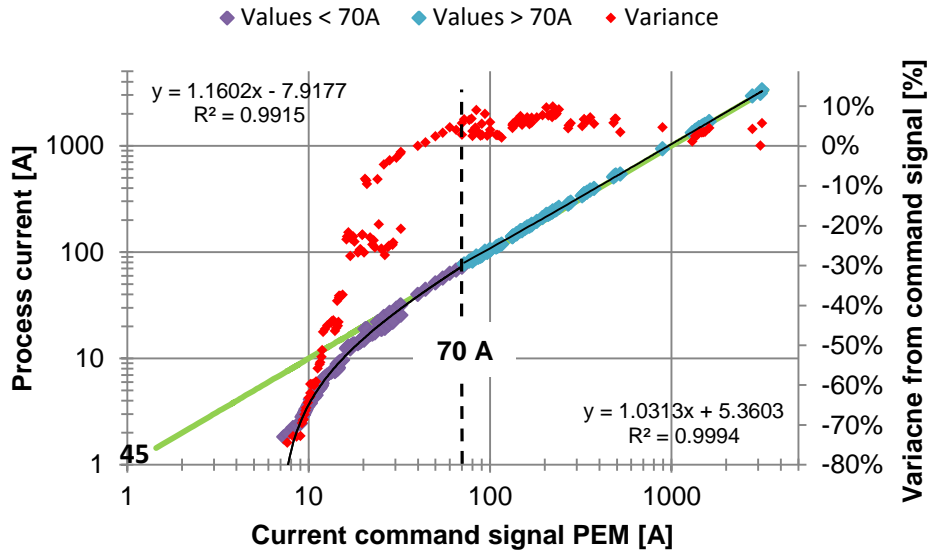


Figure 5-24 Data correction based on external measurement

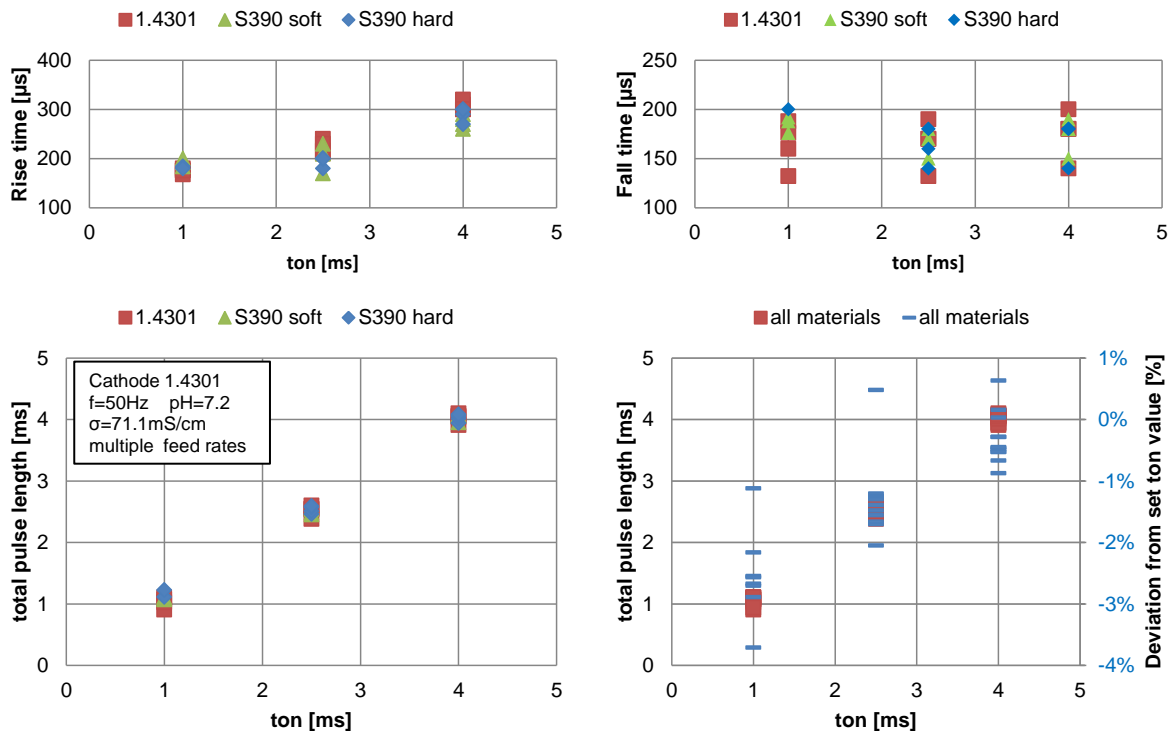


Figure 5-25 Rise and fall times at different pulse on times

On the basis of the conducted measurements using the external sensors, see Figure 5-25, it was determined that the pulse length in experiments with constant pulse

times of  $t_{on} = 1$  ms have to be adjusted by 2.65 %,  $t_{on} = 2.5$  ms by 1.45 % and with  $t_{on} = 4$ ms by 0.35 %. The corresponding corrections to the times and effects on SMR and MRR values in Coulomb are included in all presented experimental data.

Next to the electrical data, the surface roughness is also of special importance. With a surface roughness reported in the range of  $R_a=0.05-12.5\mu\text{m}$  using ECM and  $R_a = 0.002-3.2 \mu\text{m}$  using electropolishing [3], the achievable surface roughness is an important and special feature as well as an indicator for the use of ECM. To achieve such a fine surface roughness, the fundamental aspects of electropolishing and surface brightening under ECM conditions [101] were already investigated. It has been found that macrosmoothing on the surface results from local differences on a rough surface of the gradient of either the potential or of the concentration of the transport limiting species [102]. In this context the electrolyte concentration, pH and temperature play a role in the brightening of the surface [101]. However, since these constraints remain mostly constant in this thesis, the influences will not be regarded. On the other hand the initial surface roughness of the tool plays an important role [57] and has a significant influence on the smoothing process, with the anode surface roughness being usually smaller than the surface roughness of the cathode used [103]. In order to observe and measure the effects caused by PECM on the material surface in accordance to DIN4760 [104], the surfaces are measured following the standards specified in EN ISO 4287 [105] and EN ISO 4288 [106] - using a Mahr MarSurf XR/XT 20 profilometer in accordance to VDI/VDE2602 [107] which is located at the Institute of Production Engineering at Saarland University. The commonly used values  $R_a$ ,  $R_z$  and  $R_{max}$  are used to describe the surface roughness achieved in the experiments.

## 6 Simulation Concept

The amount of material removed following Faraday's law is dependent on the exposure time and intensity of the electric current. Therefore it is important to understand how the electric current is distributed over the electrode surface. Especially the strength of the electric field and resulting from Ohm's law, the related current density is distance and therefore highly geometry-dependent. Accordingly, this chapter gives an insight into the electrostatic field simulation and the calculation of the electrochemical dissolution on the basis of the ratio between gap distance and current density. Furthermore two approaches towards the use of material-specific data for the simulation of anodic shaping and inverse tool calculation are presented.

### 6.1 Static simulation

To understand and correctly consider the current in the experimental devices, FEM is used to simulate the static electric fields. The necessary calculations and considerations are done using the software COMSOL Multiphysics (Version 4.2a) at ZeMA. The results and impact of the field simulated as well as data on the current density can be related to the recorded machine data, and conclusions can be drawn towards effects and necessary corrections.

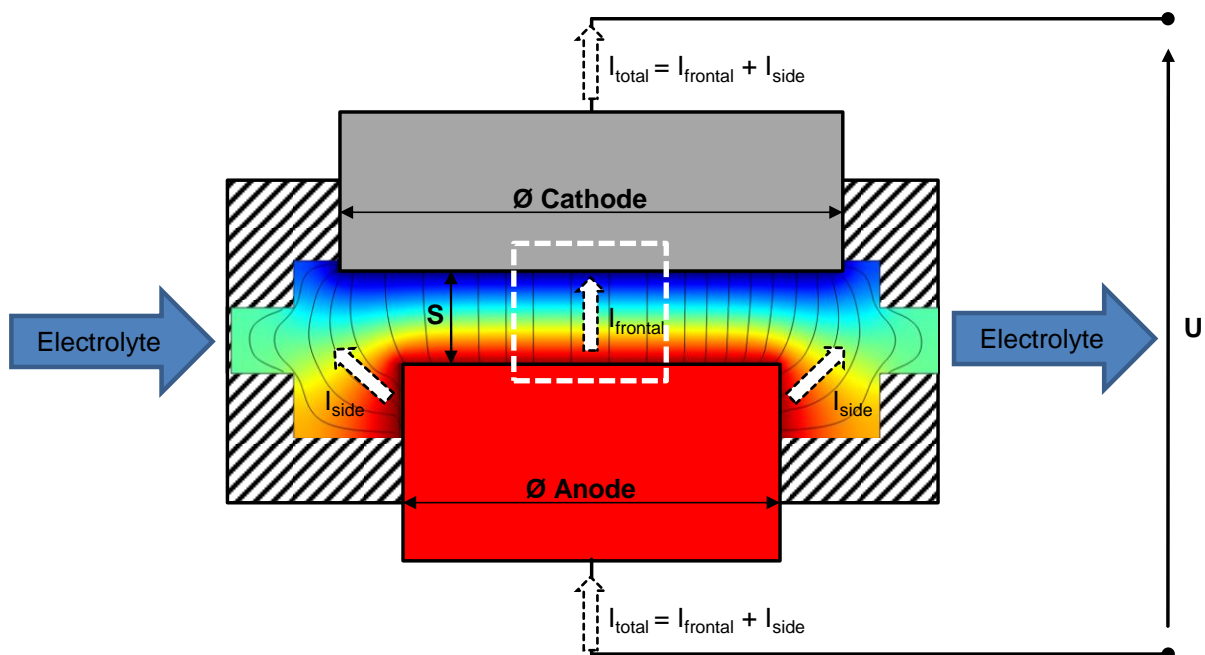


Figure 6-1 Schematic result of a FEM simulation picturing the electric potential (colors) and the lines indicating the homogeneity of the current density in the experimental setup

Figure 6-1 shows the aim of the static simulation. While the electric potential is distributed over the complete surface in touch with the electrolyte and is inhomogeneous towards the edges of the anode and cathode, the current density is highly homogeneous close to the center of the setup (highlighted area). Hence, the current density and electric field represent the electric conditions during the

machining when using a constant feed. By setting the simulation model underlying the experimental data, the total current recorded can be separated into a frontal gap and side gap share. Using this approach, the dependence between feed rate and current density in the frontal gap can be calculated. The effects resulting from flushing and joule heating were neglected in these simulations, since no data was recorded to verify the related results. Table 6.1 lists the material parameters used in the simulation. The input parameters regarding the current, voltage and conductivity were individually considered in relation to the experiments.

Table 6.1 Electrical data on the materials taken from their individual data sheets

Material	Electrical resistivity [ $\Omega \cdot \text{mm}^2/\text{m}$ ]	Electrical conductivity	
		[ $\text{S} \cdot \text{m}/\text{mm}^2$ ]	[ $\text{mS} \cdot \text{cm}/\text{cm}^2$ ]
1.4301	0.72	1.39	13,888,888.9
S390	0.61	1.64	16,393,442.6

Since the simulation was not adapted to consider effects on the electrode surfaces, the polarization can be inversely calculated in the frontal gap. By using the recorded experimental current as input to the simulation, for the following two geometries listed, the resulting voltage at the electrodes can be calculated assuming Ohm's law.

1. Cathode diameter 8 mm and anode diameter 6 mm in case of 1.4301
2. Cathode diameter 6.3 mm and anode diameter 6.3 mm in case of S390

As a result of this simulation the calculated voltage can be subtracted from the actual voltage used in the experiments, compare Equation 2-22, and as a result the total polarization voltage for this setup under experimental conditions and boundary conditions can be acquired. For the simple example of a uniform frontal gap at given gap distance, the formula can be used analytically as well.

$$s = \frac{(U - U_{pol}) \cdot \sigma}{J} \leftrightarrow U_{pol} = U - \frac{s \cdot I}{\sigma \cdot A} \quad \text{Equation 2-22}$$

The most important reason for the use of the simulation, schematically shown in Figure 6-1, is the correction of the total current into a current through the frontal gap and over the side gap. Based on the COMSOL model the necessary corrections to the data recorded in the experiments can be broken down to the relationship between current density and gap presented in Figure 6-2 and Figure 6-3.

The provided corrections are calculated for the previously introduced experimental setups and the associated geometries. By using this correction, no further complication to the experiments, e.g. a complex isolation of the electrodes, was necessary.



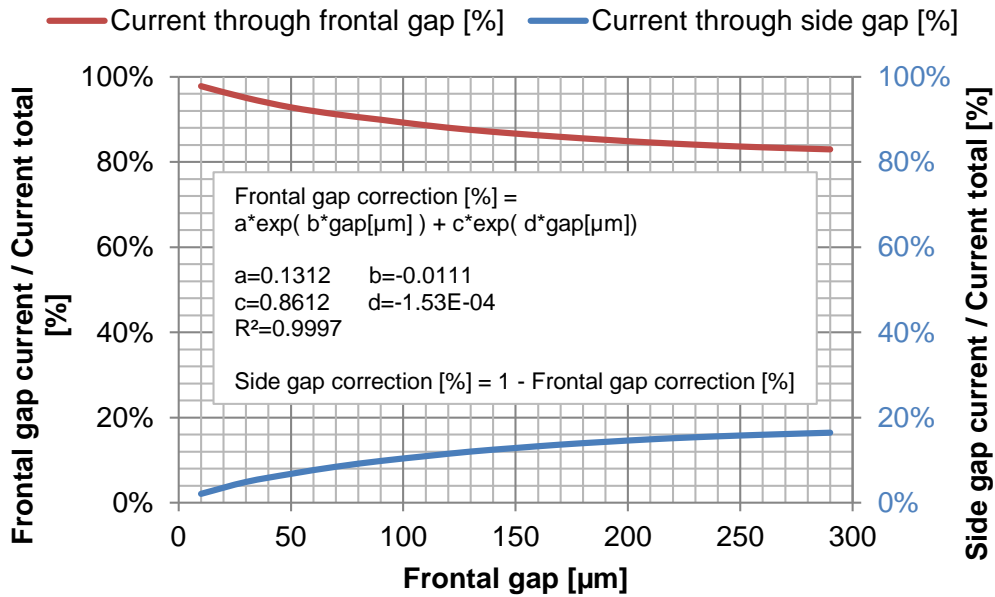


Figure 6-2 Diameter correction 1.4301 setup  
(Diameter: Anode 6 mm vs. Cathode 8 mm)

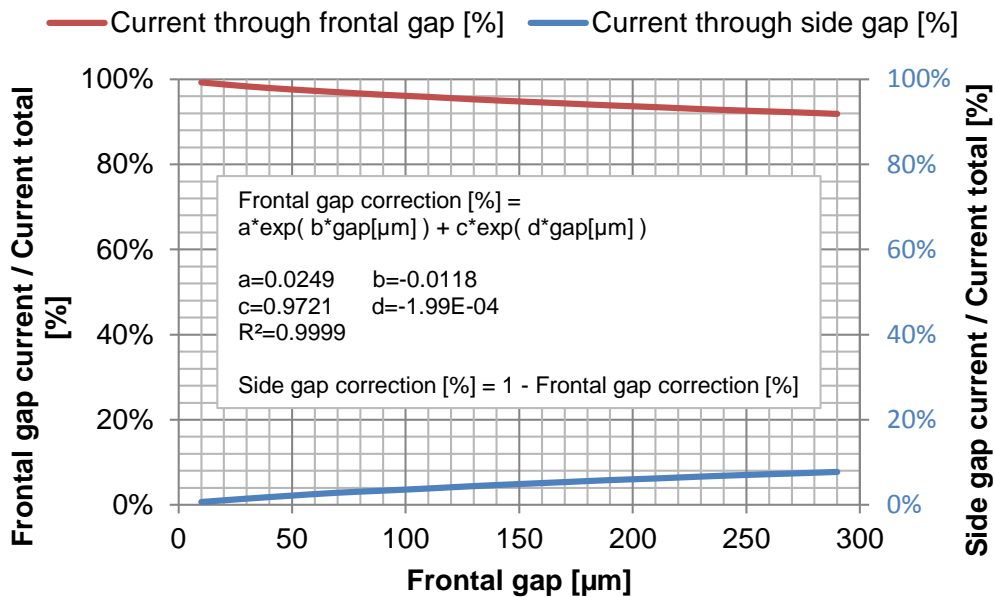


Figure 6-3 Diameter correction S390 setup  
(Diameter: Anode 6.3 mm vs. Cathode 6.3 mm)

For continuous observations, the same static simulation allows a snapshot-like view on the conditions during the machining process. This is exemplarily shown in Figure 6-4. Here an image taken during the continuous observations was used as input for an FEM simulation (modelled as mirror symmetry). The current recorded during the real experiment at a specific time was  $I_{\text{real}} = 5.85 \text{ A}$  at  $U = 10 \text{ V}$ . The static electric field simulation assuming equal boundary conditions calculates an 'FEM current' of  $I_{\text{FEM}} = 5.99 \text{ A}$  and thus a deviation of less than 2.5 %. Even though temperature and

velocity fields are not included in the contemplation, the simulation offers the possibility to specifically look into either frontal or side gap current distributions, which is not possible in the experiment.

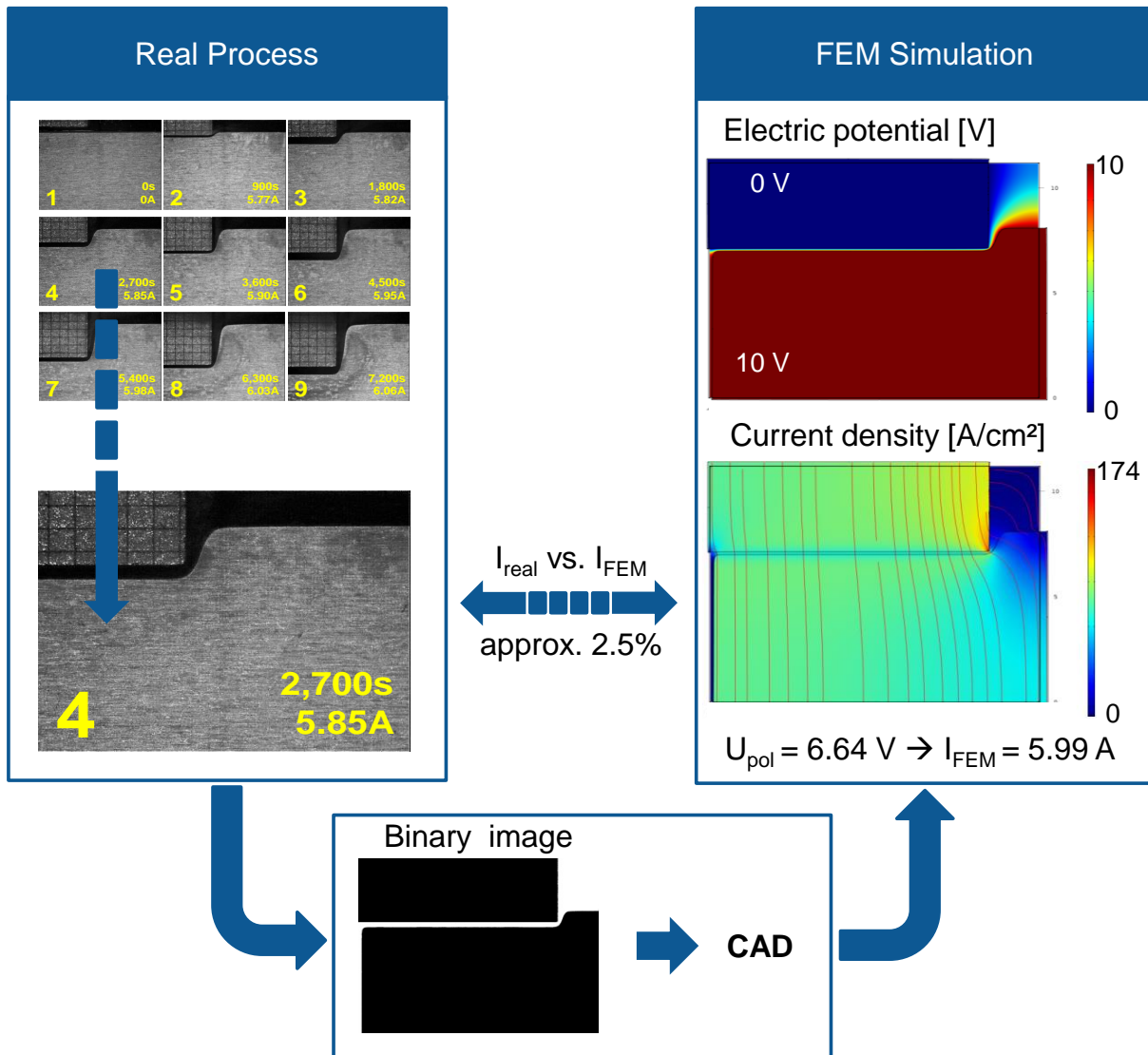


Figure 6-4 Simulation of a process snapshot [87]

## 6.2 Simulation based on material-specific data

To machine a shape in respect to a desired geometric specification using PECM, a tool has to be designed considering the material removal particularities. Especially the gap evolution at different gap sizes over time is of particular difficulty. The first approaches towards anode shaping and predefined tool geometry were based on the potential boundary conditions. The dissolution rate towards the surface normal was connected to the feed rate under steady-state ECM conditions. The angle between the surface normal and the feed rate direction was connected using either the cosine [28, 37] or sinus [11, 108]. In accordance to the angle, the shape was then calculated using the finite-difference equation corresponding to Laplace's equation and Ohm's

law. After approaches towards the multistage electrochemical shaping [109] the accuracy problems in PECM [110] came into focus around 1981. Since focusing on the steady-state or equilibrium conditions, the materials investigated had to be available in a standardized form. Different combinations of parameters were chosen. The passivating electrolytes were defined by Rajurkar [111] using  $K_m$  and  $K_v$  curves. Yet instead of defining own parameters or correlations, the material representation based on underlying laws seems to be the more reliable source of information. In this case the SMR and current density relationship following Faraday's law and the gap and current density relationship according to Ohm's law was chosen to assure reproducibility.

As early as 1977, Lindenlauf [41] described six different types of current density versus removal rate (which equals the feed rate under steady-state conditions) characteristics, Figure 6-5 schematically shows two of these classifications. The curves resemble a simple material model for electrochemical removal. While Type A, as classified and named in Lindenlauf [41], describes the NaCl based material behavior, Type D describes the NaNO<sub>3</sub> based, passivating material behavior. In the following the materials are classified in accordance to Type D, since using NaNO<sub>3</sub> as electrolyte.

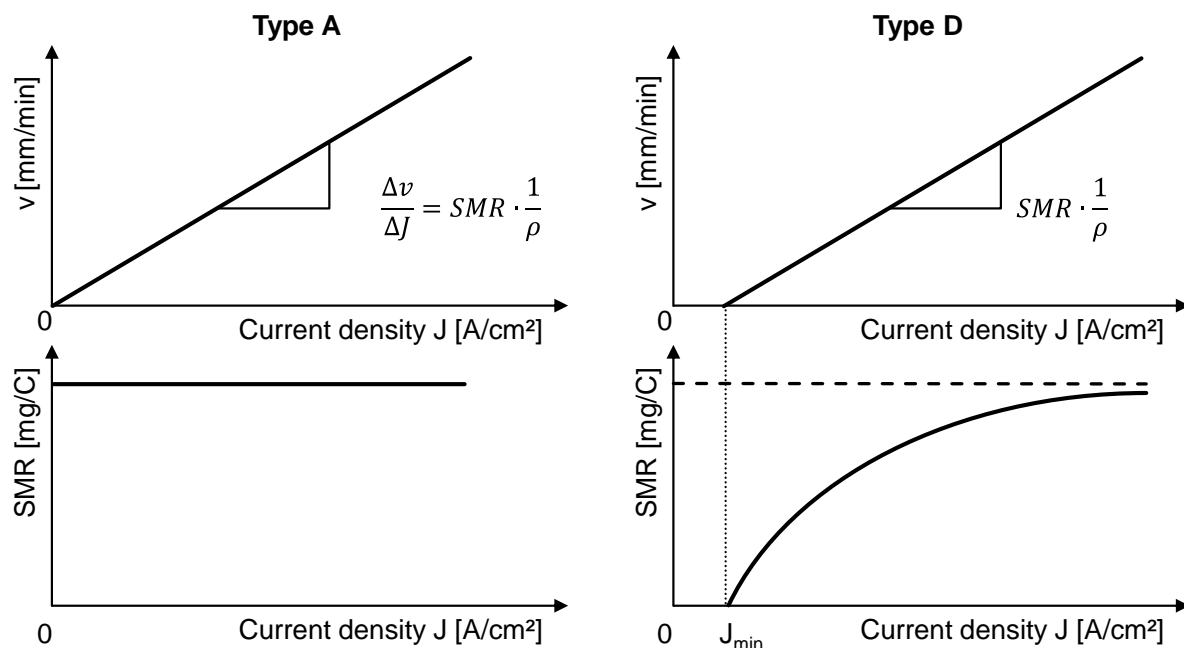


Figure 6-5 Classification of materials, similar [41]

In Table 6.2 the mathematical background shown in Figure 6-5 is provided. While the relationships of Type A can be described using Faraday's law, this cannot be done for Type D materials, since the passivation causes a nonlinear behavior.

Table 6.2 Classification of materials, similar [41]

Type A	$v = MRR \cdot J = SMR \cdot \frac{1}{\rho} \cdot J$ $SMR = \frac{v}{J} \cdot \rho = const.$	Equation 6-1  Equation 6-2
Type D	$v = MRR \cdot (J - J_{min}) = SMR \cdot \frac{1}{\rho} \cdot (J - J_{min})$ $SMR = \frac{v}{J - J_{min}} \cdot \rho \neq const.$	Equation 6-3  Equation 6-4

This procedure is neither fully applicable, since Faraday's law does not allow the specification of a maximum dissolution without knowing the valences, yet a linear relationship with respect to time, electrical current and a material constant (SMR or MRR) is possible. In addition, a maximum dissolution per current density results from the need to feed the cathode towards the anode in ECM. When the feed rate becomes faster than the material dissolution a contact of the electrodes will ultimately occur. While these relationships were defined for ECM, literature provides an indication about the difference between material characteristics towards PECM. The curves shown in Figure 6-6 schematically provide the current efficiency yield of the ECM process as function of the current density in a continuous voltage compared to a pulsed voltage case. The pulse durations according to the source were 1 ms with a pause of 10 ms [112]. At a constant current density the material shows a stronger decrease in efficiency using PECM than ECM. Similar relationships about the current efficiency being lower in the case of pulsed conditions and the course of the curves can be found in Moser [65] and Altena [8].

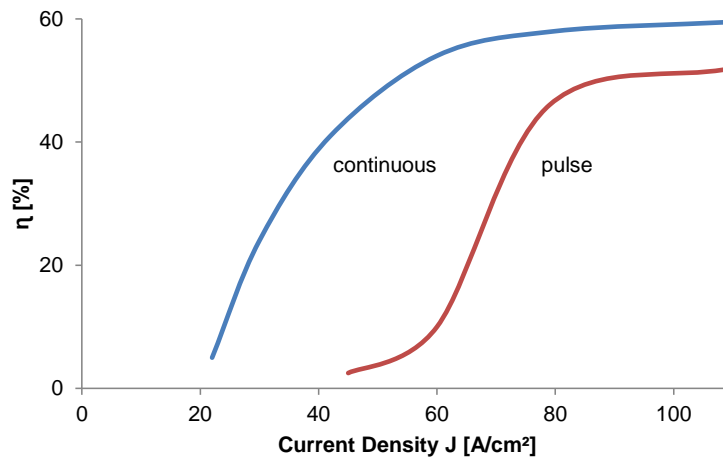


Figure 6-6 Current efficiency in ECM and PECM, schematic similar [112]

Different approaches are possible to describe a material using a consistent model. Most of them are based on the current efficiency and current density relationship [70] [113, 114, 115]. The approach used in this work is based on modelling the material behavior when using a tanh-based function, which was presented in the work of DeSilva, Altena and McGeough [114]. The function, according to Altena [44], describes the material behavior as SMR in respect to the applied boundary conditions as follows:

$$SMR = a \cdot (\tanh(b \cdot t_{on} + c) \cdot J + (d \cdot t_{on} \cdot e)) + f + e_v \quad \text{Equation 6-5}$$

The individual factors can be derived using a curve fitting module, as integrated in most of today's mathematical software tools. All calculations and models herein were programmed in Matlab R2012a, by the Mathworks company.

With a possibility to model the material behavior using either NaCl or NaNO<sub>3</sub>, a simulation based on this material-specific data can be made. Based on the mathematical fundamentals of ECM shaping [70] and iterative simulation [116], two scientists and their respective groups have put a lot of effort into the modelling of electrochemical processes. In particular the group and persons working with Kozak [117, 118, 119, 120, 121, 122] and Deconinck [115, 123, 124, 125, 126, 127] did extensive research in this particular field. Next to the detailed theoretical investigations on individual effects, e.g. temperature [128], electrolyte flow and concentrations, other publications focus more on the modeling and applications of the ECM process [129] - like the multiphysics simulation of the ECM process machining a 3D compressor blade [130, 131] or the simulation using nominal gap-voltage and cosine approach for the material Inconel 718 [43, 132]. Most of these approaches and the state-of-the-art simulation were summarized by Hinduja and Kunieda in the work "Modelling of ECM and EDM processes" [45] in 2013. While most of the mentioned works focus on the process from a rather theoretical approach, the simulation method used in this work focuses on a simple, yet robust

method based on experimental data similar to the approach used by the group around Mount and Clifton [133, 134, 135]. The calculation steps implemented in Matlab are presented in Figure 6-7.

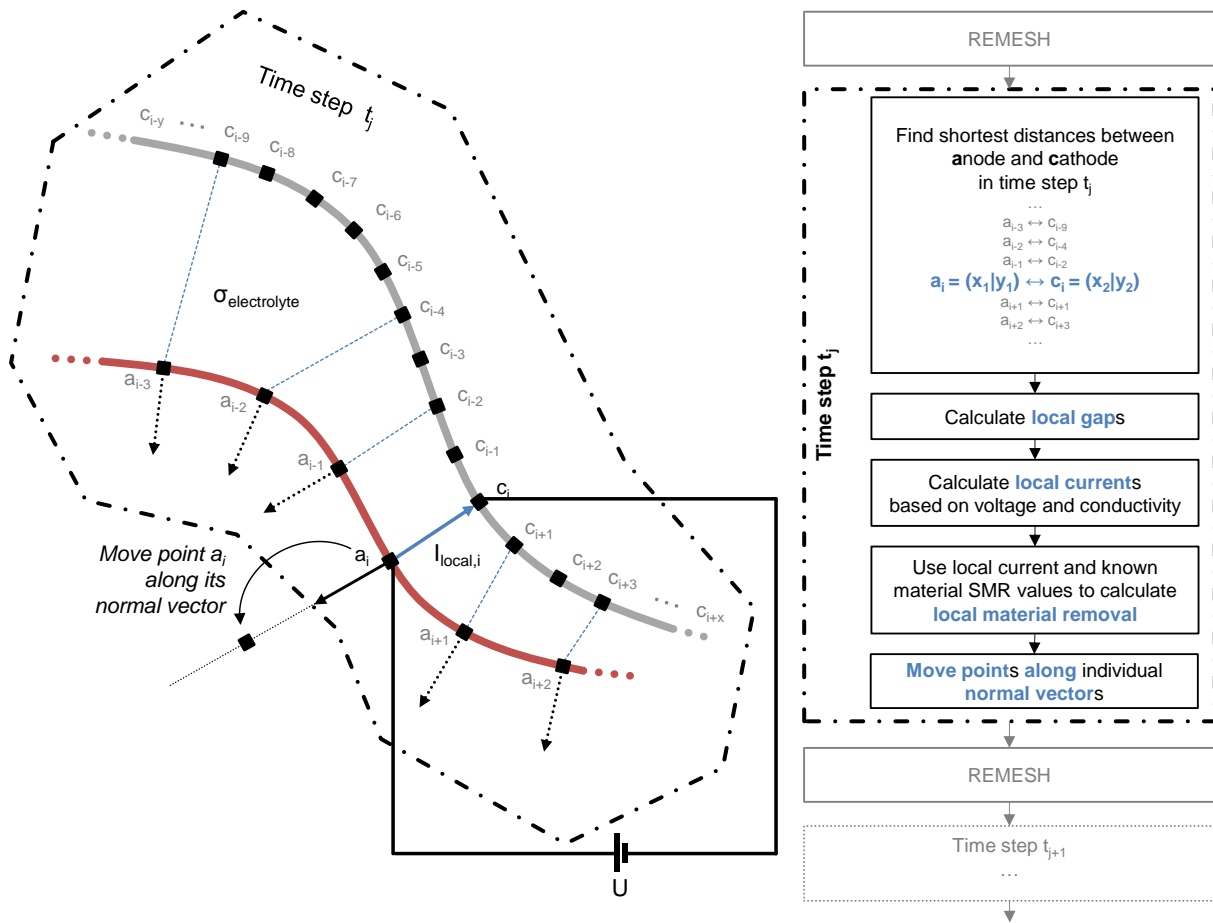


Figure 6-7 Scheme of the calculation steps implemented in Matlab

Starting from the shape of a segmented cathode and anode, the closest distances between points are determined. With the knowledge of the individual distances, the current for a given potential can be calculated using Ohm's law and then Faraday's law can be applied using the SMR values, which were determined experimentally.

The material removal (movement) at each individual point ( $\overrightarrow{dh_{a_i}}$ ) takes place in normal direction towards the anodic surface. Based on the individually calculated shortest distance and the voltage as boundary condition, the current density for each point is calculated and then the point is moved in normal direction according to Equation 6-6. The time-step can be chosen in accordance with the pulse on time  $t_{\text{on}}$  or as a multiple of it. Yet, the accuracy improves when using a time stepping equal to the pulse on time, since a wider data range in the material model is used.

$$\frac{\overrightarrow{dh_{a_i}}}{dt} = \frac{M}{z \cdot F \cdot \rho} \cdot i_{\text{local},i} \cdot \vec{n} \cdot t_{\text{on}} \cdot f$$

Equation 6-6

A complete calculation loop, incorporating the overall steps in the iteration, is presented in Figure 6-8. The termination criterion in the calculation is the preset anodic target depth.

### **6.3 Tool simulation based on material-specific simulation**

With the possibility to simulate the electrochemical dissolution based on material parameters and given tool shape, the next step is the adaptation of the tool in order to achieve a desired shape. The inverse tool simulation based on experimental data can be performed for either  $\text{NaNO}_3$  or  $\text{NaCl}$ -based electrolytes. In the case of  $\text{NaCl}$ , this approach shows a high significance, since the SMR values using  $\text{NaCl}$  are usually higher than in the case of  $\text{NaNO}_3$ . Hence the productivity of the process can be improved by using a specially shaped tool. This tool, calculated on the basis of simulation would allow faster, yet equally precise machining without the disadvantages of passivation at the work piece surface. In the past, graphical methods were used, but only after the introduction of computerized procedures, it became possible to iteratively calculate experimental tools based on anodic specifications [22, 24, 136, 137, 138]. Based on the previously presented simulation of the removal, an extension of the scheme by adding an outer loop for the calculation of cathode geometries is used and pictured in Figure 6-8. The forward simulation (anodic dissolution), using a consistent tool shape, is hereby integrated in each iterative loop. After each forward simulation the desired anodic shape and calculated shape are compared with each other and the geometric differences are used as correction factors for the cathode geometry. After each correction, the loop is repeated, until a pre-defined termination criterion is reached, or the desired geometry is achieved to a certain extent.

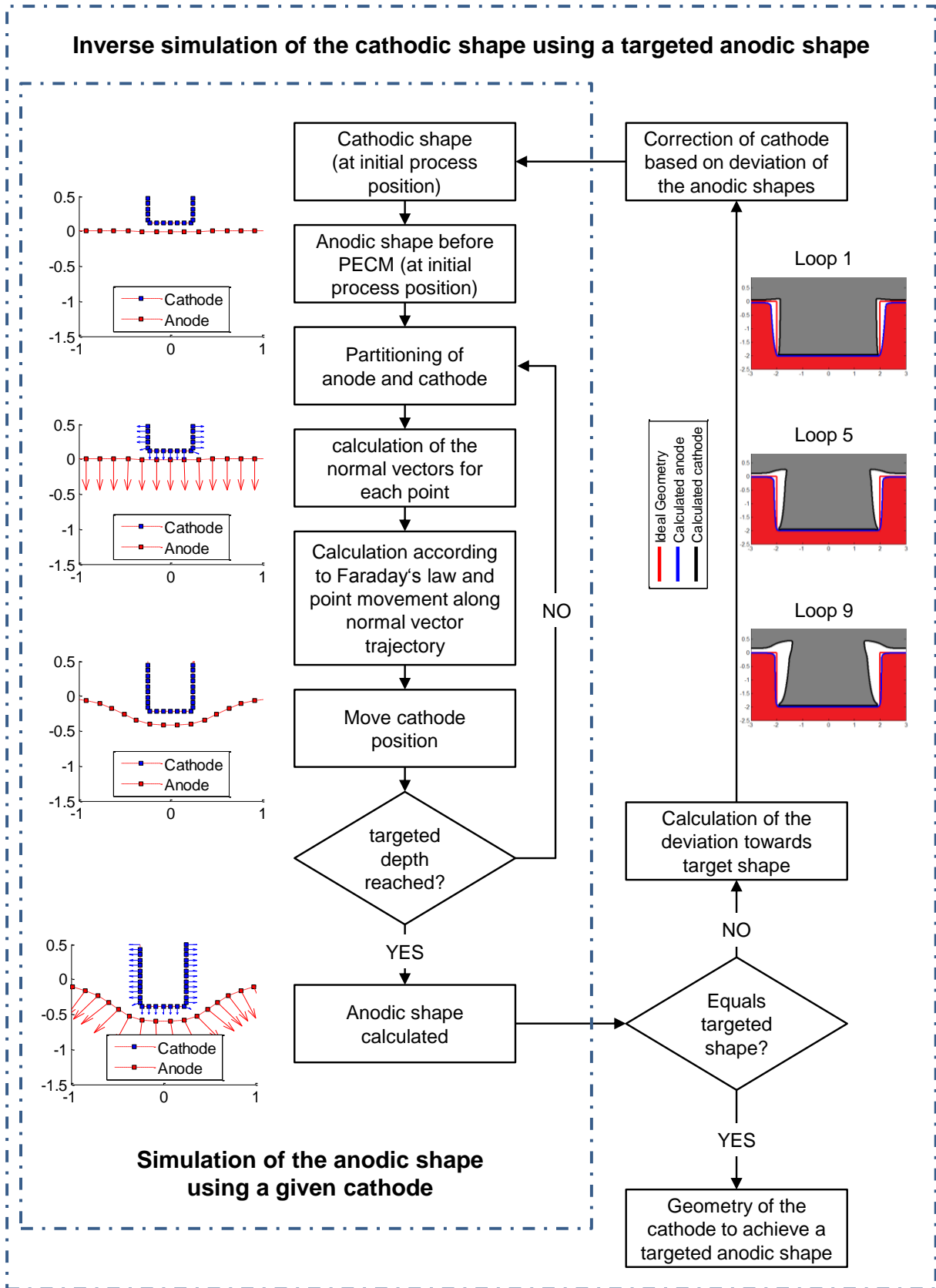


Figure 6-8 Sequence of a simulation with examples  
 Inside loop: Simulation of the anode geometry using a given cathode  
 Outside loop: Iterative inverse simulation of the anode and cathode geometry using a targeted anode geometry



## 7 Experimental Results, Simulation and Discussion

### 7.1 Material-specific data

#### 7.1.1 Stainless steel 1.4301

The results obtained using the frontal gap experiments and side gap experiments will be presented in this paragraph. Each data point presented in the figures represents the result of one experiment at equilibrium conditions. While some of the experiments took only a couple of seconds when using high feed rates, others needed several minutes in order to reach the steady-state conditions. Roughly 90 frontal gap experiments were carried out to investigate the material behavior using the voltages of 7.5 V, 10 V, 12.5 V and 15 V in combination with the pulse on times 1 ms, 2.5 ms and 4 ms. Using these combinations, roughly 117 side gap experiments with a duration lasting from 0.5 seconds up to 34.13 minutes were also investigated.

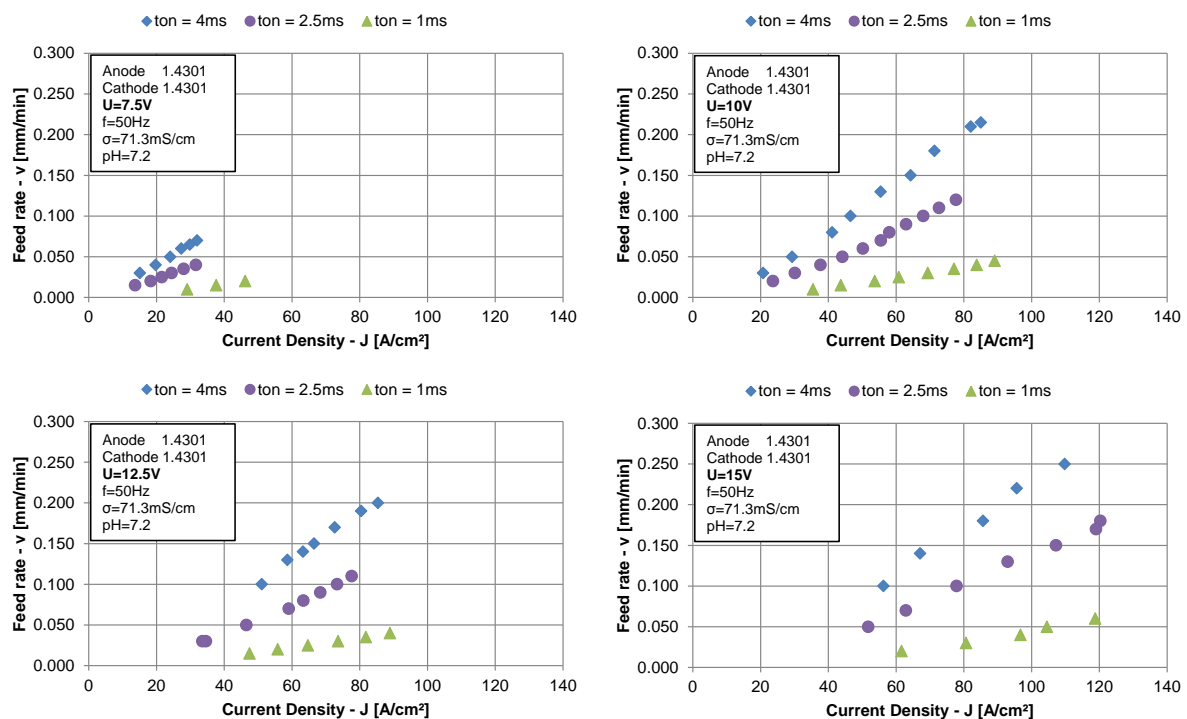


Figure 7-1 Current density [A/cm²] vs. feed rate [mm/min]

The results of the frontal gap experiments in regard to Faraday’s law are presented in Figure 7-1. Although the experiments were performed setting a feed rate and obtaining an associated current density, the axes of the diagrams are intentionally swapped due to later explanations and conditions. Figure 7-2 shows the results in terms of SMR using the transformation following Equation 2-15 corrected by the pulse-pause ratio in PECM. In order to develop an empirical model, the experimental results with regard to Ohm’s law are necessary. For each dataset Figure 7-3 shows the correlation between current density and frontal gap value. The data proves the

gap and current density correlation is independent of the pulse time during the experiments.

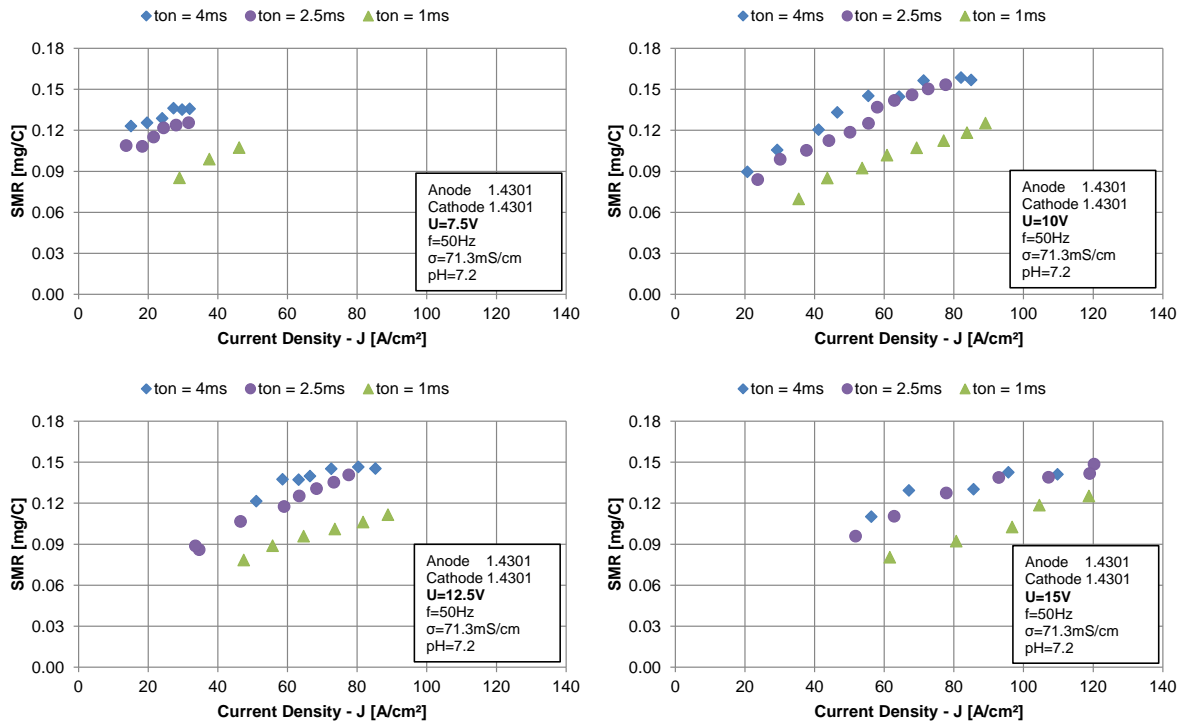


Figure 7-2 Current density [A/cm²] vs. SMR [mg/C]

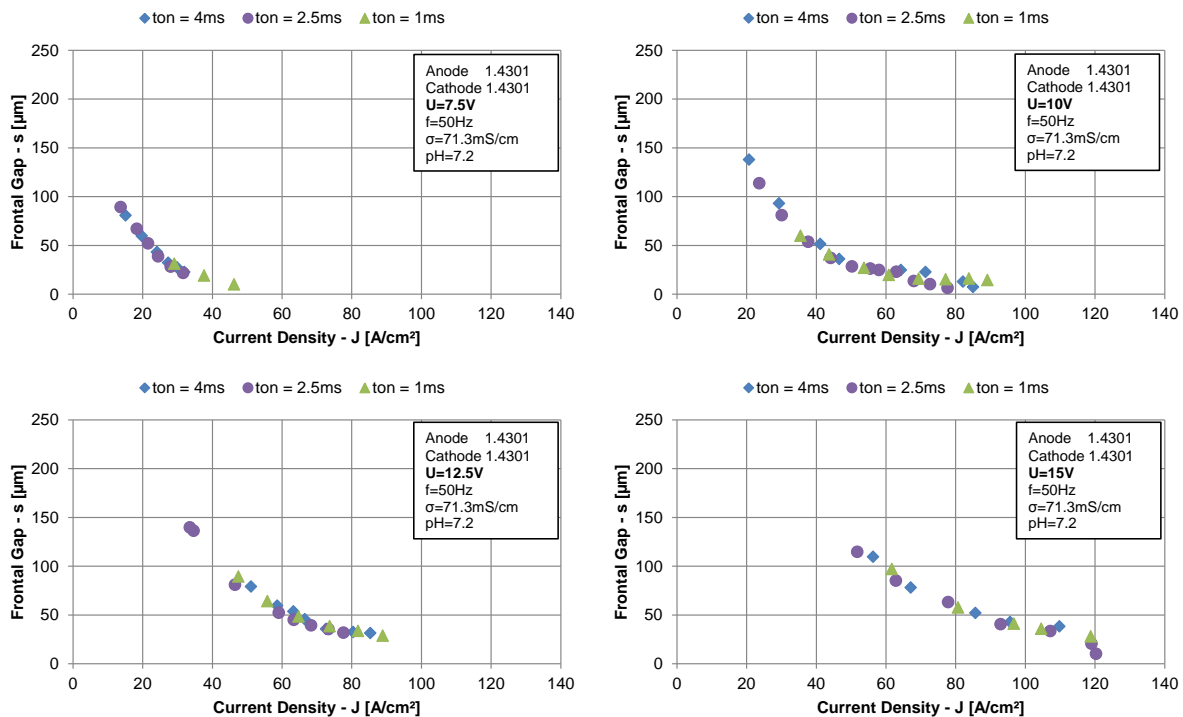


Figure 7-3 Current density [A/cm²] vs. frontal gap [µm] for all pulse times [ms] and voltages [V]

The polarization voltage with regard to the current density can be calculated for each point and drawn as a joint representation, see Figure 7-4. From this data, similar to

the approach in [44], the correlation can be calculated for the material 1.4301 as anode and cathode.

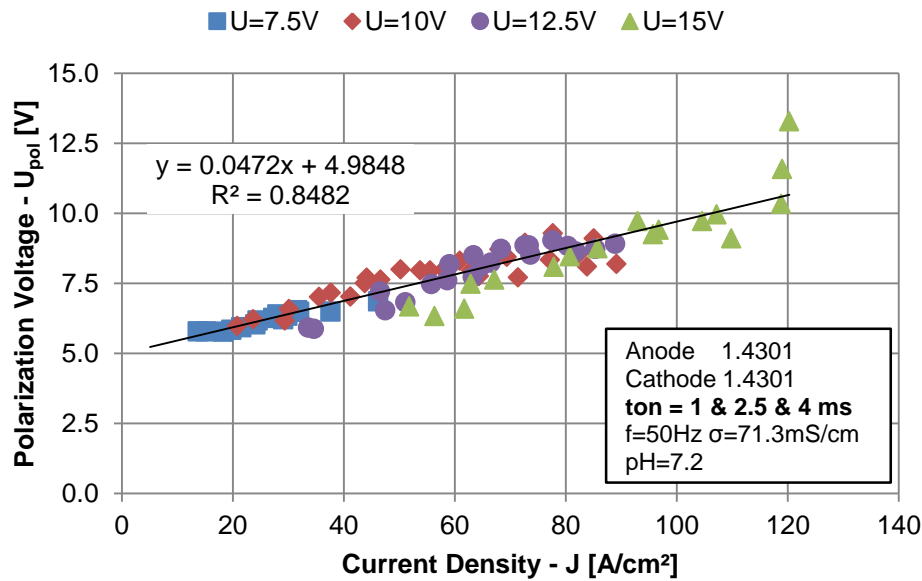


Figure 7-4 Current density [A/cm<sup>2</sup>] vs. polarization voltage [V]

Moreover, the figure shows the maximum achievable current density at a set voltage. For example, no experiments will be possible at a current density of 80 A/cm<sup>2</sup> using a voltage of 7.5 V.

$$U_{pol} = a \cdot J + b \tag{Equation 7-1}$$

with  $a = 0.0472 \frac{V \cdot cm^2}{A}$  and  $b = 4.9848 V$

$$s = \frac{(U - U_{pol}) \cdot \sigma}{J} \tag{Equation 2-22}$$

With Equation 2-22 the current density can be expressed using the variables necessary to describe the shaping precision of the process, the frontal gap *s*, and by using the voltage *U* as input parameter for the machine technology used.

$$J = \frac{\sigma \cdot (U - b)}{a \cdot \sigma + s} \tag{Equation 7-2}$$

Taking this correlation into account, the feed rate needed to achieve a desired frontal gap value for the material combination 1.4301 towards 1.4301, can be expressed using a linear approach as follows:

$$v = 0.0068 \cdot t_{on} \cdot \frac{\sigma \cdot (U - b)}{a \cdot \sigma + s} + \frac{U \cdot t_{on}}{300 \cdot t_{on} + 350} \left[ \frac{mm}{min} \right] \tag{Equation 7-3}$$

This approach is limited within the boundaries of the experimental data. Figure 7-5 shows a different representation of the previous data. On the left hand side (lhs) it is shown, that the gradient in the experiments is dependent on the pulse on time, yet the intercept with the axis is different for each voltage, which again is a result of the smaller gaps at lower voltage and hence a lower aspect ratio of set voltage towards polarization voltage.

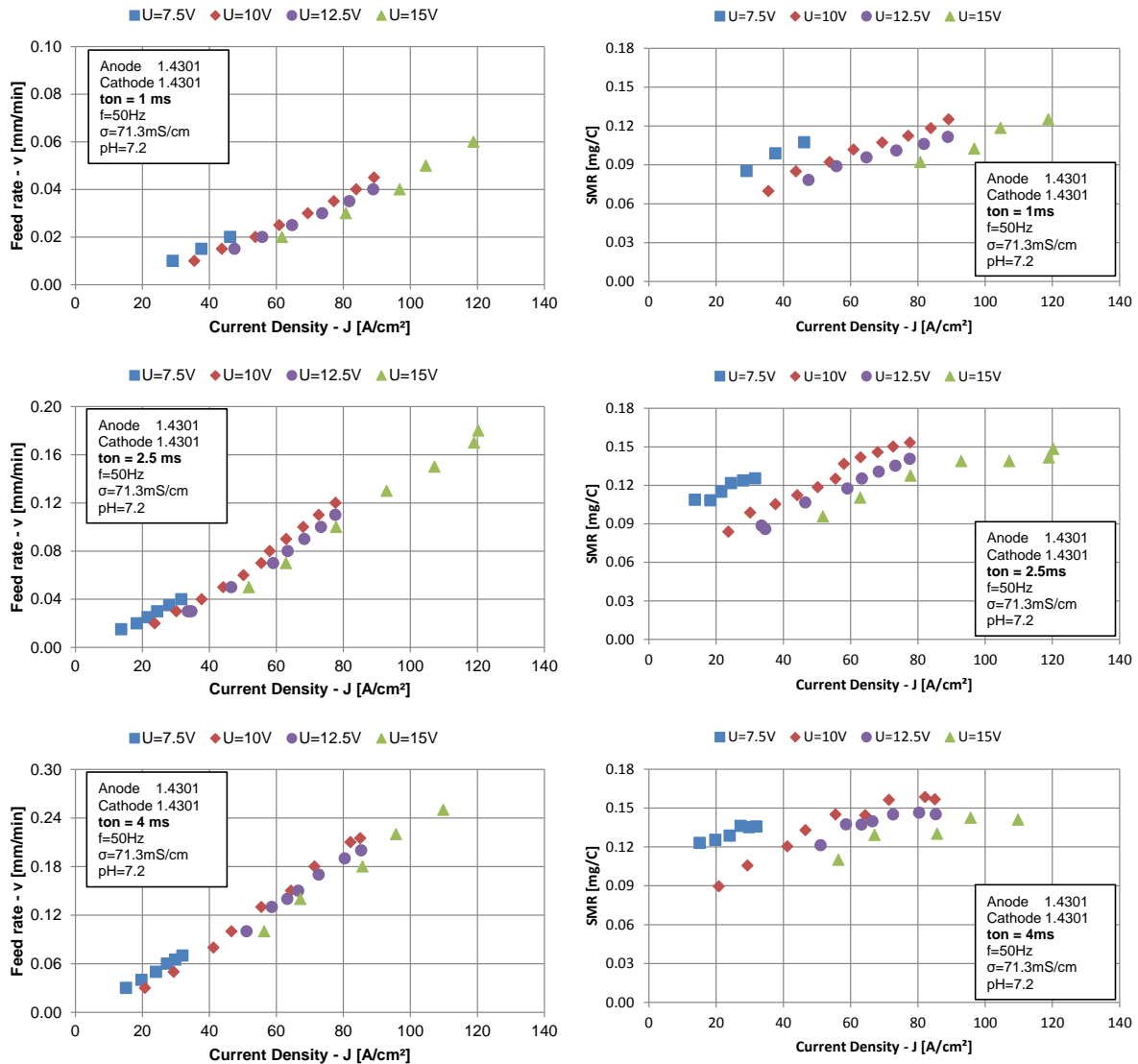


Figure 7-5 lhs: Current density [A/cm<sup>2</sup>] vs. feed rate [mm/min]  
rhs: Current density [A/cm<sup>2</sup>] vs. SMR [mg/C]

Figure 7-6 shows the results of the side gap experiments. At a stationary (no feed rate) and constant mechanical frequency of 50 Hz, pulses of different lengths (1 ms, 2.5 ms and 4 ms) were applied and the gap widening was measured at regular time intervals. As already presented in chapter 5.2, the theoretical approach found in literature does not comply with the data obtained in the PECM experiments. Since the results of the side gap widening do not resemble equilibrium conditions, yet on the contrary are time-dependent results, a description based on the data presented before is not possible. Therefore a general formula based description is not made at

this point. The correlation of these data sets towards the material properties is made using simulation - see results Figure 7-7 - which allows taking into account time-dependent effects.

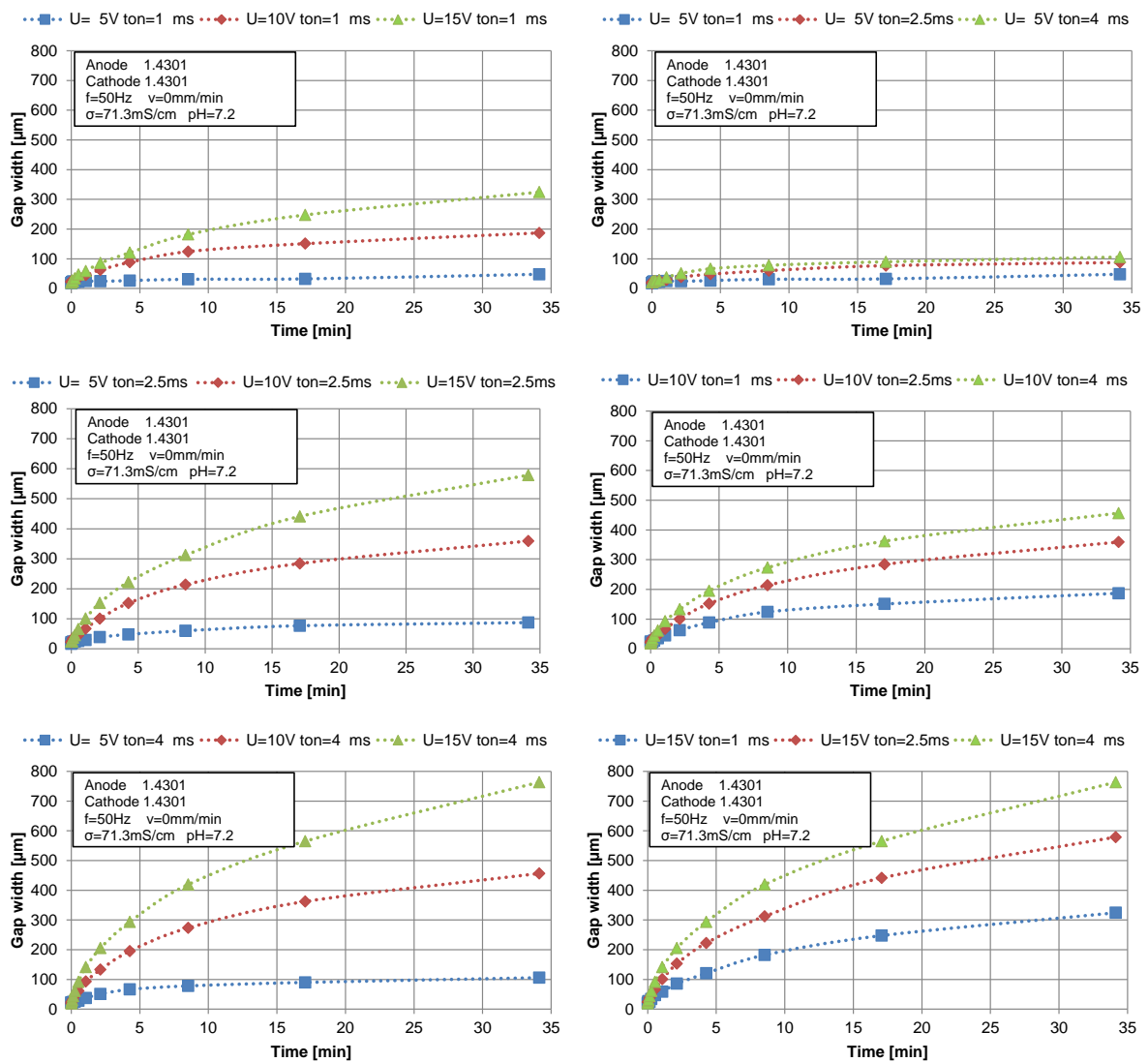


Figure 7-6 Time [min] vs. side gap [μm] development at an initial gap of 20 μm

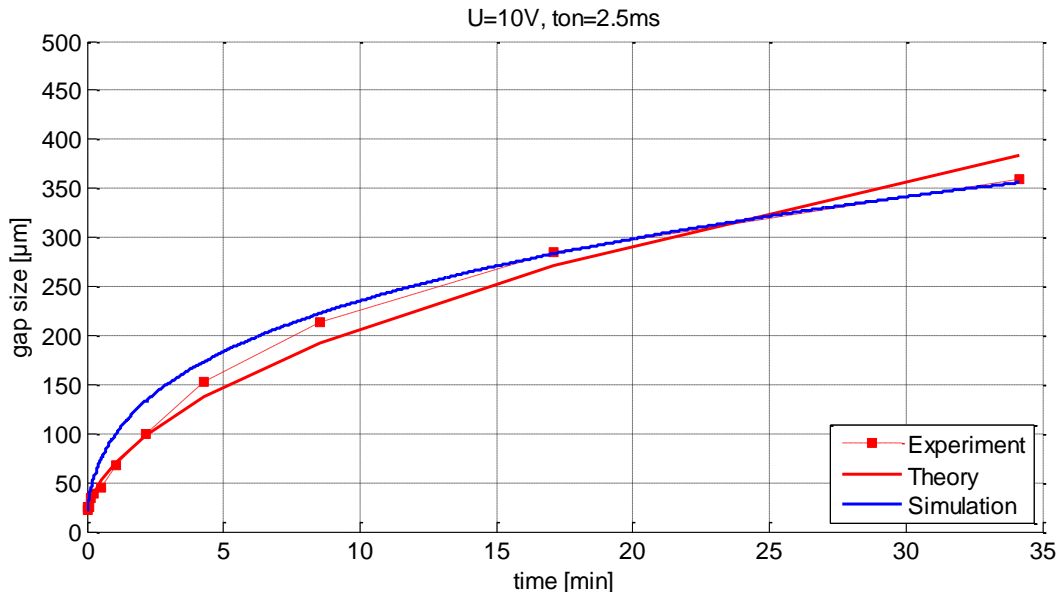


Figure 7-7 Gap widening: Experiment, Theory and Simulation

Next to the geometrical aspects, an important property of PECM machining is the resulting anode surface. In PECM, as well as ECM, the resulting surface roughness depends on the current density during processing. To investigate the surface roughness at different current densities, 12 samples were investigated using optical imaging and SEM microscopy. Figure 7-8 and Figure 7-9 show the results of machining under different equilibrium current conditions.

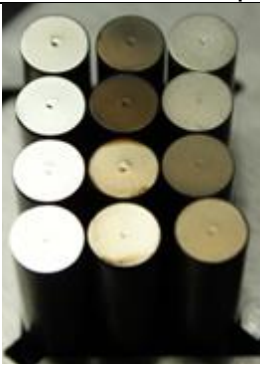
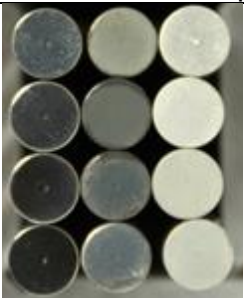
Image taken under a 45° angle towards the sample surface				Image taken under a 90° angle towards the sample surface			
							
	4	8	12		4	8	12
	3	7	11		3	7	11
	2	6	10		2	6	10
	1	5	9		1	5	9
Sample	J [A/cm <sup>2</sup> ]	Sample	J [A/cm <sup>2</sup> ]	Sample	J [A/cm <sup>2</sup> ]		
1	132.0	5	76.1	9	25.7		
2	106.1	6	65.8	10	16.0		
3	92.2	7	52.5	11	8.4		
4	87.4	8	37.6	12	7.2		

Figure 7-8 Optical images of the machined surface

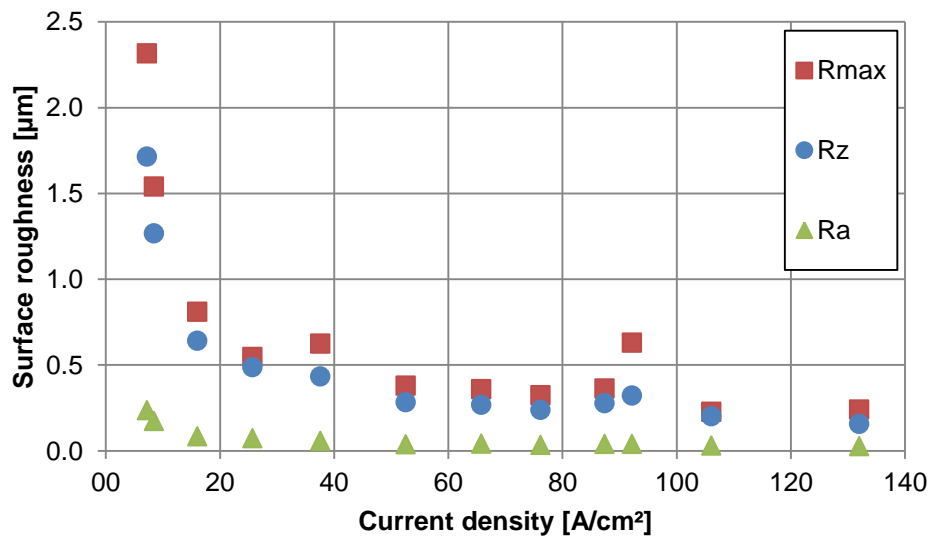


Figure 7-9 Surface roughness of 1.4301 at different current densities [A/cm<sup>2</sup>]

Looking at the results, a visual high-gloss brightness could only be reached at high current densities. To understand the increase in roughness a closer look towards the surface was done using a Zeiss Sigma VP scanning electron microscope (SEM) by Carl Zeiss AG located at the Department of Functional Materials (German: Lehrstuhl für Funktionswerkstoffe) of the Saarland University.

The SEM images in Figure 7-10 show the austenitic microstructure with carbide precipitates in the grain and at the grain boundaries. Similar to the results of Moser [65] and Rosenkranz [48], especially the material at the grain boundaries and the precipitates is preferably dissolved. These localized dissolutions are the reason for the increased roughness at lower current densities.

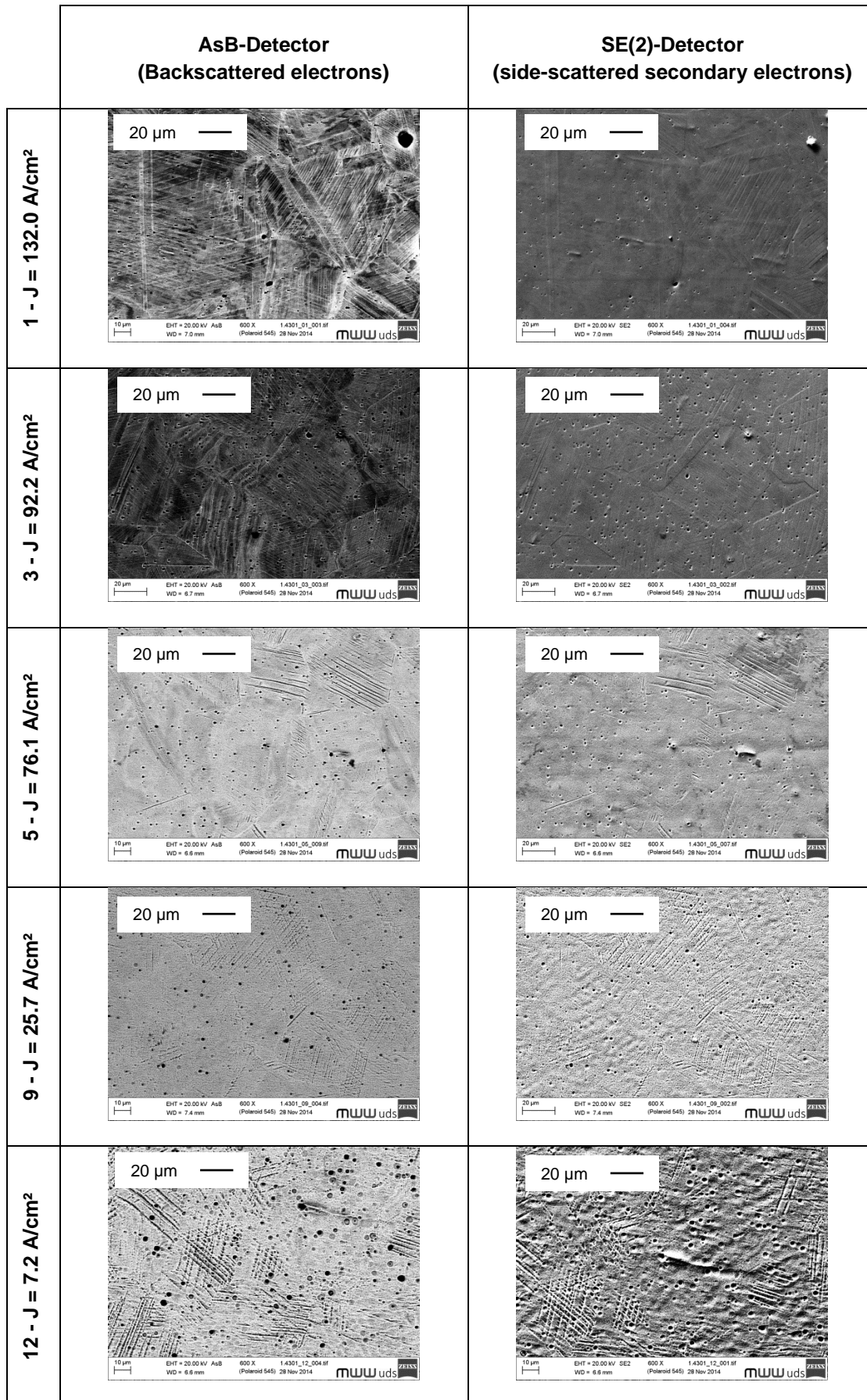


Figure 7-10 SEM surface images of 1.4301 at different current densities



### 7.1.2 Powder metallurgical steel S390

The presentation of the experimental data for S390 follows the one used in the chapter focusing on stainless steel, yet in a compressed form. The left hand side (lhs) images and diagrams present the data collected when machining the soft-annealed S390 samples (short: S390 S) and the right hand side (rhs) data presents the results from machining the hardened S390 (short: S390 H). Roughly 162 frontal gap experiments were carried out to investigate the material behavior using voltages of 7.5 V, 10 V, 12.5 V and 15 V in combination with the pulse on times 1 ms, 2.5 ms and 4 ms - Figure 7-11 to Figure 7-14. Using the same combinations roughly 175 side gap experiments with a duration lasting from 0.5 seconds up to 34.13 minutes were also investigated.

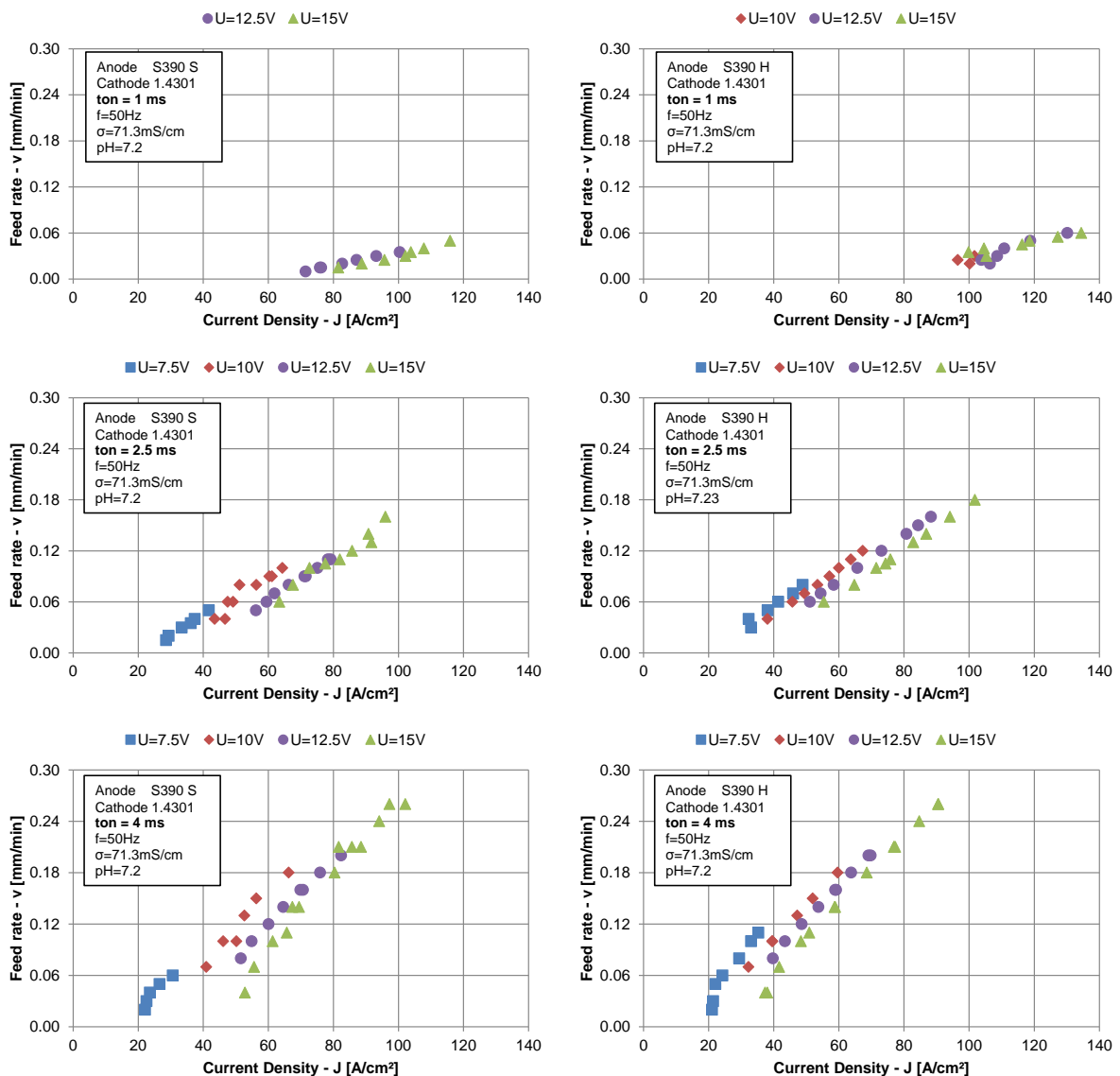


Figure 7-11 Current density [A/cm²] vs. feed rate [mm/min]  
 lhs: S390 soft-annealed / rhs: S390 hardened

The results of the frontal gap experiments are reduced to the data sets which allowed uninterrupted and stable machining conditions. In case of the S390 S, the parameter

combination  $U = 10 \text{ V}$  and  $t_{\text{on}} = 1 \text{ ms}$  did not produce reliable results and for both hardness states the parameter combinations with  $U = 7.5 \text{ V}$  and  $t_{\text{on}} = 1 \text{ ms}$  were not possible at all. The explanation can be found in the pulse-on-time independent polarization voltage. As the data in Figure 7-12 shows, the polarization voltage in case of the hardened S390 is on average lower compared to the soft-annealed S390. This explains why the machining of hardened S390 can be done at lower processing voltages.

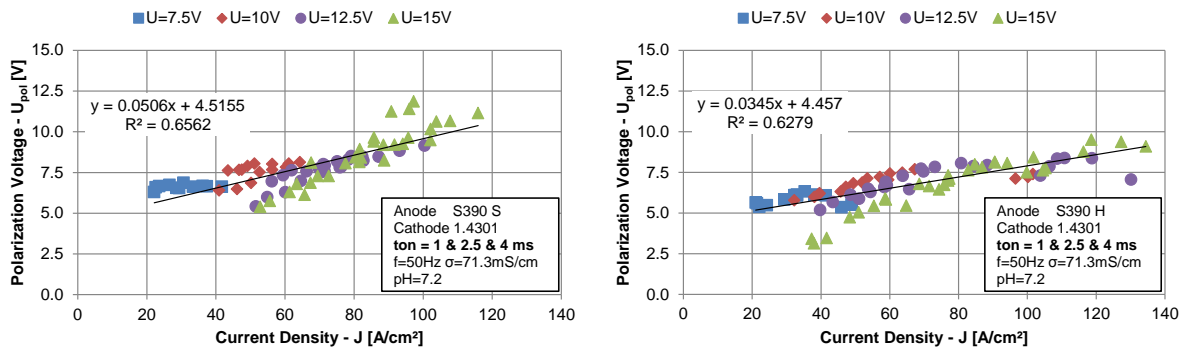


Figure 7-12 Current density [ $\text{A}/\text{cm}^2$ ] vs. polarization voltage [V]  
lhs: S390 soft-annealed / rhs: S390 hardened

$$U_{\text{pol},S390S} = a \cdot J + b$$

with  $a = 0.0506 \frac{\text{V} \cdot \text{cm}^2}{\text{A}}$       Equation 7-4  
and  $b = 4.5155 \text{ V}$

$$U_{\text{pol},S390H} = a \cdot J + b$$

with  $a = 0.0345 \frac{\text{V} \cdot \text{cm}^2}{\text{A}}$       Equation 7-5  
and  $b = 4.457 \text{ V}$

The correlations between current density and polarization voltage can again be used in Ohm's law to describe the current density towards the frontal gap relationship. The data itself overlaid with the theoretical calculations - for  $U = 10 \text{ V}$  in case of S390 S and  $U = 12.5 \text{ V}$  in case of S390 H - are provided in Figure 7-13.

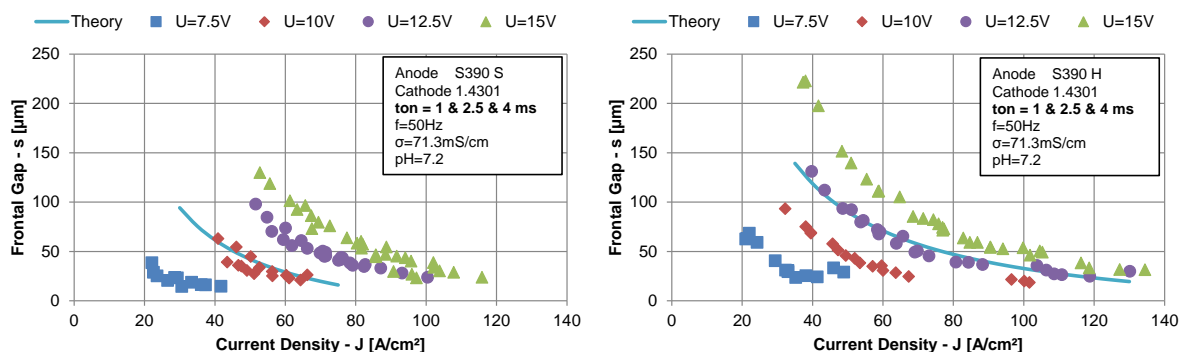


Figure 7-13 Current density [ $\text{A}/\text{cm}^2$ ] vs. frontal gap [ $\mu\text{m}$ ] - including theoretical calculation following Ohm's law - lhs: S390 soft-annealed / rhs: S390 hardened

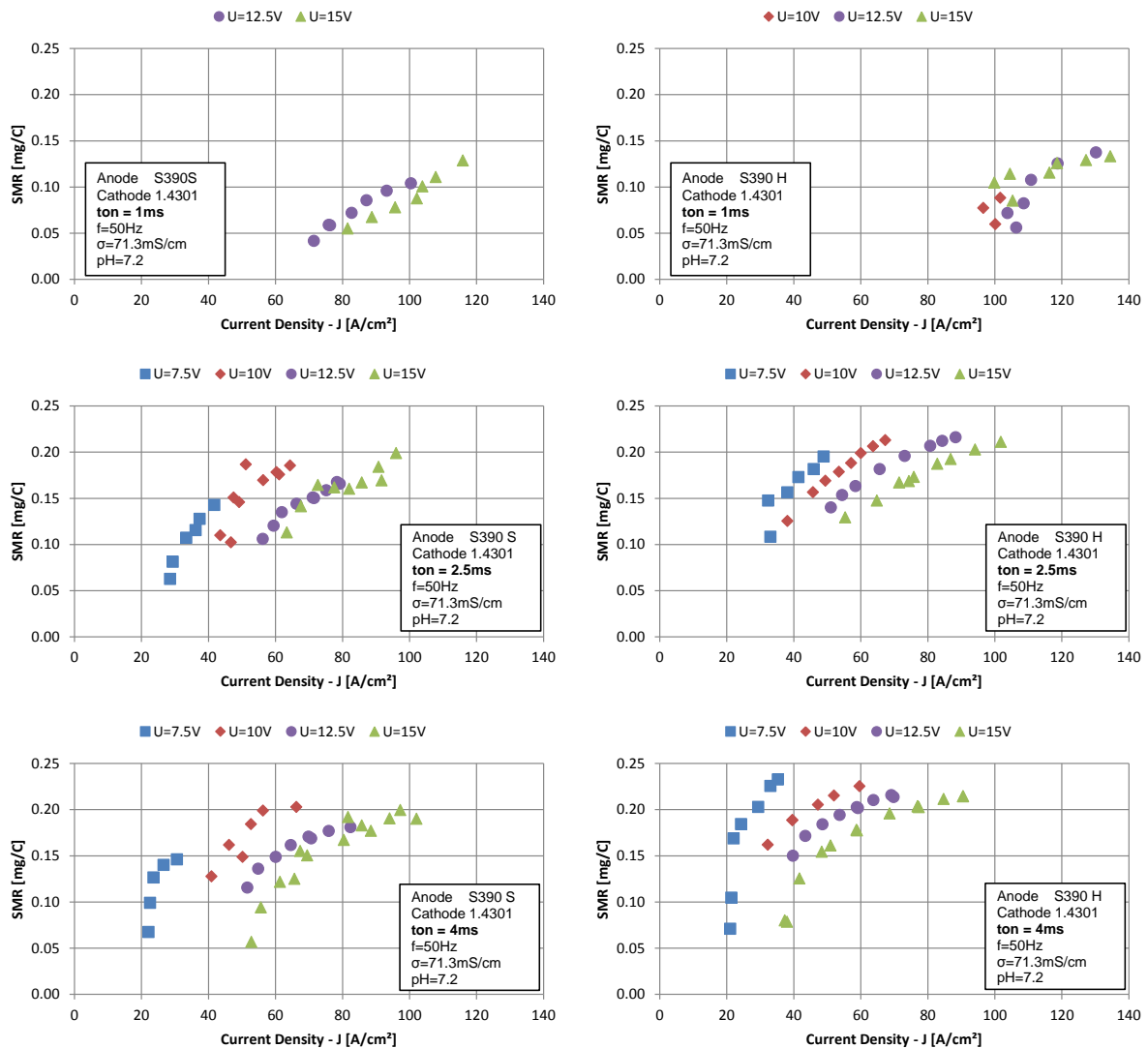


Figure 7-14 Current density [A/cm<sup>2</sup>] vs. SMR [mg/C]  
 lhs: S390 soft-annealed / rhs: S390 hardened

According to the data regarding current density and feed rate, the SMR values presented in Figure 7-14 reflect the higher dissolution rates at lower current densities for the hardened material.

Based on these results, the interpretation of the strongly deviating results from the gap experiments presented in Figure 7-15 can be explained. With a higher overall dissolution rate at equal current densities, the gap widens faster in the case of the hardened material. This effect is the result of the fast drop in current density at around 20 A/cm<sup>2</sup>. Once the current density in the gap drops below this value, the dissolution becomes highly irregular and results in a surface as pictured in Figure 7-16. At this point, the side gap experiments for S390 H were stopped and only the data from experiments which did not show this “fingerprint”-like effect were integrated in Figure 7-15. To investigate the cause for this surface formation with grooves as deep as 14 μm, experiments were performed using lower voltages than the  $U_{pol}$  (Figure 7-12) relationship would indicate are possible.

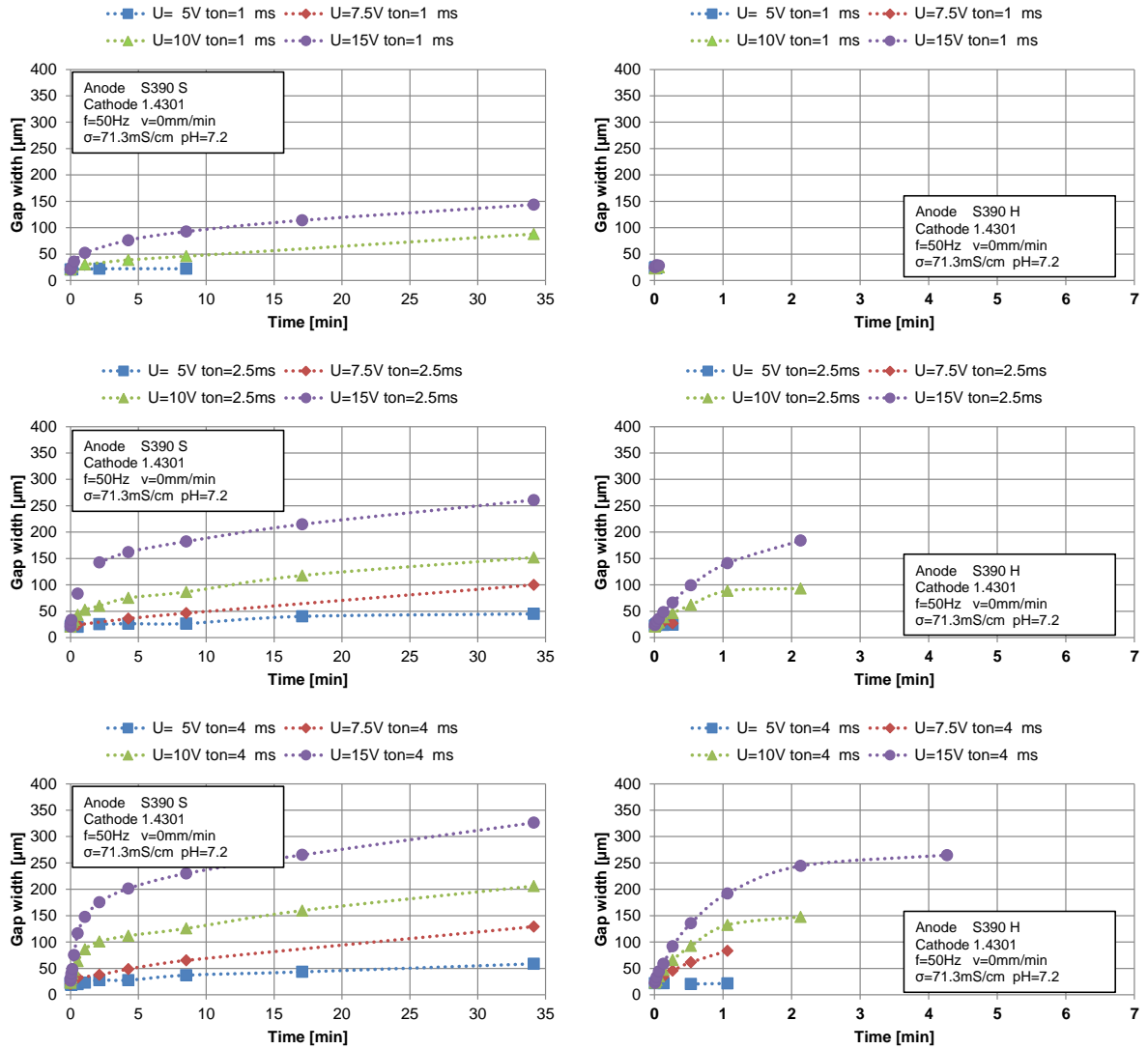


Figure 7-15 Time [min] vs. side gap [μm] development at an initial gap of 20 μm  
 lhs: S390 soft-annealed / rhs: S390 hardened

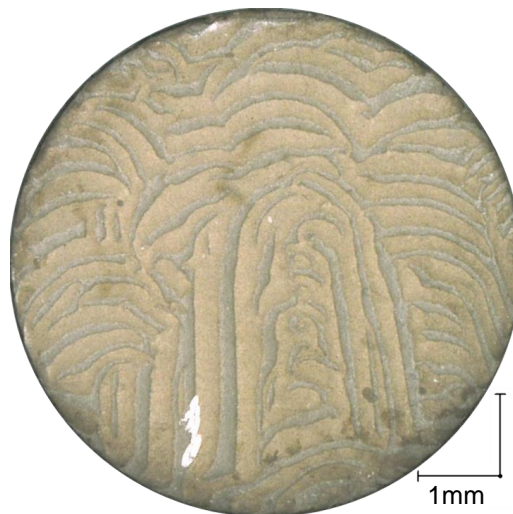


Figure 7-16 Optical image of a S390 surface (∅6.3 mm) after machining at a current density below 20 A/cm<sup>2</sup>

As indicated in the experiments, the gap even widens at voltages below the current density and polarization voltage correlation. Yet, at a voltage of  $U = 5 \text{ V}$  and  $t_{\text{on}} > 1 \text{ ms}$  no full surface dissolution can be observed but rather a slow, localized dissolution enhanced by the flushing conditions and stray current [22]. While in the case of the soft-annealed S390 the carbides are distributed rather loosely in the matrix, the micrographs of the hardened S390 presented in Figure 7-17 show pronounced martensite needles and carbon at the grain boundaries (red arrows).

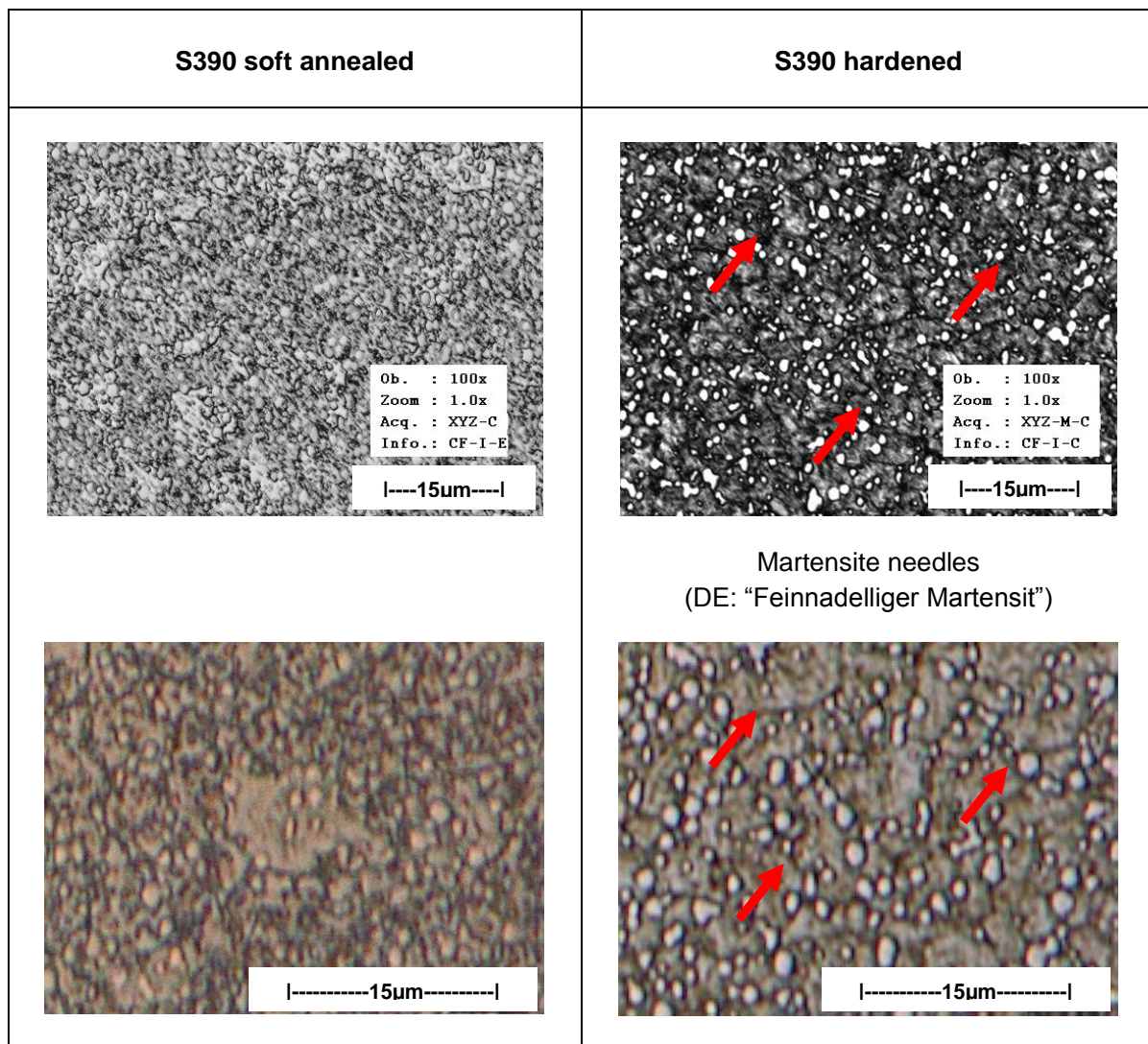


Figure 7-17 Optical micrograph images S390 in soft-annealed and hardened state

By taking a closer look at the materials surface after machining using SEM, a main reason for this effect can be concluded. As shown in the direct comparison between the two hardness states in Figure 7-18, the martensite needles are preferably dissolved at lower current densities. This effect of enhanced dissolution taking place at different geometric-shaped carbon structures in the matrix was already investigated at the example of the carbon content by McGeough [139] in general and specifically in the case of cast iron by Lindenlauf [41] in 1977 and by Weber [140, 141, 142, 143, 144] in recent years.

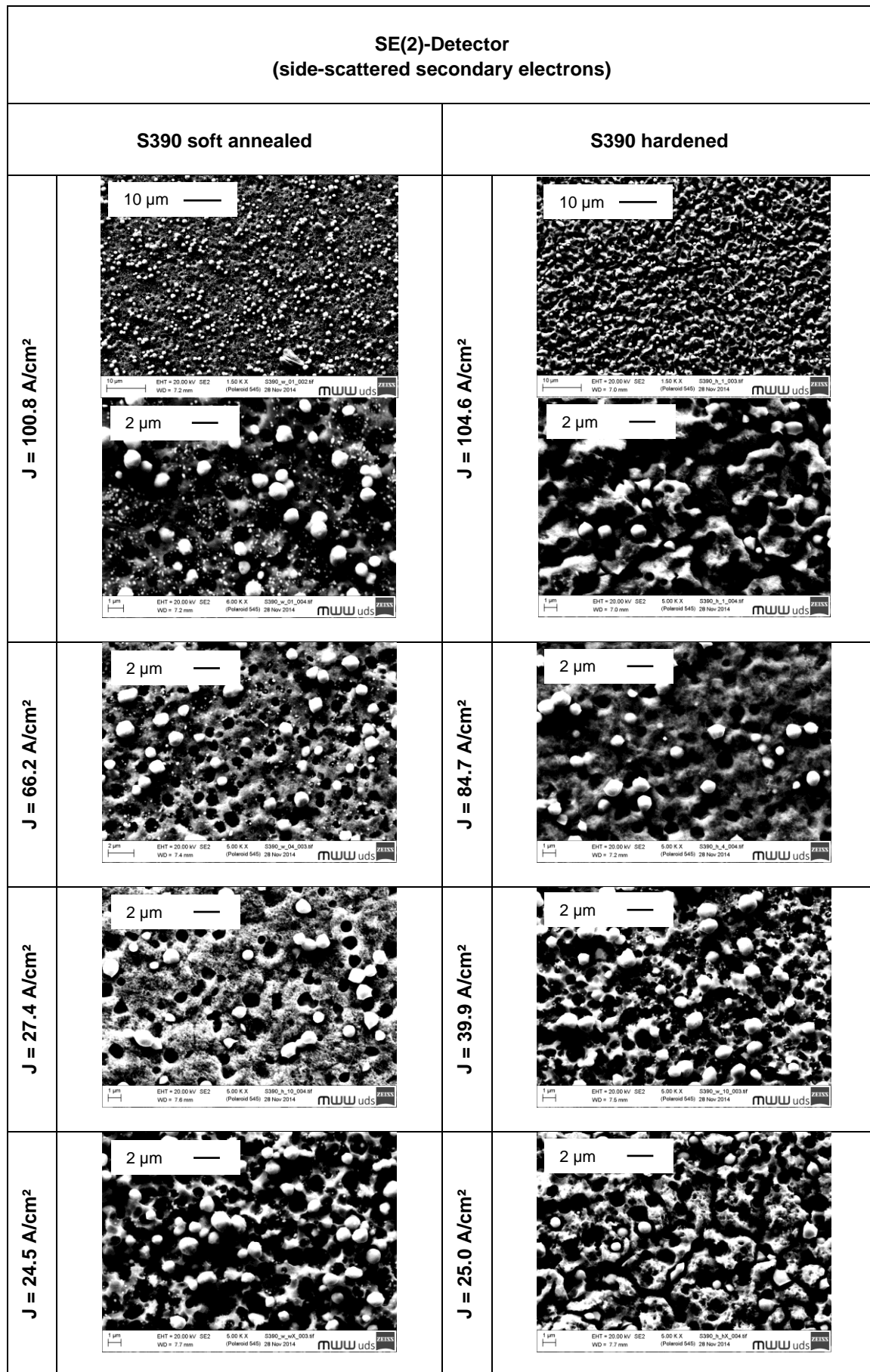




Figure 7-18 S390 SEM surface images at different current densities

According to the previously presented results, the investigation towards the surface roughness under different current conditions was therefore made for current densities above 20A/cm<sup>2</sup>. Table 7.1 shows optical images of the soft-annealed S390 samples after machining under different current conditions (compare Table 7.2).

Table 7.1 S390 S - optical images of the machined surfaces and experimental data

S390 soft-annealed					
Image taken under a 45° angle towards the sample surface			Image taken under a 90° angle towards the sample surface		
	4	8	12		4
	3	7	11		3
	2	6	10		2
	1	5	9		1

Similar to the results machining the hardened material under different current conditions (compare Table 7.3) no optical deviations to the surface can be detected.

Table 7.2 S390 S - experimental data

S390 soft-annealed					
Image taken under a 45° angle towards the sample surface			Image taken under a 90° angle towards the sample surface		
Sample	J [A/cm <sup>2</sup> ]	Sample	J [A/cm <sup>2</sup> ]	Sample	J [A/cm <sup>2</sup> ]
1	108.8	5	66.2	9	33.2
2	100.8	6	59.2	10	30.3
3	93.6	7	53.2	11	27.4
4	78.1	8	37.1	12	24.5

Table 7.3 S390 H - experimental data

S390 hardened					
Sample	J [A/cm <sup>2</sup> ]	Sample	J [A/cm <sup>2</sup> ]	Sample	J [A/cm <sup>2</sup> ]
1	104.6	5	77.3	9	38.8
2	90.5	6	68.6	10	39.9
3	91.9	7	59.0	11	24.9
4	84.7	8	50.9	12	25.0

Similar to the results of Rajurkar [145], who investigated the relationship between surface roughness ( $R_a$ ) and grain size, the size of the tungsten particles in the S390 matrix for both hardness states are in the range of 1-2  $\mu\text{m}$  in diameter. Since these particles cannot be dissolved using the  $\text{NaNO}_3$  electrolyte, the resulting surface roughness will not drop further than the achieved values presented in Figure 7-20 and Figure 7-20, using the pre-defined parameters in terms of pH and conductivity.

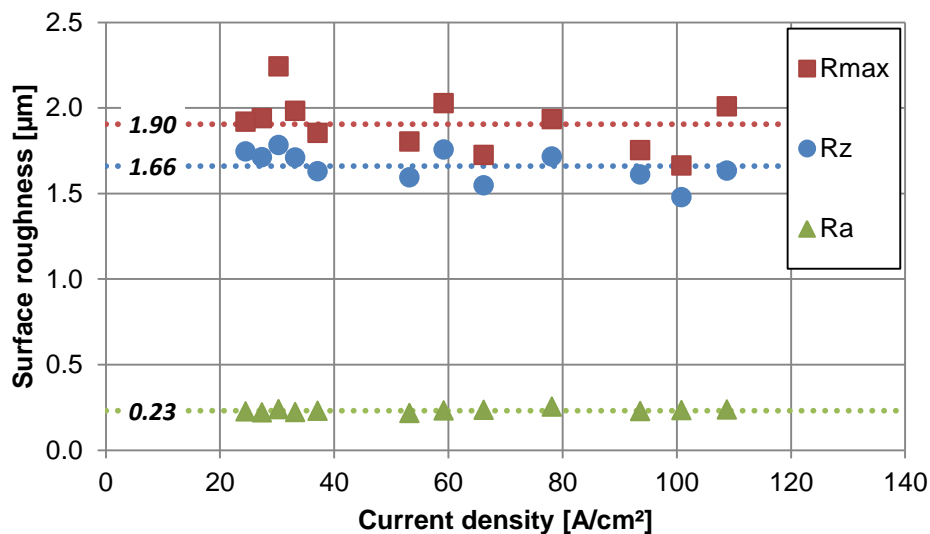


Figure 7-19 Current density [A/cm<sup>2</sup>] vs. surface roughness S390 soft-annealed



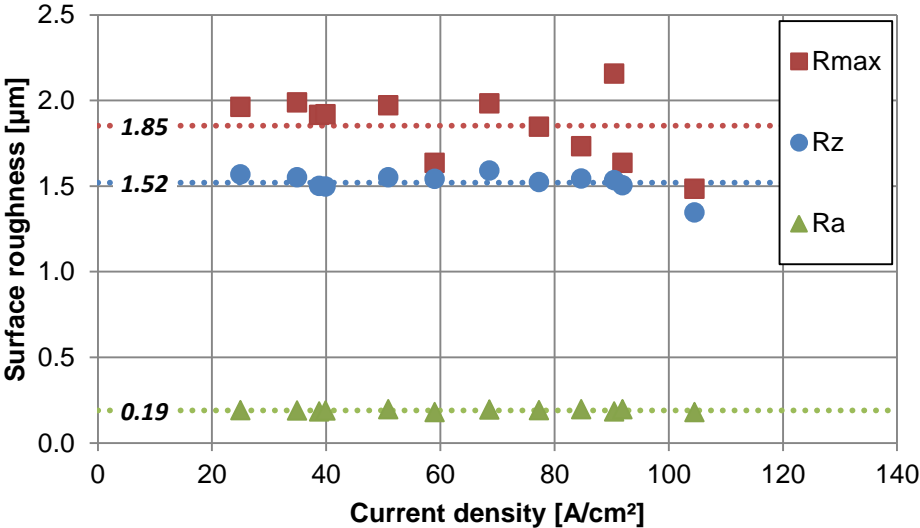


Figure 7-20 Current density [A/cm²] vs. surface roughness S390 hardened

## 7.2 Effects from continuous observations

The introduced setup was built to investigate material dissolution and shaping over time, instead of only focusing on data points from steady-state or equilibrium process conditions. Even though many different shapes can be investigated using the setup constructed and tested, the setup schematically presented on the left hand side in Figure 7-21 was used in most of the following cases. On the right hand side a variety of other shaping processes observable by using the same setup and different anode and cathode geometries are presented. All experiments were made using the material 1.4301 as anode and cathode material.

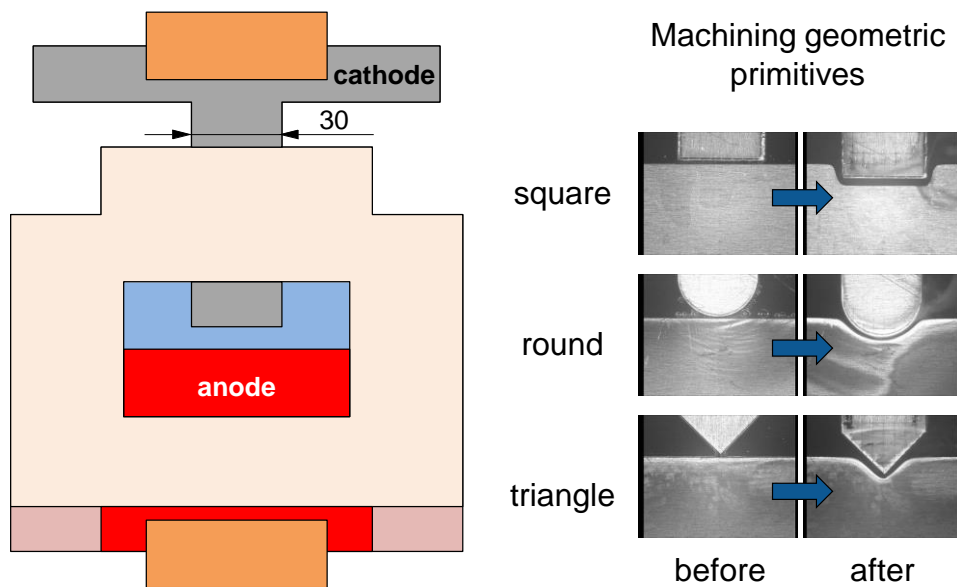


Figure 7-21 Electrode geometries for continuous dissolution and shaping observation

Similar to the frontal gap detection sequence in previous chapters, the first presentation of results focuses on the frontal gap. With the possibility to closely observe and record the shaping process in the area highlighted and indicated in Figure 7-21, the detail in Figure 7-22 gives an overview of the analysis options possible.

Based on an edge detection algorithm programmed in Matlab, the interelectrode gap can be traced for both anode and cathode. In the end, the information retrieved from more than 7,000 individual frames can be combined and the movement of the boundaries can be traced. As pictured in Figure 7-22, the feed rate used in the experiment can be calculated and traced back to the set machining feed rate, which in this case was  $v = 0.027$  mm/min. Besides, the reference structure of  $500\ \mu\text{m}$  times  $500\ \mu\text{m}$  on the cathode can be observed visually and evaluated as size reference using the software.

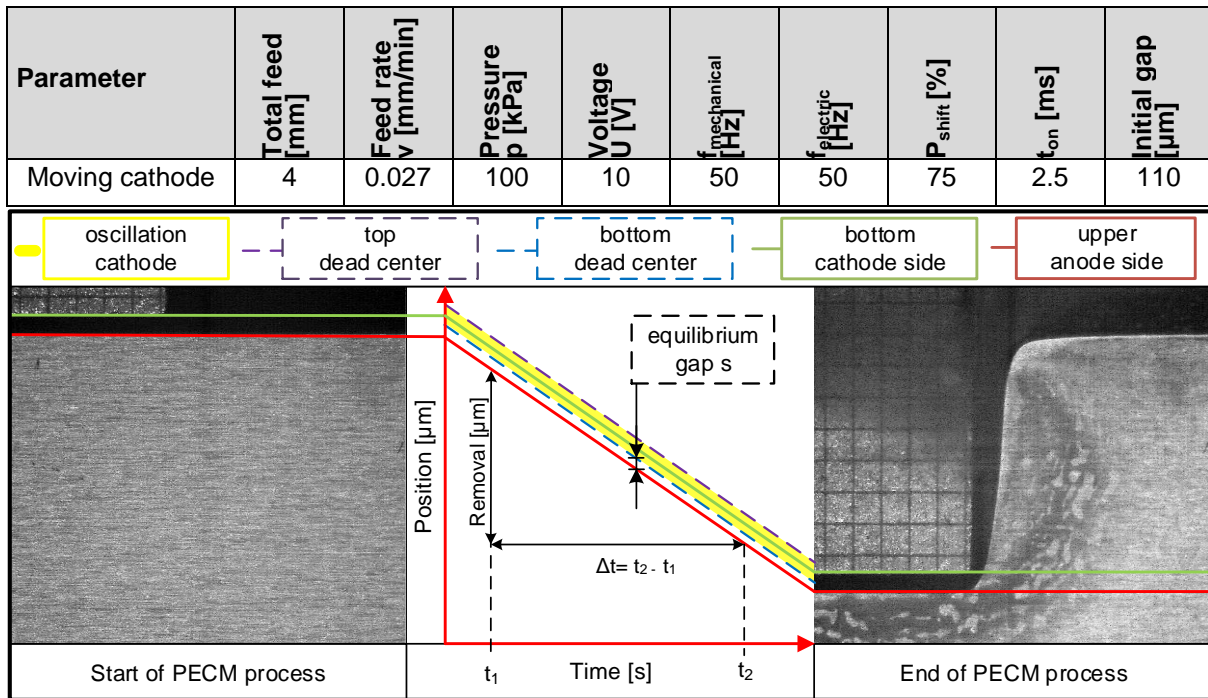


Figure 7-22 Verification of the feed rate used in the experiment and illustration of the oscillation and equilibrium frontal gap based on the acquired data

The experiments based on the observation of geometry and dimensional shaping can be reduced to the investigation of the side gap development over time. This is achieved using the method of only applying pulses under stationary cathode vibration. Such an experiment is presented in Figure 7-23. Using two rectangular shaped electrodes, with a frontal surface area of 1 x 30 mm<sup>2</sup> for the cathode, 1 x 29 mm<sup>2</sup> for the anode and the parameters provided, the software-based analysis covers multiple results at once. As separately explained in Figure 7-23, the basic analysis covers the tracing of the anode movement and the direct correlation of image information with the material removal in volume units as well as the comparison towards the prevailing process conditions at each point in time.

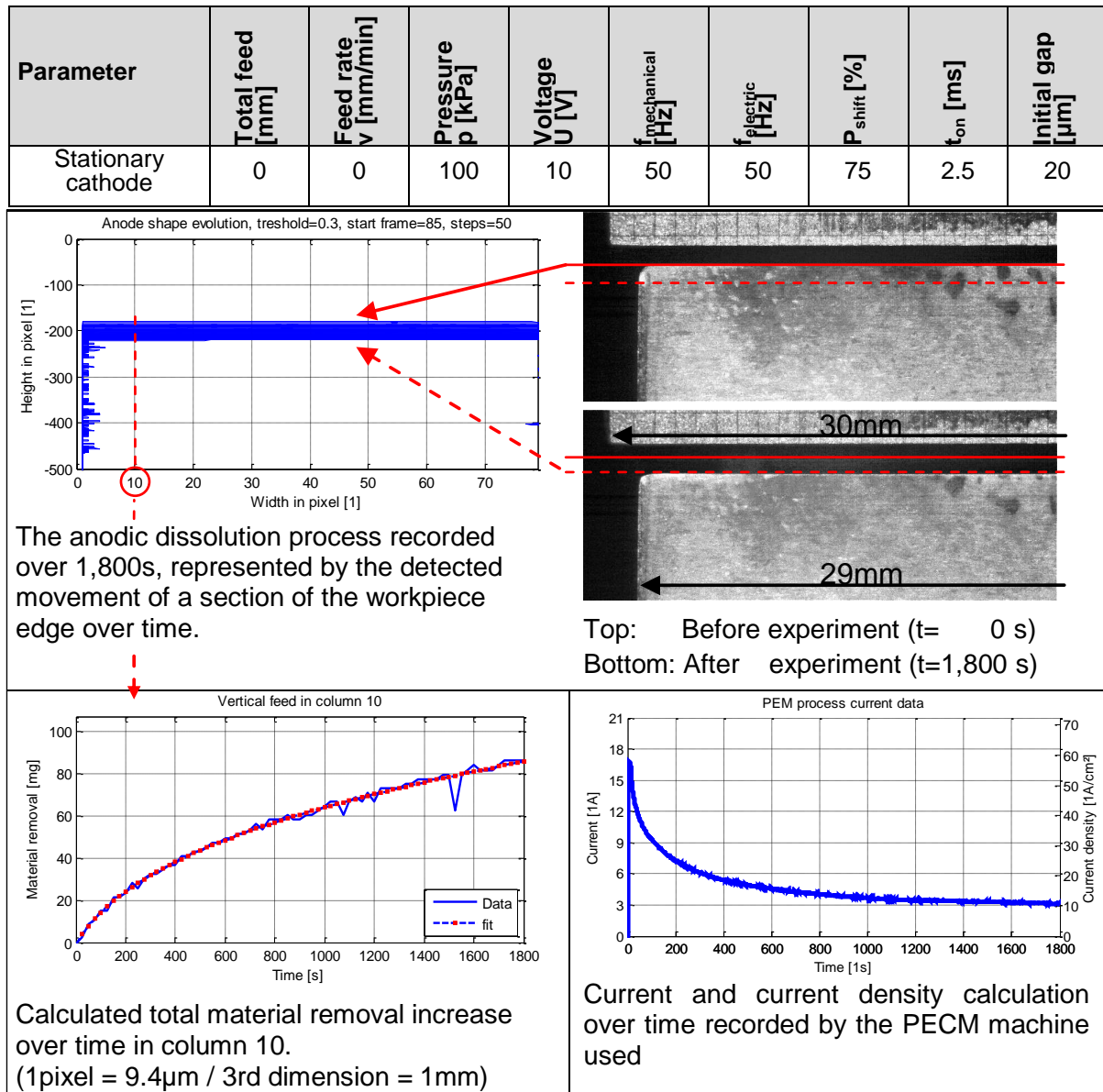


Figure 7-23 Direct extraction of material data from video data [88]

When using the same setup, side gap detections are also possible. Figure 7-24 schematically shows how a side gap detection and evaluation over time is possible at a constant, pre-defined detection layer. The detection layer is defined by a pre-set horizontal reference line beneath the initial anode surface. As indicated in the figure, the side gap detection starts once the depth of 0.5 mm is reached. Before this depth was reached through dissolution and shaping, no boundaries other than the global image boundaries can be detected using the programmed software. In further steps, the side gap distance on the pre-defined depth is continuously evaluated and can be traced using the representation of time in relation to the gap size.

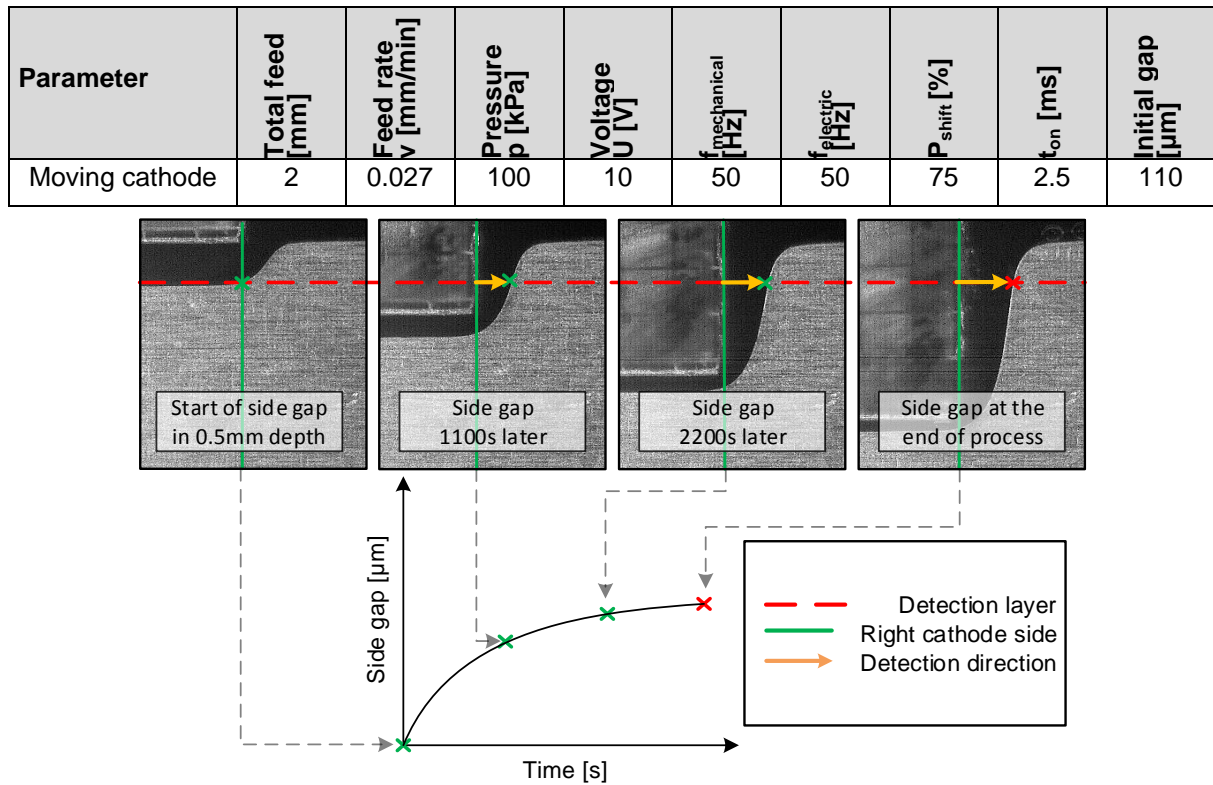


Figure 7-24 Side gap detection using software analysis

Figure 7-25 shows how the detection of the side gap can be used to visually trace a side gap on the inflow side and on the outflow side of the electrolyte. The information provided in the figure pictures the steps taken to gather the information about the varying side gap developments. While on the inflow side of the setup, indicated by the green line, the side gap widening follows the material behavior investigated for the material 1.4301, the gap widening on the outflow side, indicated by the red line, shows a divergent behavior. This effect could specifically be traced back to a different edge shape on the cathode. With this deviation in shape, the electrical field and therefore the resulting current density on the outflow side was different. The impact of such a deviation causes changes in the overall shaping process. Yet with the possibility to trace the geometry during the process, a direct link between the geometry, dissolution and boundary conditions can be created. In addition reasons for deviations can be traced back to their origins by looking at the effects on a time based approach.

Looking at the precision itself, with a pixel ratio of  $8.5 \mu\text{m}/\text{pixel}$ , the investigation method is not yet sufficient enough to qualitatively cover the complete range of precision offered by PECM. Yet, as part of this work, the setup itself already provides new insights into the shaping processes by taking into account the factor time. The possibilities and chances offered by such continuous investigations could be exploited in these investigations only partially. With improved equipment offering a more detailed optical imaging and by using higher frame rates, insights into the faster processes, like flushing, electrolyte flow and other observations should very well be possible.

Parameter	Total feed [mm]	Feed rate $v$ [mm/min]	Pressure $p$ [kPa]	Voltage $U$ [V]	$f_{\text{mechanical}}$ [Hz]	$f_{\text{electric}}$ [Hz]	$P_{\text{shift}}$ [%]	$t_{\text{on}}$ [ms]	Initial gap [ $\mu\text{m}$ ]
Moving cathode	2	0.027	100	10	50	50	75	2.5	110

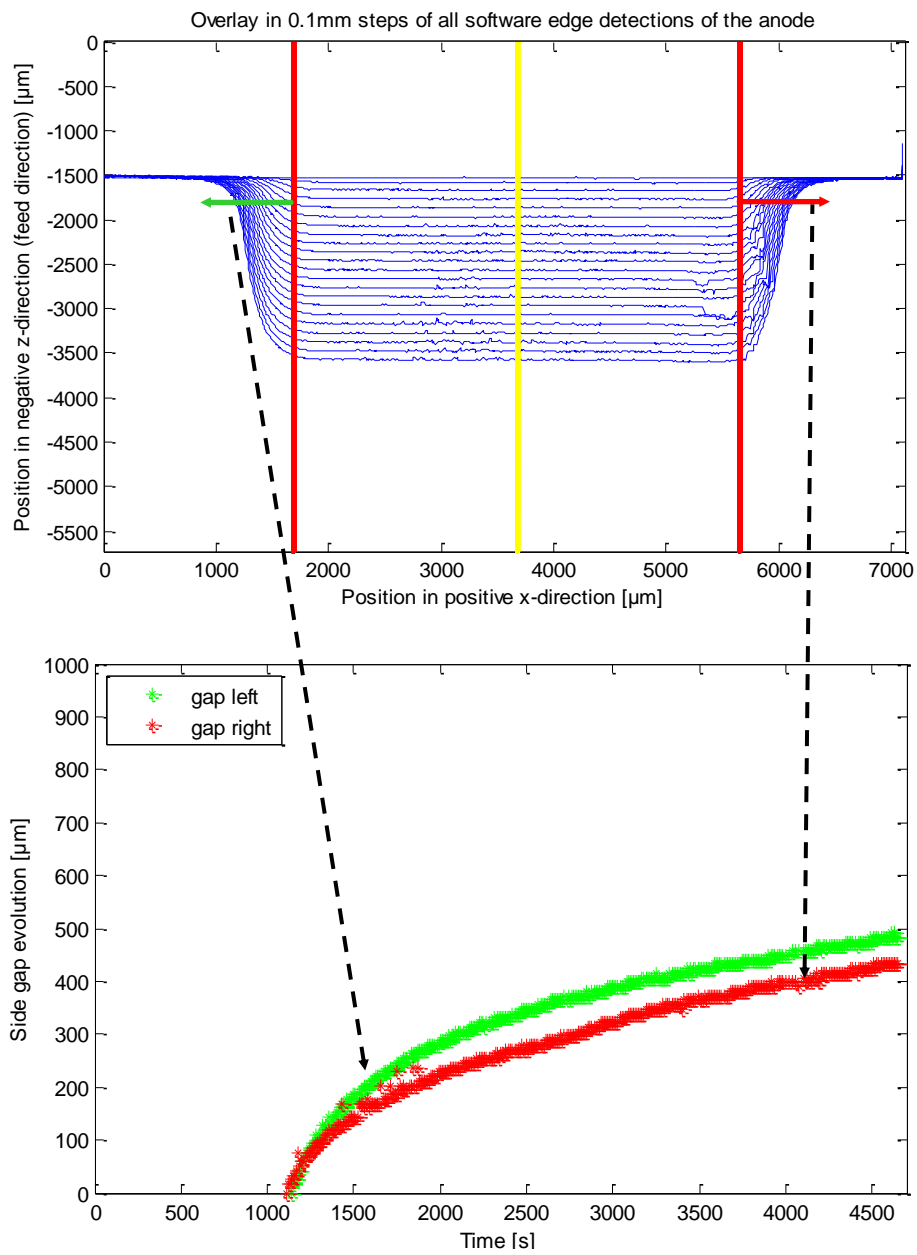
  


Figure 7-25 Side gap evolution 0.4 mm below the initial anodic surface as function over time based on video observation [88]

### 7.3 Simulation based on material-specific data

The simulation based on material-specific data is focused on the results derived from the experiments using the stainless steel material 1.4301. To validate the simulation introduced, a reference experiment was performed. Figure 7-26 presents the parameters and details of the experiment performed. The experimental boundary conditions under which the data for the simulation was determined are as follows:

- Electrolyte conductivity  $\sigma = 71 \text{ mS/cm } (\pm 0.5 \text{ mS/cm})$
- Temperature  $T = 21^\circ\text{C } (\pm 1^\circ\text{C})$
- pH  $7.1 \text{ pH } (\pm 0.2 \text{ pH})$

Based on this experiment, the geometry was captured from the frames recorded using the programmed edge detection algorithm in Matlab. The shape serves as the basis for comparison.

Parameter	Total feed [mm]	Feed rate $v$ [mm/min]	Pressure $p$ [kPa]	Voltage $U$ [V]	$f_{\text{mechanical}}$ [Hz]	$f_{\text{electric}}$ [Hz]	$P_{\text{shift}}$ [%]	$t_{\text{on}}$ [ms]	Initial gap [ $\mu\text{m}$ ]
Moving cathode	2	0.027	100	10	50	50	75	2.5	110

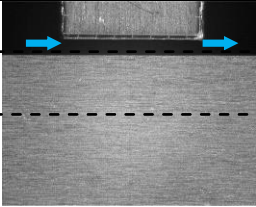
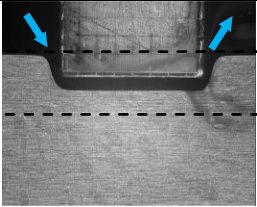
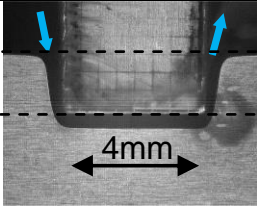
2 mm			
time	0 s	2,344 s	4,688 s

Figure 7-26 Experimental data for the validation of the introduced simulation

In order to use the data for simulation purposes, the individual points determined in the experiments have to be transformed into a continuous dataset. To improve the dataset before using the tanh approach, compare Table 7.4, the database needed to be enlarged. Originally just ranging between  $23.7 \text{ A/cm}^2$  to  $77.7 \text{ A/cm}^2$ , the data was enlarged performing additional experiments based on the experimental conditions mentioned for the continuous experiment. Figure 7-27 shows the data experimentally determined, ranging from  $8.1 \text{ A/cm}^2$  up to  $93.5 \text{ A/cm}^2$ .

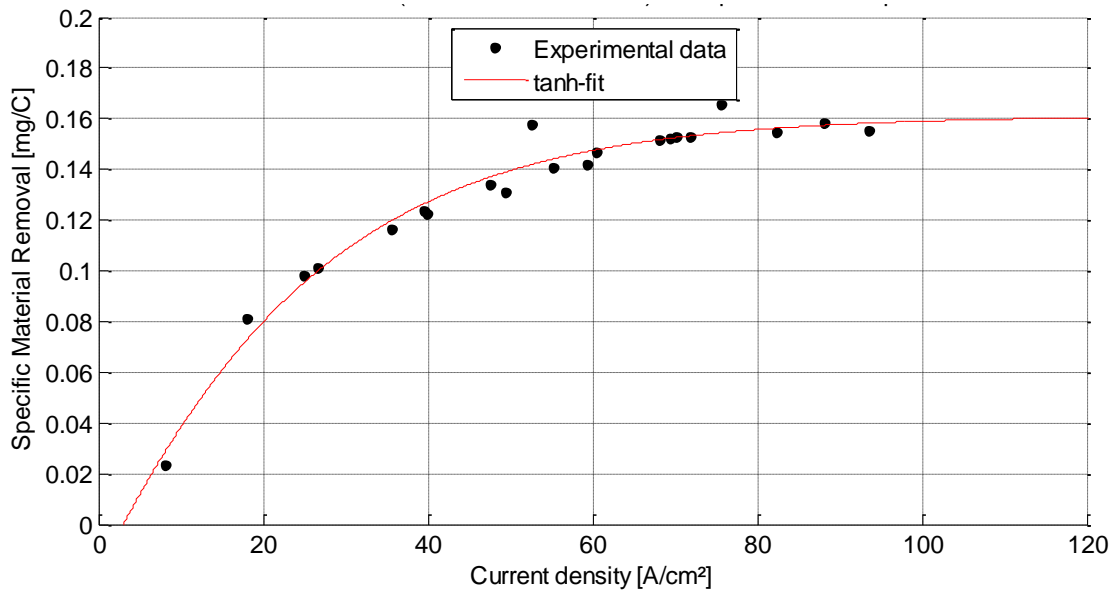


Figure 7-27 Material data for 1.4301 ( $U=10V$  and  $t_{on}=2.5ms$ )

Table 7.4 tanh-fit data under defined boundary conditions

$SMR_{1.4301; 10V; 2.5ms} = a \cdot (\tanh(b \cdot t_{on} + c) \cdot J + (d \cdot t_{on} \cdot e)) + f$			
$a = 6.4683 \frac{mg \cdot cm^2}{C \cdot A}$	$b = 0.6152 \frac{1}{s}$	$c = 0.795$	$d = 0.06 \frac{1}{s}$
$e = 0.4965$	$f = 0.0659 \frac{mg}{C}$	$R^2 = 0.9713$	

The simulation result based on the stainless steel 1.4301 material data is presented in Figure 7-28. The calculated anode geometry corresponds well with the experimental shape pictured in red. The experimental shape was slightly smoothed in the range of -1 mm to 1 mm in the figure, since the edge detection created minor artefacts at the frontal boundary of the anodic surface due to cloudiness in the PMMA plate of the setup.



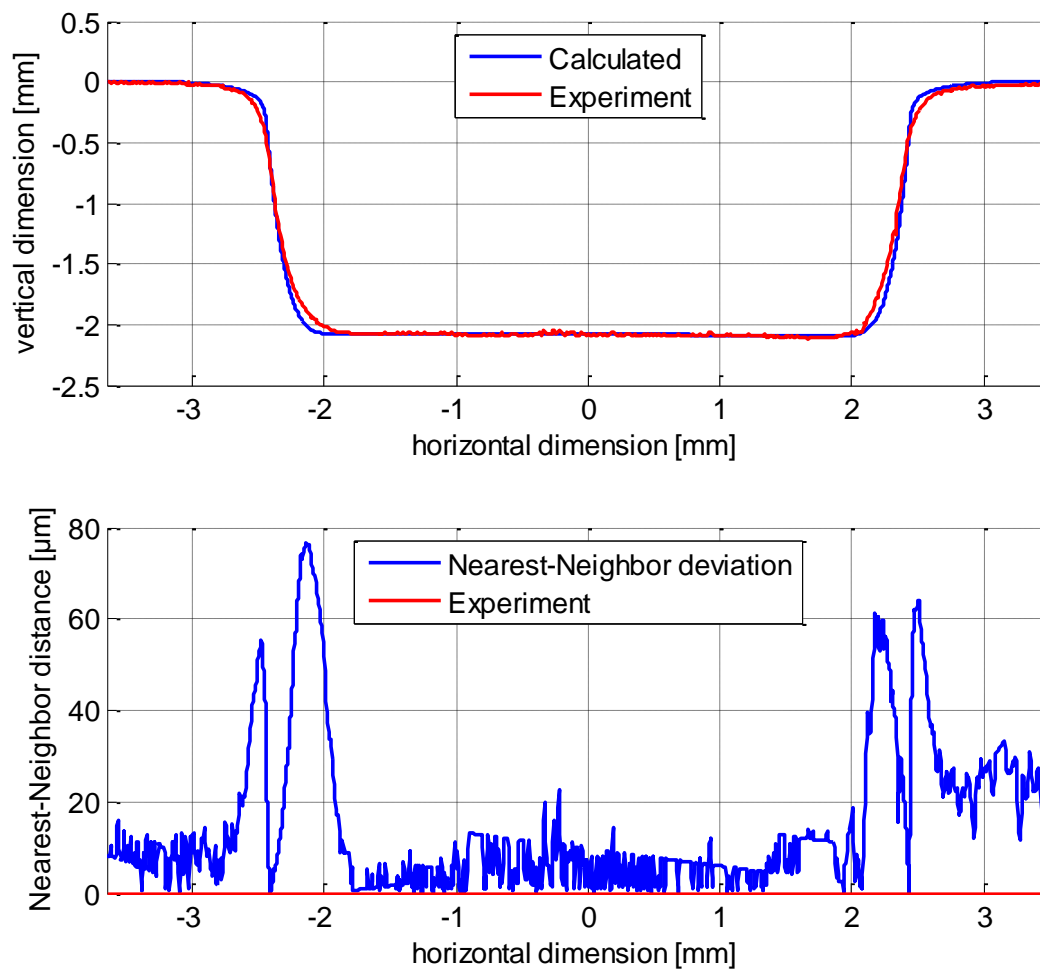


Figure 7-28 Calculated shape compared to the experimental contour

To estimate the precision of the simulation based on the material data, the calculated nearest-neighbor deviation is included in Figure 7-28. The calculation is based on the individual two-dimensional distances between the respectively closest points on anode and cathode. The greatest deviation, with a maximum value of 76.6  $\mu\text{m}$ , is in close vicinity to the cathode's frontal edges, where the electric field is at its maximum. Despite these deviations, the simulation itself proves to be robust and functional. The overall calculation time in the example was 521.25 seconds, simulating every fifth pulse. The subdivision of the anode was made at 5  $\mu\text{m}$  increments and the subdivision of the cathode at 10  $\mu\text{m}$  increments. By setting the simulation on the same hardware (Windows7SP1x64bit, AMD FX™-8120 Eight-Core processor (3.10GHz) and 8GB of RAM) to a time stepping of every hundredth pulse, the calculation time can be reduced to about 26.6 seconds with just slight differences in the result. Using this simulation, the process time can be estimated and the energy consumed can be calculated. This enables an estimation of the workload for the used machine and additionally the specification of a multiple electrode, parallel machining approach.

Table 7.5 Calculation data

Parameter	Total feed [mm]	Feed rate $v$ [mm/min]	Pressure $p$ [kPa]	Voltage $U$ [V]	$f^{\text{mechanical}}$ [Hz]	$f^{\text{electric}}$ [Hz]	$P_{\text{shift}}$ [%]	$t_{\text{on}}$ [ms]	Initial gap [ $\mu\text{m}$ ]
Moving cathode	2	0.13	-	10	50	50	75	2.5	40

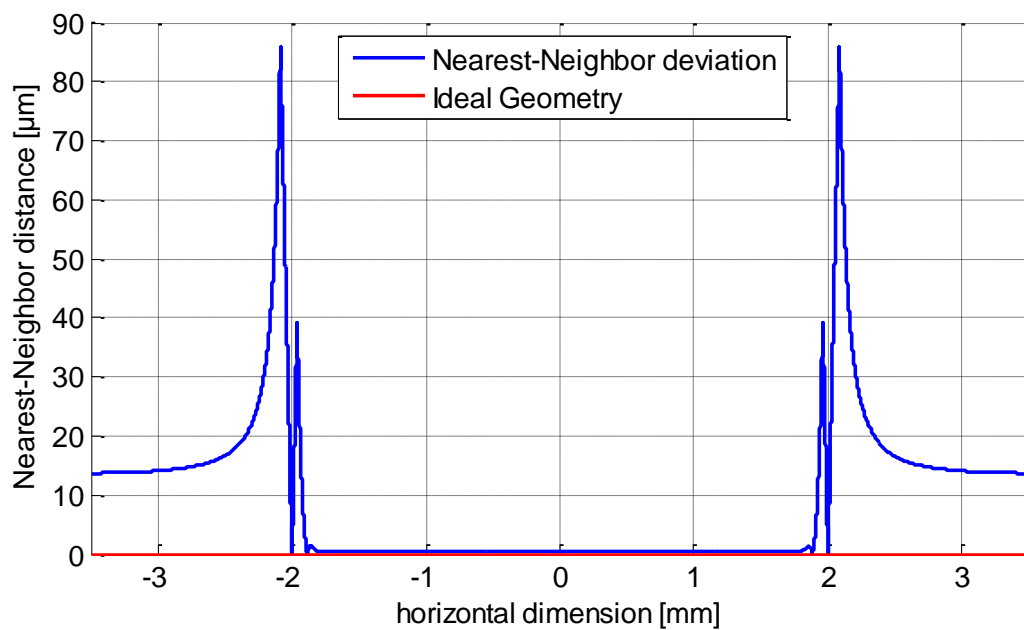
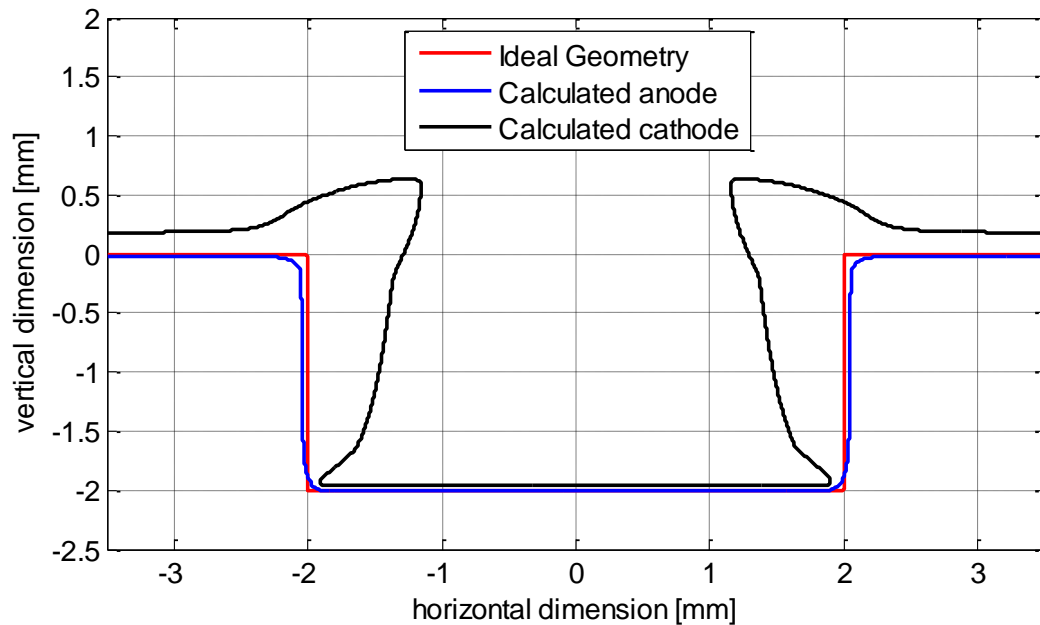


Figure 7-29 Inverse calculation of the cathode geometry

For the tool simulation, introduced in chapter 6.3, an ideal rectangular cavity was assumed. With an electrode segmentation of 5  $\mu\text{m}$  and simulating every tenth pulse, using the parameters listed in Table 7.5, the simulation took 14 iterations and a total time of 1,126.7 seconds to calculate the result pictured in Figure 7-29. The blue outline shows the simulated anode geometry in contrast to the intended ideally rectangular shape in red. The cathode theoretically needed to machine this cavity with a depth of 2 mm is outlined in black. The nearest-neighbor deviation between ideal anode and calculated anode calculates to a maximum deviation of 85.3  $\mu\text{m}$  at the transition edge from the initial surface into the gap. Even though this theoretical approach could not be validated, it contains the opportunity for a scientific and accelerated cathode design process based on material-specific dissolution data.



## 8 Summary and Conclusion

In the beginning of this work, the basics of the electrochemical dissolution and processing of material using the ECM production process are presented. Based on these principles and basic theory, the reference to the used PECM process and machine technology is emphasized. By introducing and utilizing specifically designed, yet easy-to-use experimental setups, the possibilities and necessary restrictions in the experimentation using the available PECM machining technology is presented. For the acquisition of material-specific data, three different experimental procedures are introduced:

1. Frontal gap experiments (steady-state) are the key to derive material-specific data under a wide range of boundary conditions. Yet in the focus of using industrial process conditions, the necessity for e.g. identical pre-machining before the actual experiment in order to eliminate the effects of preprocessing using other machining technologies is emphasized. With this proceed frontal gap and feed rate relationships, as well as surface roughness specifics from combinations of pulse on times and different current densities can be investigated.
2. Side gap experiments (steady-state) are useful to examine the relationship between current density and passivation, through the widening of the gap over time.
3. Continuous observations (dynamic over time) using a novel approach and setup are introduced and tested. They allow a view into the overall geometric shaping process while machining, and a variety of downstream data analysis possibilities.

During the restriction of parameters and the introduction of machine-specific boundary conditions for the gathering and recording of data, the theoretical aspects of the technology are substantiated and discussed using experimental data. Also the uncertainties are investigated and the individual limits towards the precision of each mechanical, electrical and visual method are discussed.

The material-specific data at hand, the datasets are reworked and then presented according to the basic principles of electrochemical dissolution. While the material composition cannot be influenced, the data is adapted to show the effects on shape and surface based on the process input parameters, which can be modified using the machine technology to achieve a desired result.

The focus is set on the investigation of two different materials, a commonly used stainless steel and a powder metallurgical steel. For a better understanding and transparency, most experiments and validations are presented based on one material, the stainless steel 1.4301, only. Here, the modelling and detailed explanation of relationships and occurring effects as well as special features are worked out. A standardized representation of material-specific data focused on geometry and surface at both stationary and dynamic conditions is presented.

Furthermore, a commonly assumed fact regarding the independence of the electrochemical process of the hardness of a material was substantiated with facts, showing the possibility of machining, but also the drastic differences in the results at the example of the powder metallurgical steel S390.

With the material data at hand, simulation possibilities derived from the process basics are presented with the aim of validating the simulation in reference to actual experimental data. The possibility to calculate and estimate geometries and shapes as a way of visualizing the complex technological relationships is made available. Using this mainly virtual tool (simulation) the development costs and process can be decreased.

Based on this standardized proceed and simulation possibility to reduce the process of iterative tool shaping, a machine control could be realized, which uses only the targeted depth and desired surface roughness as input parameters. As basis of this approach a material database or clusters of similar material compositions should be made available similar to the approach in the plastics and metal processing industry, where processing data is made available by the suppliers of the materials. The clustering of materials could be achieved in accordance with the chemical compositions as well with regard to the material's microstructure. With this knowledge at hand, the acceptance and use cases for the Electrochemical Machining might further increase, yet at the same time be of benefit for the further improvement of easy-to-use simulations as part of or additional packages for well-established CAD software.

## REFERENCES

- [1] C. Czeslik, H. Seemann and R. Winter: Basiswissen Physikalische Chemie. 4., aktualisierte Auflage, Vieweg+Teubner, Wiesbaden, 2010.
- [2] "Wikipedia," Wikimedia Foundation Inc., 2015. [Online]. Available: [https://en.wikipedia.org/wiki/Faraday%27s\\_laws\\_of\\_electrolysis](https://en.wikipedia.org/wiki/Faraday%27s_laws_of_electrolysis). [Accessed 11 July 2015].
- [3] Metcut Research Associates Inc.: Machining Data Handbook 3rd edition, Volume two. ISBN 0-936914-02-8, 1980.
- [4] R. Förster: Untersuchung des Potentials elektrochemischer Senkbearbeitung mit oszillierender Werkzeugelektrode für Strukturierungsaufgaben der Mikrosystemtechnik. Dissertation, Albert-Ludwigs-Universität Freiburg im Breisgau, Freiburg, 2004.
- [5] K. P. Rataj: Elektrochemische Charakterisierung technisch relevanter anodischer Oxidschichten bei niedrigen und höchsten Stromdichten. Dissertation, Heinrich-Heine-Universität Düsseldorf, Düsseldorf, 2013.
- [6] T. R. Munninghoff: Mechanismen der anodischen Auflösung von Metallen und Legierungen bei extrem hohen Stromdichten. Dissertation, Heinrich-Heine-Universität Düsseldorf, Düsseldorf, 2012.
- [7] F. Klocke and W. König: Fertigungsverfahren 3 - Abtragen, Generieren, Lasermaterialbearbeitung. 4.te, neu bearbeitete Auflage, Springer-Verlag Berlin Heidelberg, 2007.
- [8] H. S. J. Altena: EDM and ECM for mass production Philips DAP. *Journal of Materials Processing Technology* 149 (2004), pp.18-21, 2004.
- [9] F. Klocke, A. Klink, D. Veselovac, D. K. Aspinwall, S. L. Soo, M. Schmidt, J. Schilp, G. Levy, J.-P. Kruth: Turbomachinery component manufacture by application of electrochemical, electro-physical and photonic processes. *CIRP Annals - Manufacturing Technology* 63 (2014), pp.703-726, 2014.
- [10] D. R. Corbin: Corbin Handbook of Bullet Swaging No. 9. White City, OR 97503 USA: Corbin Manufacturing & Supply, Inc., 2012.
- [11] H. Degenhardt: Elektrochemische Senkbarkeit metallischer Werkstoffe. Dissertation, Rheinisch-Westfälische Technische Hochschule Aachen, Aachen, 1972.

- [12] M. Brussee: PECM History and Outlook. *International Symposium on Electrochemical Machining INSECT2011*, Editors: B. Mollay, M.M. Lohrengel, pp.8-9, Vienna, 2011.
- [13] ECM, LLC: Short history of electrochemical machining (ECM) development. <http://www.indec-ecm.com/en/>, online: 12.12.2014.
- [14] W. Piersig: ECM - Elektrochemische Metallbearbeitung und EC-Kombinationsverfahren. GRIN Verlag, ISBN 978-3-640-19833-7, 2008.
- [15] K. P. Rajurkar, M. Sundaram, A. P. Malshe: Review of Electrochemical and Electrodischarge Machining. *Procedia CIRP 6 (2013)*, pp.13-26, 2013.
- [16] DIN 8580: Fertigungsverfahren; Begriffe, Einteilung. DIN 8580:2003-09, Beuth Verlag, Berlin, 2003.
- [17] DIN 8590: Fertigungsverfahren Abtragen; Einordnung, Unterteilung, Begriffe. DIN8590:2003-09, Beuth Verlag, Berlin, 2003.
- [18] VDI 3400: Elektroerosive Bearbeitung; Begriffe, Verfahren, Anwendung. VDI-Handbuch Betriebstechnik, 1975.
- [19] VDI 3401 - Blatt 1 Entwurf: Elektrochemisches Abtragen; Formabtragen. VDI-Handbuch Betriebstechnik, Teil 2: Fertigungsverfahren, Düsseldorf, 2009.
- [20] VDI 3401 - Blatt 1: Elektrochemisches Abtragen; Formabtragen. VDI-Handbuch Betriebstechnik, Teil 2, Düsseldorf, 1993.
- [21] VDI 3401 - Blatt 3: Elektrochemisches Abtragen; Behandlung der Elektrolytlösungen, Abwässer und Schlämme. VDI-Handbuch Betriebstechnik, Teil 2, Düsseldorf, 1993.
- [22] A. E. DeBarr and D. A. Oliver: *Electrochemical Machining*. MacDonald, London, 1968.
- [23] D. Pahl: Über die Abbildungsgenauigkeit beim elektrochemischen Senken. Dissertation, Rheinisch-Westfälische Technische Hochschule Aachen, Aachen, 1969.
- [24] F. W. Wilson: *Practice and Theory of Electrochemical Machining*. John Wiley & Sons Inc., 1971.
- [25] W. Mauz: Technik der elektrochemischen Metallbearbeitung. *Chemie-Ing.-Techn.*, Vol. 45 (1973), Nr. 4, pp.194-197, 1973.
- [26] S. P. Loutrel, N. H. Cook: A Theoretical Model of High Rate Electrochemical Machining. *Journal of Engineering for Industry*, Paper No.73-Prod-2, pp.1003-



- 1008, 1973.
- [27] H. Dietz, K. G. Günther, K. Otto: Reproduction Accuracy with Electrochemical Machining: Determination of the Side Gap. *Annals of CIRP*, 22/1, pp.61-62, 1973.
- [28] J. A. McGeough: Principles of Electrochemical Machining. Chapman and Hall, London, 1974.
- [29] J. Bannard: Electrochemical machining. *Journal of Applied Electrochemistry*, 7, pp.1-29, 1976.
- [30] W. Degener: Handbuch Feinbearbeitung. VEB Verlag Technik, Berlin, 1979.
- [31] W. Degner: Elektrochemische Metallbearbeitung. VEB Verlag Technik, Berlin, 1984.
- [32] E. J. Weller and M. Haavisto: Nontraditional Machining Processes. Second Edition, Society of Manufacturing Engineers, 1984.
- [33] J. M. Fitz-Gerald, J. A. McGeough: Mathematical Theory of Electrochemical Machining 1. Anodic Smoothing. *J. Inst. Maths Applies (1969) 5*, pp.387-408, 1969.
- [34] J. M. Fitz-Gerald, J. A. McGeough, L. M. Marsh: Mathematical Theory of Electrochemical Machining 2. Anodic Shaping. *J. Inst. Maths Applies (1969) 5*, pp.409-421, 1969.
- [35] J. M. Fitz-Gerald, J. A. McGeough: Mathematical Theory of Electrochemical Machining 3. Deburring and Cavity-forming. *J. Inst. Maths Applies (1970) 6*, pp.102-110, 1970.
- [36] D. G. Risko, A. D. Davydov: Manufacturing applications and productivity limitations of electrochemical machining. *Manufacturing Science and Engineering ASME 1993*, PED-Vol. 64, pp.701-718, 1993.
- [37] K. P. Rajurkar, D. Zhu, J. A. McGeough, J. Kozak, A. De Silva: New Developments in Electro-Chemical Machining. *Annals of CIRP*, Vol. 48/2, pp.567-579, 1999.
- [38] W. König: Elektrochemisches Abtragen. In: G. Spur, T. Stöferle: Handbuch der Fertigungsverfahren Band 4/1 Abtragen, Beschichten. München Wien: Carl Hanser Verlag, 1987.
- [39] J. Wijers: Sterke evolutie elektrochemisch. *Mikroniek 2-2009*, pp.36-42, 2009.

- [40] T. Masuzawa, T. Takawashi: Recent Trends in EDM/ECM Technologies in Japan. *VDI Berichte Nr. 1405*, pp.1-15, 1998.
- [41] H.-P. Lindenlauf: Werkstoff- und elektrolytspezifische Einflüsse auf die Elektrochemische Senkbarkeit ausgewählter Stähle und Nickellegierungen. Dissertation, Rheinisch-Westfälische Technische Hochschule Aachen, Aachen, 1977.
- [42] C. H. Hamann and W. Vielstich: Elektrochemie. 4., vollständig überarbeitete und aktualisierte Auflage, Wiley-VCH, 2005.
- [43] G. M. Alder, D. Clifton, F. Mill: A direct analytical solution to the tool design problem in electrochemical machining under steady state conditions. *Proceedings of the Institution of Mechanical Engineers, Part B: Journal of Engineering Manufacture*, vol. 214, pp.745-750, 2000.
- [44] H. S. J. Altena: Precision ECM by process characteristic modelling. Dissertation, Glasgow Caledonian University, 2000.
- [45] S. Hinduja, M. Kunieda: Modelling of ECM and EDM processes. *CIRP Annals - Manufacturing Technology*, Vol. 62 (2013), pp.775–797, 2013.
- [46] J. W. Schultze, M. M. Lohrengel: Stability, reactivity and breakdown of passive films. Problems of recent and future research. *Electrochimica Acta 45 (2000)*, pp.2499-2513, 2000.
- [47] C. Rosenkranz, M. M. Lohrengel, J. W. Schultze: The surface structure during pulsed ECM of iron in NaNO<sub>3</sub>. *Electrochimica Acta 50 (2005)*, pp.2009-2016, 2005.
- [48] C. Rosenkranz: Elektrochemische Prozesse an Eisenoberflächen bei extremen anodische Stromdichten. Dissertation, Heinrich-Heine-Universität Düsseldorf, Düsseldorf, 2005.
- [49] M. M. Lohrengel, C. Rosenkranz: Microelectrochemical surface and product investigations during electrochemical machining (ECM) in NaNO<sub>3</sub>. *Corrosion Science*, 47, pp.785-794, 2005.
- [50] A. Möhring: Entwicklung einer elektrochemischen Mikrodurchflusszelle zur Untersuchung des Elektrochemischen Senkens (ECM, Electrochemical Machining). Dissertation, Heinrich-Heine-Universität Düsseldorf, Düsseldorf, 2004.
- [51] W. Pies, A. Weiss: a2215, I.2.1 Simple chlorides and their solid solutions. *SpringerMaterials - The Landolt-Börnstein Database* (<http://www.springermaterials.com>), DOI: 10.1007/10201462\_30.

- [52] K. Gesi: 30A-2 KNO<sub>3</sub> [F]. *SpringerMaterials - The Landolt-Börnstein Database* (<http://www.springermaterials.com>), DOI: 10.1007/10635019\_58.
- [53] M. Datta, D. Landolt: On the role of mass transport in high rate dissolution of iron and nickel in ECM electrolytes - I. chloride solutions. *Electrochimica Acta*, Vol. 25, pp.1255-1262, 1980.
- [54] M. Datta, D. Landolt: On the role of mass transport in high rate dissolution of iron and nickel in ECM electrolytes - II. chlorate and nitrate solutions. *Electrochimica Acta*, Vol. 25, pp.1263-1271, 1980.
- [55] Kirsch Pharma GmbH: Sicherheitsdatenblatt nach 91/155/EWG - Handelsname: Natriumnitrat, Material-Nr.: 10318. Ausgabedatum: 29.06.2007, 2007.
- [56] A. K. M. De Silva, H. S. J. Altena, J. A. McGeough: Influence of Electrolyte Concentration on Copying Accuracy of Precision-ECM. *Annals of CIRP*, 52/1, pp.165-168, 2003.
- [57] D. Bähre, A. Rebschläger, O. Weber, P. Steuer: Reproducible, fast and adjustable surface roughening of stainless steel using Pulse Electrochemical Machining. *Procedia CIRP 6 (2013)*, pp.385-390, 2013.
- [58] A. P. Semaschko, N. Z. Gimaev, I. V. Maksimov, S. V. Bezrukov, V. B. Rabinovitch: Verfahren und Anordnung zur elektrochemischen Bearbeitung. *Deutsches Patentamt*, Offenlegungsschrift DE 29 03 873 A1, 1979.
- [59] M. Datta, D. Landolt: Electrochemical Machining under pulsed current conditions. *Electrochimica Acta Band 26 (1981)*, pp.899-907, 1981.
- [60] M. Datta, D. Landolt: Electrochemical saw using pulsating voltage. *Journal of Applied Electrochemical 13 (1983)*, pp.795-802, 1983.
- [61] J. Kozak, K. P. Rajurkar, B. Wei: Analysis of electrochemical machining process with short pulses. *Materials Issues in Machining and the Physics of Machining Processes*, pp.131-146, 1992.
- [62] J. Kozak, K. P. Rajurkar, Z. Gulbinowicz: Electrochemical machining with using of vibrating tool electrode. *International Symposium on Electrochemical Machining INSECT2009*, Editors: A. Michaelis, M. Schneider, pp. 31-36, 2009.
- [63] J. Kozak, K. P. Rajurkar, S. Malicki: Study of electrochemical machining utilizing a vibrating tool electrode. *16th International Conference on Computer-aided Production Engineering CAPE 2000*, IMechE Conference Transactions 2000-5, pp.173-181, 2000.

- [64] H.-P. Schulze: Problems of the processing accuracy for electro-erosion and electro-chemical machining processes. *International Journal of Material Forming*, Vol. 2 Suppl. 1, pp.641-644, 2009.
- [65] S. Moser: Mikrostrukturierung von Metallen durch elektrochemischen Abtrag mit gepulstem Strom (PECM). Dissertation, Heinrich-Heine-Universität Düsseldorf, Düsseldorf, 2004.
- [66] B. Lilly, J. Brevick, C. S. Chen: The effect of pulsed electrochemical machining on the fatigue life of H-13 steel. *Transactions of NAMRI/SME*, Volume XXV, 153-158, 1997.
- [67] K. P. Rajurkar, J. Kozak, B. Wei: Study of Pulse Electrochemical Machining Characteristics. *Annals of CIRP*, 41/1, pp.231-234, 1993.
- [68] M. Burger: Präzise Elektrochemische Bearbeitung (PECM) komplexer Strukturbauteile. Dissertation, Technische Universität München, München, 2010.
- [69] J. Kozak: Thermal models of pulse electrochemical machining. *Bulletin of the polish academy of sciences*, Technical Sciences Vol. 52, No. 4, pp.313-320, 2004.
- [70] A. D. Davydov, V. M. Volgin, V. V. Lyubimov: Electrochemical Machining of Metals: Fundamentals of Electrochemical Shaping. *Russian Journal of Electrochemistry*, Vol. 40, No. 12, pp.1230-1265, 2004.
- [71] A. Zaytsev, I. Agafonov, N. Gimaev, R. Moukhoutdinov, A. Belogorsky: Precise pulse electrochemical machining by bipolar current Aspects of effective technological application. *Journal of Materials Processing Technology 149 (2004)*, pp.419-425, 2004.
- [72] A. Zaitsev, N. Z. Gimaev, N. A. Amirchanova, A. L. Belogorsky, L. Markelova, R. R. Muchutdinov, M. Brussee: METHOD FOR A REMOVAL OF CATHODE DEPOSITIONS BY MEANS OF BIPOLAR PULSES. *United States Patent*, Patent No.: US 6,620,307 B2, 2003.
- [73] E. Rosset, M. Datta, D. Landolt: Electrochemical dissolution of stainless steels in flow channel cells with and without photoresist masks. *Journal of Applied Electrochemistry*, 20 (1990), pp.69-76, 1990.
- [74] G. Meichsner, L. Boenig, M. Hackert-Oschätzchen, M. P. T. Krönert, J. Edelmann, A. Schubert: Determination of the gas generation during precise electrochemical machining. *International Symposium on Electrochemical Machining Technology INSECT2014*, Editors: D. Bähre, A. Rebschläger, pp.63-75, Saarbrücken, 2014.

- [75] W. Hoogsteeen, T. P. Pajak: ECM Experiments on Stainless Steels. *International Symposium on Electrochemical Machining Technology INSECT2010*, Editors: J. Deconinck, D. De Wilde, pp.51-65, Brussels, 2010.
- [76] M. Spittel, T. Spittel: Steel symbol/number: X5CrNi18–10/1.4301. *SpringerMaterials - The Landolt-Börnstein Database* (<http://www.springermaterials.com>), Springer-Verlag Berlin Heidelberg, DOI: 10.1007/978-3-540-44760-3\_93, 2009.
- [77] W. Schatt, K.-P. Wieters and B. Kieback: Pulvermetallurgie; Technologien und Werkstoffe. 2., bearbeitete und erweiterte Auflage, Springer-Verlag, Berlin-Heidelberg, 2007.
- [78] Böhler Edelstahl GmbH: Böhler S390 microclean. Material Data Sheet: <http://www.boehler-edelstahl.com/english/files/S390DE.pdf> (online 01/21/2015).
- [79] W. Hoogsteen: The effect of the heat treatment of an ASTM A693 stainless steel on the ECM behavior in NaNO<sub>3</sub> and NaNO<sub>2</sub> electrolyte. *International Symposium on Electrochemical Machining Technology INSECT2014*, Editors: D. Bähre, A. Rebschläger, pp.77-84, Saarbrücken, 2014.
- [80] A. Schubert, G. Meichsner, M. Hackert-Oschätzchen, M. Zinecker, J. Edelmann: Pulsed Electrochemical Machining of Powder Metallurgy Steels. *International Symposium on Electrochemical Machining INSECT2011*, Editors: B. Mollay, M.M. Lohrengel, pp.68-75, Vienna, 2011.
- [81] Bio-Logic Science Instruments SAS, EC-Lab Software User's Manual. Version 10.38, 2014.
- [82] H. S. J. Altena: EDM and ECM for mass production Philips DAP. *Journal of Materials Processing Technology* 149 (2004), pp.18-21, 2004.
- [83] M. Hackert-Oschätzchen, M. Penzel, M. Kowalick, G. Meichsner, A. Schubert: Transient Simulation of the Electrolyte Flow in a Closed Device for Precise Electrochemical Machining. *Proceedings of the 2014 COMSOL Conference in Cambridge*, Cambridge, 2014.
- [84] A. Schubert, G. Meichsner, L. Boenig, M. Hacker-Oschätzchen, M. Krönert, J. Edelmann: Resource-Efficient Design of Precise Electrochemical Machining. *International Symposium on Electrochemical Machining Technology INSECT2013*, Editors: A. Schubert, M. Hackert-Oschätzchen, pp.53-63, Chemnitz, 2013.
- [85] P. Steuer, A. Rebschläger, A. Ernst, D. Bähre: Process Design in Pulse Electrochemical Machining Based on Material Specific Data – 1.4301 and Electrolytic Copper as an Example. *Key Engineering Materials Vols 651-653*,

- pp. 732-737, 2015.
- [86] C.-O. A. Olsson, D. Landolt: Passive films on stainless steels - chemistry, structure and growth. *Electrochimica Acta* 48 (2003), pp.1093-1104, 2003.
- [87] A. Rebschläger, R. Kollmannsperger, D. Bähre: Video based process observations of the pulse electrochemical machining process at high current densities and small gaps. *Procedia CIRP* 13 (2013), pp. 418-423, 2013.
- [88] A. Rebschläger, K. U. Fink, T. Heib, D. Bähre: Geometric shaping analysis based on PECM video process observations. *International Symposium on Electrochemical Machining Technology INSECT2014*, Editors: D. Bähre, A. Rebschläger, pp.37-44, Saarbrücken, 2014.
- [89] C. Y. Yu, Y. H. Liu, Y. H. Huang, Y. C. Hsu: The Investigation of the Flow Characteristics of the Gap in the Pulse Electrochemical Machining (PECM). *Annals of CIRP*, 31/1, pp.119-123, 1982.
- [90] M. Schneider, S. Schroth, N. Schubert, C. Lämmel, A. Michaelis: A novel approach of in-situ investigation of the surface topography under near ECM-conditions. *International Symposium on Electrochemical Machining INSECT2009*, Editors: A. Michaelis, M. Schneider, pp.81-87, 2009.
- [91] M. Schneider, S. Schroth, S. Richter, S. Höhn, N. Schubert, A. Michaelis: In-situ investigation of the interplay between microstructure and anodic copper dissolution under near-ECM conditions – Part 1: The active state. *Electrochimica Acta* 56 (2011), pp.7628-7636, 2011.
- [92] M. Schneider, S. Schroth, S. Richter, S. Höhn, N. Schubert, A. Michaelis: In-situ investigation of the interplay between microstructure and anodic copper dissolution under near-ECM conditions – Part 2: The transpassive state. *Electrochimica Acta* 70 (2012), pp.76-83, 2012.
- [93] S. Schroth: Optische In-situ-Beobachtung des anodischen Auflösungsverhaltens von Kupfer unter ECM-nahen Bedingungen. FRAUNHOFER VERLAG, Dresden, 2013.
- [94] F. Klocke, M. Zeis, T. Herrig, S. Harst, A. Klink: Optical In Situ Measurements and Interdisciplinary Modeling of the Electrochemical Sinking Process of Inconel 718. *Procedia CIRP* 24 (2014), pp.114-119, 2014.
- [95] A. Rebschläger, O. Weber, B. Heitkamp: Benefits and Drawbacks Using Plastic Materials Produced by Additive Manufacturing Technologies in the Electrochemical Environment. *International Symposium on Electrochemical Machining Technology INSECT2013*, Editors: A. Schubert, M. Hackert-Oschätzchen, pp.45-51, Chemnitz, 2013.

- [96] S. Agafonov, M. Brussee, J. Dorzweiler: The influence of pressure and flow on the results of the PEM process. *n.a.*
- [97] A. N. Zaytsev, V. P. Zhitnikov, T. V. Kosarev: Formation mechanism and elimination of the workpiece surface macro-defects, aligned along the electrolyte stream at electrochemical machining. *Journal of Materials Processing Technology 149 (2004)*, pp.439-444, 2004.
- [98] K. Kollmannsperger, "Softwaregestützte Analyse des elektrochemischen Materialverhaltens eines Edeltstahls auf Basis experimentell erfasster Video- und Bilddaten," Master Thesis, Saarland University, Saarbrücken, 2014.
- [99] K. U. Fink, "Analyse der geometrischen Formgebung des gepulsten elektrochemischen Abtragens auf Basis experimentell erfasster Video- und Bilddaten," Master Thesis, Saarland University, Saarbrücken, 2014.
- [100] A. Rebschläger, O. Weber, D. Bähre: In-situ process measurements for industrial size Pulse Electrochemical Machining. *International Symposium on Electrochemical Machining Technology INSECT2012*, Editor: Maria Zybura-Skrabalak, pp.133-148, Krakow, 2012.
- [101] M. Datta, D. Landolt: On the influence of electrolyte concentration, pH and temperature on surface brightening of nickel under ECM conditions. *Journal of Applied Electrochemistry 7 (1977)*, pp.247-252, 1977.
- [102] D. Landolt: Fundamental aspects of electropolishing. *Electrochimia Acta*, vol. 52 No. 1, pp.1-11, 1987.
- [103] M. Zybura-Skrabalak, A. Ruszaj: The influence of electrode surface geometrical structure on electrochemical smoothing process. *Journal of Materials Processing Technology 107 (2000)*, pp. 288-292, 2000.
- [104] DIN 4760: Gestaltabweichungen; Begriffe, Ordnungssystem. Beuth-Verlag, Berlin, 1992.
- [105] DIN EN ISO 4287: Geometrische Produktspezifikation (GPS) - Oberflächenbeschaffenheit: Tastschnittverfahren - Benennungen, Definitionen und Kenngrößen der Oberflächenbeschaffenheit. DIN EN ISO 4287:2010-07, Beuth Verlag, Berlin, 2010.
- [106] DIN EN ISO 4288: Geometrische Produktspezifikationen (GPS) - Oberflächenbeschaffenheit: Tastschnittverfahren Regeln und Verfahren für die Beurteilung der Oberflächenbeschaffenheit. EN ISO 4288 : 1997, Beuth Verlag, Berlin, 1998.
- [107] VDI/VDE 2602: Rauheitsmessung mit elektrischen Tastschnittgeräten.

- VDI/VDE-Handbuch Meßtechnik II, 1983.
- [108] W. König, H.-J. Hümbts: Mathematical Model for the Calculation of the Contour of the Anode in Electrochemical Machining. *Annals of CIRP*, 25/1, pp.83-87, 1977.
- [109] V. M. Volgin, A. D. Davydov: Modeling of multistage electrochemical shaping. *Journal of Materials Processing Technology 149 (2004)*, pp.466-471, 2004.
- [110] J. Kozak, K. Lubkowski, J. Peronczyk: Accuracy problems of the pulse electrochemical machining. *Proceedings of the International Machine Tool Design and Research Conference*, Issue of 1981, pp. 353-360, 1981.
- [111] K. P. Rajurkar, D. Zhu, B. Wei: Minimization of Machining Allowance in Electrochemical Machining. *Annals of CIRP*, 47/1, pp.165-168, 1998.
- [112] C. Van Osenbruggen, I. C. De Regt: Elektrochemisch micro-bewerken. Mikroniek 5-1988, Philips Technisch Tijdschrift 42-1984, 1984.
- [113] B. Mollay, G. Schöllhammer, P. Raffelstetter: A modeling strategy for the optimization of high-precision electrochemical machining processes. *International Symposium on Electrochemical Machining INSECT2009*, Editors: A. Michaelis, M. Schneider, pp.17-22, 2009.
- [114] A. K. M. De Silva, H. S. J. Altena, J. A. McGeough: Precision ECM by Process Characteristic Modelling. *Annals of CIRP*, 49/1, pp.151-155, 2000.
- [115] S. Van Damme, G. Nelissen, B. Van Den Bossche, J. Deconinck: Numerical model for predicting the efficiency behaviour during pulsed electrochemical machining of steel in NaNO<sub>3</sub>. *Journal of Applied Electrochemistry (2006) 36*, pp.1-10, 2006.
- [116] H. Hocheng, Y. H. Sun, P. S. Kao: A material removal analysis of electrochemical machining using flat-end cathode. *Journal of Materials Processing Technology 140 (2003)*, pp.264-268, 2003.
- [117] J. Kozak: Mathematical models for computer simulation of electrochemical machining processes. *Journal of Materials Processing Technology 76 (1998)*, pp.170-175, 1998.
- [118] J. Kozak, M. Chuchro, A. Ruszaj, K. Karbowski: The computer aided simulation of electrochemical process with universal spherical electrodes when machining sculptured surfaces. *Journal of Materials Processing Technology 107 (2000)*, pp.283-287, 2000.
- [119] J. Kozak, L. Dabrowski, K. Lubkowski, M. Rozenek, R. Slawinski: CAE-ECM



- system for electrochemical technology of parts and tools. *Journal of Materials Processing Technology* 107 (2000), pp.293-299, 2000.
- [120] J. Kozak: Computer Simulation of Electrochemical Machining. *Proceedings of the World Congress on Engineering and Computer Science WCECS 2011 Vol. II*, ISBN: 978-988-19251-7-6, San Francisco, 2011.
- [121] J. Kozak, D. Gulbinowicz, Z. Gulbinowicz: The Mathematical Modeling and Computer Simulation of Pulse Electrochemical Micromachining. *Engineering Letter*, 16:4, 2008.
- [122] P. Domanowski, J. Kozak: Direct and inverse problems of shaping by electrochemical generating machining. *Journal of Materials Processing Technology* 107 (2000), pp.300-306, 2000.
- [123] M. Purcar, L. Bortels, B. Van den Bossche, J. Deconinck: 3D electrochemical machining computer simulations. *Journal of Materials Processing Technology* 149 (2004), pp.472-478, 2004.
- [124] M. Purcar, A. Dorochenko, L. Bortels, J. Deconinck, B. Van den Bossche: Advanced CAD integrated approach for 3D electrochemical machining simulations. *Journal of Materials Processing Technology* 203 (2008), pp.58-71, 2008.
- [125] L. Bortels, M. Purcar, B. Van den Bossche, J. Deconinck: A user-friendly simulation software tool for 3D ECM. *Journal of Materials Processing Technology* 149 (2004), pp.486-492, 2004.
- [126] N. Smets, S. Van Damme, D. De Wilde, G. Weyns, J. Deconinck: Time averaged temperature calculations in pulse electrochemical machining. Part I: theoretical basis. *Journal of Applied Electrochemistry* (2007) 37, pp.1345-1355, 2007.
- [127] N. Smets, S. Van Damme, D. De Wilde, G. Weyns, J. Deconinck: Time averaged temperature calculations in pulse electrochemical machining, part II: numerical simulation. *Journal of Applied Electrochemistry* (2008) 38, pp.551-560, 2008.
- [128] N. Smets, S. Van Damme, D. De Wilde, G. Weyns, J. Deconinck: Calculation of temperature transients in pulse electrochemical machining (PECM). *Journal of Applied Electrochemistry* (2007) 37, pp.315-324, 2007.
- [129] R. Tsuboi, M. Yamamoto: Modeling and application of electrochemical machining process. *Proceedings of the ASME 2009 International Mechanical Engineering Congress & Exposition IMECE 2009*, IMECE2009-12552, pp.377-384, Florida, 2009.

- [130] T. Fujisawa, L. Inaba, M. Yamamoto, D. Kato: Multiphysics Simulation of Electrochemical Machining Process for Three-Dimensional Compressor Blade. *Journal of Fluids Engineering*, DOI: 10.1115/1.2956596, Volume 130 - Issue 8, 2008.
- [131] F. Klocke, M. Zeis, S. Harst, A. Klink, D. Veselovac, M. Baumgärtner: Modeling and Simulation of the Electrochemical Machining (ECM) Material Removal Process for the Manufacture of Aero Engine Components. *Procedia CIRP 8 (2013)*, pp.265-270, 2013.
- [132] J. McClennan, G. Alder, A. Sherlock, F. Mill, D. Clifton: Two-dimensional tool design for two-dimensional equilibrium electrochemical machining die-sinking using a numerical method. *Proceedings of the Institution of Mechanical Engineers, Part B: Journal of Engineering Manufacture*, vol. 220 no. 5, pp.637-645, 2006.
- [133] D. Curry, A. Sherlock, A. Mount, R. Muir: Time-dependent simulation of electrochemical machining under non-ideal conditions. *WIT Transactions on Engineering Sciences, Vol 48*, pp.133-142, 2005.
- [134] V. P. Zhitnikov, G. I. Fedorova, O. V. Zinatullina, A. V. Kamashev: Simulation of non-stationary processes of electrochemical machining. *Journal of Materials Processing Technology 149 (2004)*, pp.398-403, 2004.
- [135] A. R. Mount, D. Clifton, P. Howarth, A. Sherlock: An integrated strategy for materials characterisation and process simulation in electrochemical machining. *Journal of Materials Processing Technology 138 (2003)*, pp.449-454, 2003.
- [136] C. S. Chang, L. W. Hourng, C. T. Chung: Tool design in electrochemical machining considering the effect of thermal-fluid properties. *Journal of applied electrochemistry*, Vol. 29 (1999), pp.321-330, 1999.
- [137] S. S. Patil, V. Yadava: Finite element prediction of tool shapes in electrochemical machining. *International Journal Design Engineering*, Vol. 1, No. 1, pp.21-40, 2007.
- [138] J. A. Westley, J. Atkinson, A. Duffield: Generic aspects of tool design for electrochemical machining. *Journal of Materials Processing Technology 149 (2004)*, pp.384-392, 2004.
- [139] J. A. McGeough: Some effects of carbon content on the efficiency of electrochemically machined carbon steels and cast iron. *International Journal of Production Research*, Vol. 9, No. 2, 311-316, 1971.
- [140] O. Weber, H. Natter, A. Rebschläger, D. Bähre: Surface quality and process behaviour during Precise Electrochemical Machining of cast iron. *International*


- Symposium on Electrochemical Machining INSECT2011*, Editors: B. Mollay, M.M. Lohrengel, pp.41-46, Vienna, 2011.
- [141] O. Weber, H. Natter, A. Rebschläger, D. Bähre: Analytical characterization of the dissolution behavior of cast iron by electrochemical methods. *International Symposium on Electrochemical Machining Technology INSECT2012*, Editor: Maria Zybura-Skrabalak, pp.41-55, Krakow, 2012.
- [142] O. Weber, D. Bähre, A. Rebschläger: Study of Pulse Electrochemical Machining characteristics of spheroidal cast iron using sodium nitrate electrolyte. *International Conference on Competitive Manufacturing, COMA 13*, pp.125-130, South Africa, 2013.
- [143] O. Weber, A. Rebschläger, P. Steuer, D. Bähre: Modeling of the Material/Electrolyte Interface and the Electrical Current Generated during the Pulse Electrochemical Machining of Grey Cast Iron. *Proceedings of the 2013 European COMSOL Conference in Rotterdam*, Rotterdam, 2013.
- [144] D. Bähre, O. Weber, A. Rebschläger: Investigation on Pulse Electrochemical Machining Characteristics of Lamellar Cast Iron using a Response Surface Methodology-based Approach. *Procedia CIRP 6 (2013)*, pp.363-368, 2013.
- [145] K. P. Rajurkar, C. L. Schnacker, R. P. Lindsay: Some Aspects of ECM Performance and Control. *Annals of CIRP*, 37/1, pp.183-186, 1988.
- [146] T. Wagner (geb. Haisch): High rate electrochemical dissolution of iron-based alloys in NaCl and NaNO<sub>3</sub> electrolytes. Dissertation, Universität Stuttgart, Stuttgart, 2002.
- [147] M. Swat, A. Rebschläger, D. Bähre: Investigation of the energy consumption for the pulse electrochemical machining (PECM) process. *International Symposium on Electrochemical Machining Technology INSECT2013*, Editors: A. Schubert, M. Hackert-Oschätzchen, pp.65-71, Chemnitz, 2013.
- [148] M. Swat, A. Rebschläger, K. Trapp, T. Stock, G. Seliger, D. Bähre: Investigating the energy consumption of the PECM process for consideration in the selection of manufacturing process chains. *Procedia CIRP. 22nd CIRP conference on Life Cycle Engineering (LCE)*, 2015.
- [149] M. Spittel, T. Spittel: Steel symbol/number: X90CrMoV18/1.4112. *SpringerMaterials - The Landolt-Börnstein Database* (<http://www.springermaterials.com>), Springer-Verlag Berlin Heidelberg, DOI: 10.1007/978-3-540-44760-3\_91, 2009.
- [150] M. Spittel, T. Spittel: Steel symbol/number: X6CrNiMoTi17-12-2/1.4571. *SpringerMaterials - The Landolt-Börnstein Database*

- (<http://www.springermaterials.com>), Springer-Verlag Berlin Heidelberg, DOI: 10.1007/978-3-540-44760-3\_115, 2009.
- [151] M. Spittel, T. Spittel: Steel symbol/number: X2CrNiMo17–12–2/1.4404. *SpringerMaterials - The Landolt-Börnstein Database* (<http://www.springermaterials.com>), Springer-Verlag Berlin Heidelberg, DOI: 10.1007/978-3-540-44760-3\_100, 2009.
- [152] M. Spittel, T. Spittel: Steel symbol/number: 100Cr6/1.3505. *SpringerMaterials - The Landolt-Börnstein Database* (<http://www.springermaterials.com>), Springer-Verlag Berlin Heidelberg, DOI: 10.1007/978-3-540-44760-3\_83, 2009.
- [153] N. Smets, S. Van Damme, D. De Wilde, G. Weyns, J. Deconinck: Time-averaged concentration calculations in pulse electrochemical machining, spectral approach. *Journal of Applied Electrochemistry* (2009) 39, pp.2481-2488, 2009.
- [154] N. Smets, S. Van Damme, D. De Wilde, G. Weyns, J. Deconinck: Time averaged concentration calculations in pulse electrochemical machining, spectral approach. *Journal of Applied Electrochemistry* (2009) 39, pp.791-798, 2009.
- [155] N. Smets, S. Van Damme, D. De Wilde, G. Weyns, J. Deconinck: Time averaged concentration calculations in pulse electrochemical machining. *Journal of Applied Electrochemistry* (2008) 38, pp.1577-1582, 2008.
- [156] N. Smets, S. Van Damme, D. De Wilde, G. Weyns, J. Deconinck: Time averaged calculations in pulse electrochemical machining, using a strongly non-linear model. *Journal of Applied Electrochemistry* (2010) 40, pp.1395-1405, 2010.
- [157] R. N. Muir, D. R. Curry, F. Mill, A. Sherlock, A. R. Mount: Real-time parameterization of electrochemical machining by ultrasound measurement of the interelectrode gap. *Proceedings of the Institution of Mechanical Engineers, Part B: Journal of Engineering Manufacture*, vol. 221, pp.551-558, 2007.
- [158] A. R. Mount, P. S. Howarth, D. Clifton: The use of a segmented tool for the analysis of electrochemical machining. *Journal of Applied Electrochemistry* 31, pp.1213-1220, 2001.
- [159] J. A. McGeough, M. C. Leu, K. P. Rajurkar, A. K. M. De Silva, Q. Liu: Electroforming Process and Application to Micro/Macro Manufacturing. *CIRP Annals*, Volume 50, Issue 2, pp.499–514, 2001.
- [160] A. Lesch, G. Wittstock, C. Burger, J. Hackenberg, B. Walther: Two-way anodic dissolution of low alloyed steel in chloride/nitrate mixed electrolytes.

- International Symposium on Electrochemical Machining INSECT2009*, Editors: A. Michaelis, M. Schneider, pp.89-94, 2009.
- [161] D. Landolt, S. Mischler, M. Stemp: Electrochemical methods in tribocorrosion: a critical appraisal. *Electrochimica Acta* 46 (2001), pp.3913-3929, 2001.
- [162] J. Kozak: Computer simulation system for electrochemical shaping. *Journal of Materials Processing Technology* 109 (2001), pp.354-359, 2001.
- [163] F. Klocke, M. Zeis, A. Klink, D. Veselovac: Technological and economical comparison of roughing strategies via milling, sinking-EDM, wire-EDM and ECM for titanium- and nickel-based blisks. *CIRP Journal of Manufacturing Science and Technology* 6 (2013), pp.198-203, 2013.
- [164] T. Haisch, E. J. Mittemeijer: Electrochemical Machining: The Role of Steel Microstructure in High-Rate Anodic Dissolution. *JOM*, Vol. 54, Issue 7, pp.38-41, 2002.
- [165] T. Haisch, E. Mittemeijer and J. W. Schultze: Electrochemical machining of the steel 100Cr6 in aqueous NaCl and NaNO<sub>3</sub> solutions: microstructure of surface films formed by carbides. *Electrochimica Acta* 47 (2001), pp. 235–241, 2001.
- [166] L. Dabrowski, T. Paczkowski: Computer Simulation of Two-dimensional Electrolyte Flow in Electrochemical Machining. *Russian Journal of Electrochemistry*, Vol. 41, No. 1, pp.91-98, 2005.
- [167] D. Clifton, A. R. Mount, G. M. Alder, D. Jardine: Ultrasonic measurements of the inter-electrode gap in electrochemical machining. *International Journal of Maching Tools & Manufacture*, 42, pp.1259-1267, 2002.
- [168] D. Clifton, A. R. Mount, F. Mill, P. Howarth: Characterization and representation of non-ideal effects in electrochemical machining. *Proceedings of the Institution of Mechanical Engineers, Part B: Journal of Engineering Manufacture*, vol. 217, pp.373-385, 2003.
- [169] M. Zybura, G. Skrabalak: Electrochemical Smoothing - Investigations of Surface Layer Properties depending on Various Electrochemical Machining Ways. *International Symposium on Electrochemical Machining Technology INSECT2010*, Editors: J. Deconinck, D. De Wilde, pp.9-15, Brussels, 2010.
- [170] K. Weißhaar, M. Weinmann, A. Jung, O. Weber, H. Natter: Replication of microstructured tools for electrochemical machining applications. *The International Journal of Advanced Manufacturing Technology*, Springer London, 2015.

## APPENDIX A Olympus iSpeed-TR

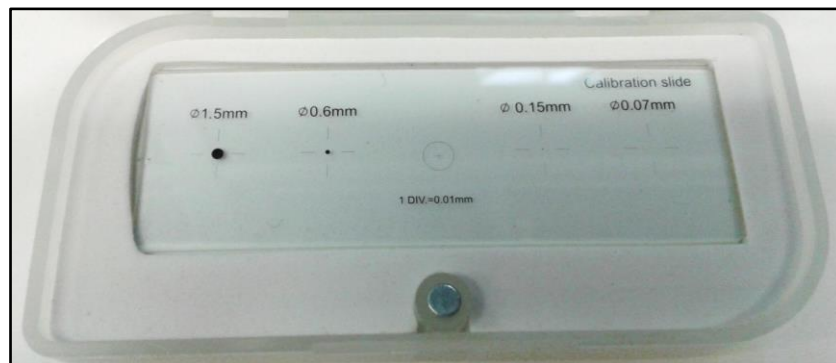
### Technical data and specifications Olympus iSpeed-TR

	Technical data	
	Maximum resolution [pixel]	1,280 x 1,024
	Framerate at max. resolution [fps]	2,000
	Framerate [fps]	1-10,000
	Minimum exposure time [μs]	2.16
	Sensor	CMOS
Framerate [fps]	Max. resolution [pixel]	Recording time [s]
1	1,280 x 1,024	2,447.000
10	1,280 x 1,024	244.700
100	1,280 x 1,024	24.470
2,000	1,280 x 1,024	1.224
3,000	1,068 x 800	1.256
4,000	912 x 684	1.298
5,000	804 x 600	1.334
7,500	636 x 476	1.417
10,000	528 x 396	1.539

## APPENDIX B Microscope calibration slide

**Model:** A36CALM2 (<http://www.microscopenet.com>, online 27.4.2015)  
**Slide material:** Schott optical glass  
**X-Y metric ruler:** 0.01mm per division, total length of scale 1mm, 100 divisions  
**4 calibration dots:** diameters of 1.5mm, 0.6mm, 0.15mm, 0.07mm  
**Slide size:** 75mm x 25mm x 0.9mm

Size of the reference structure mm	Optical evaluation results			
	pixel		mm/pixel	µm/pixel
1.5	179	→	0.00838	8.38
0.6	73	→	0.00822	8.22
0.15	17	→	0.00882	8.82
0.07	8	→	0.00875	8.75
0.1	12	→	0.00833	8.33
			<b>Average</b>	<b>8.50</b>



	CDU Picture	Software Analysis	
∅ 0.6mm			
∅ 0.07mm			
Cross			